Experimental study of the electric dipole moment of neutrons by crystal diffraction

（結晶回折法による中性子電気双極子能率の実験的研究）

Shigeyasu Ito

Graduate School of Science,
Nagoya University

March, 2024

Abstract

The Standard Model of Elementary Particles is almost complete with great success, awaiting for the discovery of the Higgs boson in 2012. However, there are still some unsolved problems. One of them is that we have not been able to explain the current matter-dominated universe. For the matter-dominated universe to exist, Sakharov's three conditions are necessary, one of which is CP symmetry violation.

The amount of CP symmetry violation that can be explained by the Standard Model is nine orders of magnitude less than the amount based on cosmological observations. This suggests the existence of undiscovered CP symmetry violation. If a fundamental particle such as a neutron has an electric dipole moment (nEDM), it violates the time-reversal symmetry and according to the CPT theorem, CP symmetry. Despite 70 years of experiments searching for the nEDM, it has not yet been discovered, and the current upper limit is $1.8 \times 10^{-26}\ e \cdot \mathrm{cm}$ obtained by using ultra-cold neutrons (UCN). The value predicted by the Standard Model is very small at $\sim 10^{-32}\ e \cdot \mathrm{cm}$, and some theories beyond the Standard Model predict values on the order of 10^{-26} to $10^{-28}\ e \cdot \mathrm{cm}$. Increasing the sensitivity by another two orders of magnitude could limit these theories. To this end, it is essential not only to increase the statistical sensitivity, but also to develop other methods with different systematic uncertainties and to make efforts to reduce them.

We are experimentally studying the search for nEDM by crystal diffraction, which has different systematic uncertainties from those of the UCN method. Crystal diffraction is characterized by the dynamical diffraction of neutrons in crystals and the use of the very strong electric field sensed by neutrons in the diffraction process. The experiments were performed using the pulsed neutron source at MLF in J-PARC. First, to verify the dynamical diffraction using pulsed neutrons, Pendellösung fringes were observed, diffraction intensity distributions on the crystal ejection surface were measured, and diffraction intensities were evaluated. The results of these experiments using pulsed neutrons confirmed the results of previous reactor neutron studies.

Next, the experiment to measure the intra-crystal electric field using α-quartz was performed. For the (110)-plane, where the intra-crystal electric field is expected to exist, we obtained results that are consistent with the conventional measurements. In addition, other crystal planes were also investigated, and non-zero electric fields were observed at crystal planes where the intra-crystal electric field was assumed to be zero. This is thought to be due to the interference term, which had been considered negligible due to the Pendellösung oscillations in space. If there are macroscopic defects in the crystal that disturb the Pendellösung interference, these interference terms do not completely cancel each other out and the effect of that can be appear as an electric field. Such defects in a crystal introduce systematic uncertainties in the nEDM search experiment and must be minimized. The appearance of such an electric field at a crystal plane, which should be zero, can be used as a new indicator for this crystal imperfection. Since the experimental results are still limited, further experimental and theoretical studies are needed to clarify the contribution of the interference term. This will allow us to monitor the spin rotation using simultaneous polychromatic diffraction from multiple crystal planes with a pulsed neutron source to investigate systematic uncertainties of the experiment.

Regarding the intra-crystal electric field, which is one of the factors determining the sensitivity of nEDM search experiments, we were able to confirm that a strong electric field was available as expected. The remaining two factors, interaction time and statistics, are discussed, and an external magnetic field application method and a multi-stage system are proposed, respectively. By combining these two methods, the possibility of reaching $1.0 \times 10^{-26}\ e \cdot \mathrm{cm}$ in 200 days at the highest output power of the J-PARC MLF was demonstrated.

Contents

1 Introduction **6**
- 1.1 CP-Violation . . . 6
- 1.2 Electric Dipole Moment of a Neutron . . . 7
- 1.3 Overview and Organization of This Thesis . . . 10

2 nEDM Search Experiment **11**
- 2.1 Principle of nEDM Search Experiment . . . 11
- 2.2 The UCN Method . . . 12
- 2.3 Free Flight Method . . . 14
- 2.4 Crystal Diffraction Method . . . 15
- 2.5 Comparison of Three Methods . . . 16

3 Dynamical Diffraction Theory **18**
- 3.1 The Interaction Potential of a Neutron in a Non-Magnetic Crystal . . . 18
- 3.2 Crystal Structure Factor . . . 19
- 3.3 One Wave Approximation . . . 21
- 3.4 Two Wave Approximation . . . 23
- 3.5 Wave Field Inside a Plane Slab in the Laue Configuration . . . 26
- 3.6 Intensity Distribution of a Plane Slab . . . 29

4 Principles of nEDM Measurement by the Crystal Diffraction Method **34**
- 4.1 Principles of nEDM Measurement by the Crystal Diffraction Method . . . 34
- 4.2 Calculation of the nEDM Effect . . . 36
- 4.3 False Signal of EDM Effect . . . 39
- 4.4 Candidates of Non-Centrosymmetric Crystal . . . 40

5 Overview of the Dynamical Diffraction from Experimental View Points **42**
- 5.1 Pendellösung Fringes . . . 42
- 5.2 Intensity Distribution on the Exit Surface . . . 46
  - 5.2.1 Measurement of the Intensity Distribution on the Exit Surface . . . 46
  - 5.2.2 Measurement Results of the Intensity Distribution . . . 46
- 5.3 Calculation of the Intensity of Diffraction . . . 48

6 Theory of the Intra-Crystal Electric Field **51**

7 The Measurement of Intra-Crystal Electric Field by Spin Rotation **54**
- 7.1 Theory of the Measurement . . . 54
- 7.2 Setup of the Experiment . . . 55
- 7.3 The Preliminary Experiment . . . 57
- 7.4 Results of (110)-Plane with $\Delta\phi_g \neq 0$ in the Symmetric Laue Configuration . . . 59
  - 7.4.1 Evaluation of the Diffraction Intensity . . . 59
  - 7.4.2 Initial Polarization . . . 62
  - 7.4.3 Spin Rotation . . . 62
  - 7.4.4 Compensation for External Magnetic Field . . . 63
  - 7.4.5 Summary of the Statistical and Systematic Uncertainties . . . 64

7.5 Results of Other Crystal Planes with $\Delta\phi_g = 0$ in the Asymmetric Laue Configuration 65
7.6 Discussion of the Intra-crystal Electric Field 68

8 Improvement of the Crystal Diffraction Method **71**
8.1 The Possibility of Extending the Statistics by Multi-unit 72
8.2 The Possibility of Increasing of Interaction Time by Applying an External Magnetic Field inside a Crystal only 72

9 Feasible Study of nEDM Search Experiment by the Crystal Diffraction Method **76**
9.1 Feasible Study of nEDM Search Experiment Using α-quartz 76
9.2 Feasible Study of nEDM Search Experiment Using $Bi_{12}GeO_{20}$ 77

10 Conclusion **78**

List of Figures

1.1 Generation of matter-dominated universe . . . 7
1.2 The permanent EDM and T-violation and CP-violation . . . 8
1.3 The evolution of the upper limit value of the nEDM . . . 9
1.4 Schematic diagram of CP-violation sources and the observable EDMs . . . 9
2.1 Principle of the experiment to search for EDM . . . 11
2.2 Scheme of the UCN method . . . 13
2.3 Scheme of the free flight method . . . 14
2.4 Scheme of the crystal diffraction method . . . 15
3.1 The nucleus position in a unit cell . . . 19
3.2 The crystal structure and atom coordinates of α-quartz . . . 21
3.3 Schematic diagram of one wave approximation. . . . 23
3.4 Schematic diagram of Laue and Bragg configurations. . . . 24
3.5 Schematic diagram of two wave approximation . . . 25
3.6 Rocking curve. . . . 28
3.7 The spatial intensity distribution of the crystal injection surface. . . . 29
3.8 Neutron current and the definition of Γ . . . 30
3.9 Schematic diagrams of neutron currents in the 3 cases. . . . 31
3.10 Diffraction intensity distribution calculated . . . 33
3.11 Diffraction intensity distribution calculated with slit width and divergence angle . . . 33
4.1 α-and β-waves in a crystal. . . . 35
4.2 Precession of nMDM and nEDM. . . . 37
4.3 Rotation vector and Spin rotation. . . . 37
4.4 Tilt of spin analysis axis and false signal of EDM effect. . . . 39
4.5 Tilt of spin analysis axis and false signal of EDM effect. . . . 40
5.1 The schematic diagram of the experiment to observe the Pendellösung fringes. . . . 42
5.2 Pendellösung fringes of $(1\bar{1}1)$-plane of Si crystal. . . . 43
5.3 Evaluation of crystallinity by X-ray and the region used in the experiment. . . . 44
5.4 Pendellösung fringes of (110)-plane of α-quartz. . . . 45
5.5 Setup of the experiment measuring the intensity distribution. . . . 46
5.6 The results of experiment and the plane-wave theory. . . . 47
5.7 The results of Pendellösung fringes experiment in April 2019. . . . 48
5.8 Schematic diagram of the calculation of the intensity of diffracted neutrons. . . . 49
7.1 Setup of the experiment of the spin rotation. . . . 55
7.2 Evaluation of crystallinity by X-ray for the experiment of the spin rotation. . . . 56
7.3 TOF spectra of neutron polarization passed through the solenoid coil. . . . 57
7.4 The magnetic field of solenoid coil obtained from the spin rotation. . . . 58
7.5 TOF spectrum at each tilt angle. . . . 60
7.6 TOF spectrum of the tilt angle of 0 degrees for each measurement. . . . 61
7.7 TOF spectrum at tilt angle of 37.5 degrees for evaluation of the background. . . . 61
7.8 Initial polarization by the tilt angle and the measurement mode. . . . 62
7.9 The relationship of $P_{\rm obs}/P_0$ and the tilt angle γ. . . . 63
7.10 TOF spectra of diffraction peak of $(0\bar{2}1)$-, (011)- and $(11\bar{1})$-planes. . . . 66
7.11 Spin rotation of four waves, α, β, λ, and η waves. . . . 69
7.12 The effect of the effective intra-crystal electric field due to λ- and η-waves. . . . 70
8.1 Basic unit for the experiment to search for nEDM by crystal diffraction. . . . 71
8.2 Shematic diagram of Multi-stage system. . . . 72
8.3 The external magnetic field application method. . . . 73

8.4 Time evolution of the nEDM signal and the precession of the α- and β-waves in the case of $n = 1$ ($\kappa = 1/3$). 75
8.5 Time evolution of the nEDM signal and the precession of the α- and β-waves in the case of $n = 6$ ($\kappa = 11/13$). 75

List of Tables

1.1 The magnetic moment anomaly of electrons a_e. 6
2.1 Comparison of required parameters of measurement sensitivity for three different measurement methods. 16
4.1 Candidates of non-symmetric crystal for the diffraction method. 41
6.1 Summary of 16 components. 53
7.1 Industry Standard for an artificial α-quartz 56
7.2 Summary of the statistical and systematic uncertainties of the spin rotation of (110)-plane. . 64
7.3 Summary of results for other planes with asymmetric Laue configuration. 65
9.1 Feasibility study for α-quartz. 76
9.2 Feasibility study for $Bi_{12}GeO_{20}$. 77

1 Introduction

1.1 CP-Violation

The Standard Model (SM) of elementary particles reached a point of completion with the discovery of the Higgs boson in 2012 [1, 2]. It is the most successful theory in terms of being able to explaining and predicting much of elementary particle physics. Symbolic is the magnetic moment anomaly of electrons a_e. Its experimental value [3] and its theoretically calculated value [4, 5] are given by Table 1.1. The discrepancy is less than 10 orders of magnitude.

Table 1.1: The magnetic moment anomaly of electrons a_e, experimental value and theoretical value.
Two results of theoretical calculations are exemplified. Both use $\alpha^{-1}(\mathrm{Cs})$ [6] as the fine-structure constant. Latest result is $\alpha^{-1}(\mathrm{Rb}) = 137.035999206(11)$ using Rb atoms [7], but this result is 5σ off from that. This circumstance has not yet been taken into account.

	The value of a_e	The fine-structure constant used in the calculation
Experiment [3]	0.00115965218059(13)	—
Theoretical Calculation [4]	0.00115965218160 6(252)	$\alpha^{-1}(\mathrm{Cs}) = 137.035999046(27)$ [6]
Theoretical Calculation [5]	0.00115965218154 7(247)	$\alpha^{-1}(\mathrm{Cs}) = 137.035999046(27)$ [6]

A theoretical pillar that runs through the Standard Model is symmetry. It states that the laws of physics are invariant through the symmetry operations, which include spatial reversal symmetry (P), charge reversal symmetry (particle-antiparticle symmetry) (C), and time reversal symmetry (T). The principle that all physical interactions are symmetric led to the development of the SM as the guiding principle for its construction, but symmetry breaking was discovered as another aspect of the evolution of the SM. The first symmetry breaking was discovered in an experiment by Wu in 1957 [8]. The angular distribution of electrons emitted from ^{60}Co in the weak interaction was shown to violate the space inversion symmetry (P-violation) proposed by Lee and Yang in 1956 [9]. This was followed by the discovery of charge symmetry breaking (C-violation) in the weak interactions by Garwin [10] and Friedman [11] in the same year 1957. The first discovery of symmetry breaking with simultaneous charge and space inversion (CP-violation) was made by Christenson et al. in 1964 [12], using K mesons. CP-violation was further confirmed by KEK [13] and SLAC [14] with the decay of B mesons. The source of the symmetry breaking in the SM is the complex phase in the weakly interacting CKM matrix and the θ term in quantum Chromodynamics. This fully explains the symmetry breaking discovered so far in the SM.

However, there is a serious problem here. This is the problem that the SM does not adequately explain the current matter-dominated universe, but rather the discrepancy is as large as nine orders of magnitude. Current cosmology holds that the universe began with light in the Big Bang. From the light, equal number of matter and antimatter particles are created through pair production. Eventually, as the universe expands and the temperature decreases, matter and antimatter particles annihilate each other and become light, and then the material universe cannot exist. The conditions for the existence of the material universe, as it exists today, are the Sakharov conditions proposed by Sakharov in 1967 [15].

1. Baryon number violation.
2. C- and CP-violation.
3. Processes outside of thermal equilibrium.

While condition 3 is satisfied, condition 1 has not yet been discovered. As mentioned, the existence of CP-violation has been discovered, and its expression mechanism is included in the SM, which fully explains the CP symmetry breaking phenomena discovered so far. However, the amount that can be predicted with the SM is not at all sufficient. Figure 1.1 shows this schematically.

If the number of baryons is n_{B} and the number of antibaryons is $n_{\bar{\mathrm{B}}}$, then the amount of light filling the universe today is $n_\gamma = 2 \times n_{\bar{\mathrm{B}}}$, and the number of baryons remaining as matter is $B = n_{\mathrm{B}} - n_{\bar{\mathrm{B}}}$. This ratio can be measured from observations of the cosmic background radiation and is given by

$$B/n_\gamma \approx 10^{-9}. \tag{1.1}$$

In contrast, the quantity that can be predicted in the SM framework [16] is

$$B/n_\gamma \approx 10^{-18}, \tag{1.2}$$

which is 9 orders of magnitude smaller than the value predicted by the SM framework. This means that the sources of the yet unknown CP-violation exist outside the SM framework, and the discovery of a new CP-violation opens the door to new physics beyond the SM (Beyond Standard Model: BSM).

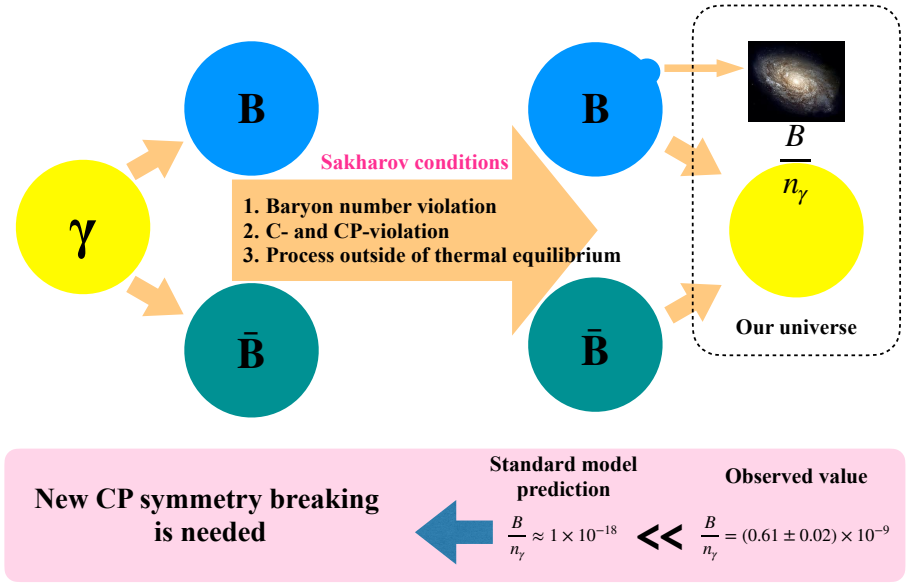

Figure 1.1: Generation of matter-dominated universe:
The universe began with light in the Big Bang, which initially produced an equal number of baryons. Later, under Sakharov conditions, an asymmetry in the number of baryons is thought to have occurred, producing the current matter-dominated universe. However, the amount of asymmetry predicted by the SM is much less than what cosmological observations indicate.

1.2 Electric Dipole Moment of a Neutron

The fact that a fundamental particle such as a neutron has an electric dipole moment (EDM) breaks the time-reversal symmetry. As shown in Fig. 1.2, time reversal causes the spin to flip direction, but the electric dipole moment, the spatial distribution of the charge, does not change direction.

The interaction potential of a particle placed in an electromagnetic field is

$$U = -\mu_n \boldsymbol{B} \cdot \frac{\boldsymbol{S}}{S} - d_n \boldsymbol{E} \cdot \frac{\boldsymbol{S}}{S} \tag{1.3}$$

where μ_n is the magnetic dipole moment of neutrons (nMDM), d_n is the electric dipole moment of neutrons (nEDM), $\boldsymbol{B}$ and $\boldsymbol{E}$ are the magnetic and electric fields, respectively, and $\boldsymbol{S}/S$ is the spin orientation. Time reversal yields

$$\boldsymbol{B} \to -\boldsymbol{B}, \quad \boldsymbol{E} \to \boldsymbol{E}, \quad \boldsymbol{S} \to -\boldsymbol{S} \tag{1.4}$$

Figure 1.2: The permanent EDM and T-violation and CP-violation.
Time reversal changes the orientation of the spin, but the spatial distribution, the EDM, does not change orientation, so the exist of the permanent EDM violates the time reversal symmetry. According to the CPT theorem, this is equivalent to violation of the CP symmetry.

and thus the potential after time reversal is

$$U = -\mu_n \boldsymbol{B} \cdot \frac{\boldsymbol{S}}{S} + d_n \boldsymbol{E} \cdot \frac{\boldsymbol{S}}{S} \tag{1.5}$$

and if d_n is not zero, the time reversal symmetry is broken. Time-reversal symmetry is equivalent to CP symmetry according to the CPT theorem [17]. Thus, the search for time-reversal symmetry-breaking physics is of great benefit because it allows us to search for CP-violation physics without using antiparticles. Therefore, several studies have been conducted in addition to the EDM search experiments. For example, the study of T-violation using a neutron-induced compound nucleus is being vigorously pursued.

Purcell and Ramsey [18] were the first to point out the importance of the EDM search before symmetry breaking had yet been discovered. They stated that whether a fundamental particle has an EDM or not must be verified experimentally rather than by a symmetry-based hypothesis, and using the experimental results of Havens et al. [19] on neutron-electron interactions, they gave an first upper limit for the neutron electric dipole moment (nEDM) of 3×10^{-18} $e \cdot$cm. Subsequently, CP-violation was discovered as described in section 1.1.

Figure 1.3 shows the evolution of the upper limits obtained by the nEDM search experiments to date. The most stringent upper limit is 1.8×10^{-26} $e \cdot$cm obtained by Abel et al [20, 21], using the ultra-cold neutron (UCN) method. In contrast, the value of the nEDM predicted by the SM is very small, $\sim 10^{-32}$ $e \cdot$cm. On the other hand, some theories beyond the SM allow much larger values of nEDM. One such theory, the supersymmetry theory, predicts nEDM values of $\sim 10^{-26}$ to $\sim 10^{-28}$ $e \cdot$cm. If the sensitivity improves by another two orders of magnitude, it will provide a constraint for some new physical theories. If not, the predictions of the SM are another six orders of magnitude smaller, so it is being studied as one of the most sensitive probes with very low background in the search for new physics.

Figure 1.4 shows how the source of CP-violation manifests itself as a concrete observable at realistic energy levels [22]. Thus, by conducting not only nEDM but also multifaceted EDM searches, such as search for electron EDM by paramagnetic atoms and diamagnetic atoms, search for muon EDM and etc., the whole process of EDM manifestation from the source of CP-violation. These experiments are complementary to each other.

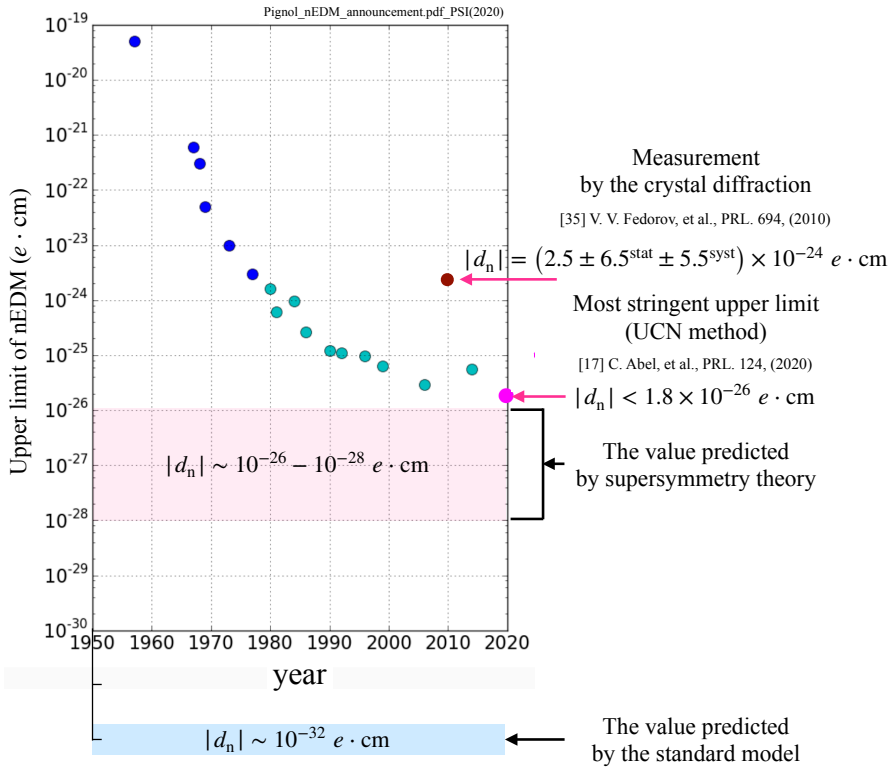

Figure 1.3: The evolution of the upper limit value of the nEDM.
Over the past 70 years, the upper limit value of the nEDM has improved by about seven orders of magnitude, but it has not yet been discovered. For the value of the nEDM predicted by the SM, indicated by the blue band, there is still an unknown region extending over six orders of magnitude. The red band indicates the region predicted by supersymmetry theory. Blue circles and green circles indicate the upper limit value by the free flight method and UCN method, respectively.(see section 2) The most stringent upper limit value (by UCN method) and the upper limit value by the crystal diffraction method is indicating by a red circle and a brown circle, respectively.

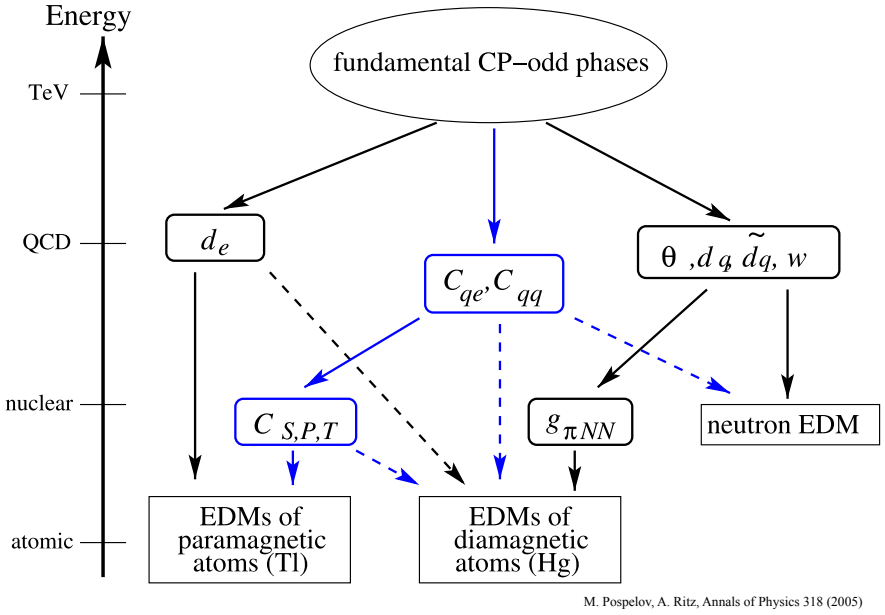

Figure 1.4: Schematic diagram of the relationship between CP-violation sources and the observable EDMs.
Solid lines represent the main dependencies and dashed lines represent the weaker dependencies. Adapted from reference [22]

1.3 Overview and Organization of This Thesis

We continue to develop the technique of the diffraction method and studying the dynamical diffraction phenomena in order to realize the nEDM search experiment using the crystal diffraction method. It is important because it has different systematic uncertainties from other methods. In this paper, the fundamentals of nEDM search experiments using the crystal diffraction method are described and experimentally demonstrations are reported, and in particular, the electric field interacting with neutrons in a crystal. The possibility of exceeding the current upper limits is then discussed.

The nEDM search experiments use the interaction of the spin magnetic moment and the electric dipole moment with the electromagnetic field, which can be classified into three types of methods. In Chapter 2, the outline of each method is described, citing representative experiments, and the characteristics of each method are described.

In the nEDM search experiment by crystal diffraction method, the electromagnetic interaction between a crystal and neutrons is used. The dynamical diffraction theory is essential to describe the behavior of neutrons in the crystal. The behavior of neutrons in crystals is described in Chapter 3, based on the plane wave dynamical diffraction theory.

Chapter 4 describes the theory of nEDM search experiments using crystal diffraction methods, using the dynamical diffraction theory. The results of the experimental verification of the dynamical diffraction, the demonstration of the pendllösung fringes, the demonstration of the intensity distribution of the reflected dynamical diffraction and the quantitative evaluation of the diffraction intensity are reported in Chapter 5.

In the nEDM search experiments using the crystal diffraction method, the electric field interacting with neutrons dynamically diffracted in a crystal is important. Chapter 6 provides a theoretical discussion of the electric field in a crystal and also discusses interference terms that were previously thought to be negligible.

In Chapter 7, the demonstration of the spin rotation due to the relativistic magnetic field and the results of the electric field in the crystal are reported. With respect to the electric field in the crystal, while a consistent result was obtained for the specific crystal plane that have been measured so far, non-zero electric fields were observed for some crystal planes that have not been measured but were theoretically assumed to have no electric field in the crystal. This suggests that the interference term mentioned in Chapter 6 may not be negligible.

The sensitivity of nEDM search experiments using crystal diffraction is three orders of magnitude lower than that of the UCN method, due to insufficient interaction time and neutron number, in contrast to the advantage of a strong electric field. In Chapter 8, two improvements are proposed to address these issues, a method to extend the interaction time by applying an external magnetic field only inside the crystal, and a multi-stage system to increase the statistics, are proposed.

Finally, in Chapter 9, we discuss plans and possibilities for nEDM search experiments using the crystal diffraction method.

2 nEDM Search Experiment

In this chapter, we describe the basic principles of nEDM measurements and outline three typical experimental methods

2.1 Principle of nEDM Search Experiment

As shown in Fig. 2.1(a), when a neutron with spin perpendicular to the magnetic field $\boldsymbol{B}$ and the electric field $\boldsymbol{E}$ parallel to $\boldsymbol{B}$ is placed, the neutron performs a precession in the potential field in Eq. (1.3) with Larmor frequency of

$$\omega_{\mathrm{L}}^{+} = \frac{2\mu_n B}{\hbar} + \frac{2d_n E}{\hbar}. \tag{2.1}$$

Next, when the electric field is antiparallel to the magnetic field by reversing the direction of the electric field shown in Fig. 2.1(b), then the potential and the larmor frequency become as follows;

$$U = -\mu_n \boldsymbol{B} \cdot \frac{\boldsymbol{S}}{S} + d_n \boldsymbol{E} \cdot \frac{\boldsymbol{S}}{S}, \tag{2.2}$$

$$\omega_{\mathrm{L}}^{-} = \frac{2\mu_n B}{\hbar} - \frac{2d_n E}{\hbar}. \tag{2.3}$$

From the difference of these two Larmor frequencies, nEDM can be obtained as follows;

$$\omega_{\mathrm{L}}^{+} - \omega_{\mathrm{L}}^{-} = \frac{4d_n E}{\hbar}. \tag{2.4}$$

On the other hand, it is also possible to directly measure the spin rotation due to the electric field. In this case, the amount of spin rotation is given by Eq. (2.5), and the corresponding change in polarization is measured.

$$\varphi_{\mathrm{EDM}} = \frac{2d_n E\tau}{\hbar} \tag{2.5}$$

where τ is an interaction time between nEDM and the electric field.

There are three main types of nEDM search experiments: the UCN method and the flight method utilize the former measurement principle, while the crystal diffraction method uses the latter.

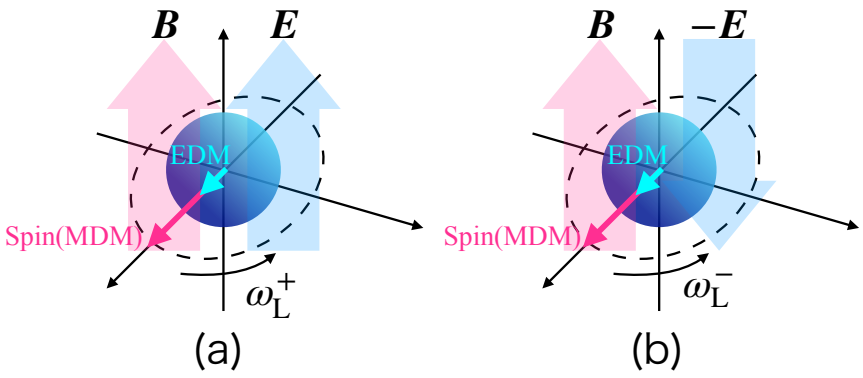

Figure 2.1: Principle of the experiment to search for EDM.
A neutron with spin perpendicular to the magnetic field $\boldsymbol{B}$ and the electric field $\boldsymbol{E}$. (a) The electric field is parallel to the magnetic field. (b) The electric field is antiparallel to the magnetic field. The nEDM can be obtained from the difference of two Larmor frequencies.

2.2 The UCN Method

The UCN method is a method in which spin-polarized ultra-cold neutrons (UCN) are confined in a vessel for a period of time and an electromagnetic field is applied to measure the Larmor frequency difference Eq. (2.4). UCN is a neutron with energy of about 250 neV or less, its velocity is less than about 7 m/s, and its wavelength is greater than about 6000 nm. Because of this very long wavelength compared to the lattice spacing, the nuclear potential of the material is not directly applied to UCNs, but the spatially averaged effective Fermi potential (optical potential) is applied to UCN. Therefore, it is fully reflected at the surface of materials such as nickel (250 neV) and stainless steel (220 neV), which have high optical potentials. Using this advantage of UCN, the UCN method is performed by confining UCN in a vessel such as nickel. As a typical example, the UCN method experiment conducted at I.L.L. (Institute of Laue and Langevin) in Grenoble, France from 1996 to 2002 is briefly introduced here [23, 24, 25, 26].

Figure 2.2 is the scheme of their experimental setup taken from reference [25]. The vessel in which neutrons are stored is the rectangular part in the center. Surrounding it is a coil that creates a constant magnetic field (10 mG) inside the vessel, and outside the coil is a four-layer magnetic shield to block the external magnetic field. There are electrodes at the top and bottom of the storage vessel to create an electric field (about 10 kV/cm) inside the vessel, and a high voltage is supplied from the top. UCN generated in another device is introduced into the vessel from the bottom. It is then polarized into upward spin by passing through a thin magnetized iron film (about 1 μm). The Larmor frequency Eq. (2.1) and Eq. (2.3) were measured by the Ramsey separated-oscillatory-field magnetic resonance method [27]. After the UCN is introduced into the vessel, the spins are flipped $\pi/2$ in the direction perpendicular to the magnetic field by the oscillating magnetic field of the horizontal RF coil, which is not shown in the figure. This can be done by selecting the frequency and intensity of the oscillating magnetic field appropriately. The UCN then have a free precession (about 30 Hz) in a constant magnetic and electric field for 130 seconds. A second $\pi/2$ flip is then performed. At this time, the measurement is repeated, scanning the frequency of the oscillating magnetic field in the range before and after the frequency of the free precession motion, in a coherent state with the first $\pi/2$ flip. When the frequency coincides with the free precession, the spin goes down, and when the phase is shifted by π, the spin goes up. The UCN is ejected from the bottom of the vessel, and now the magnetized iron film acts as an analyzer, transmitting only the up-spin UCN, which is counted by the 3He detector. In addition, the π-flipper RF coil above the magnetized iron film inverts the spin of the UCNs, so that only spin-down UCNs can be counted. The resulting resonance oscillations can be obtained, as shown in the figure, and the frequency of the free precession can be measured from its maximum amplitude position.

By switching the polarity of the high voltage applied to the top of the vessel, the nEDM can be obtained from Eq. (2.4) by measuring the Larmor frequency in the case of an electric field parallel and antiparallel to a constant magnetic field. In this experiment, the time variation of the constant magnetic field is corrected by a cooperating magnetometer using mercury atoms. The nEDM result obtained was $3.0 \times 10^{-26}\ e \cdot \mathrm{cm}$. Subsequently, a similar experiment was performed by an experimental group at PSI and the current upper limit of nEDM was updated to $1.8 \times 10^{-26}\ e \cdot \mathrm{cm}$.

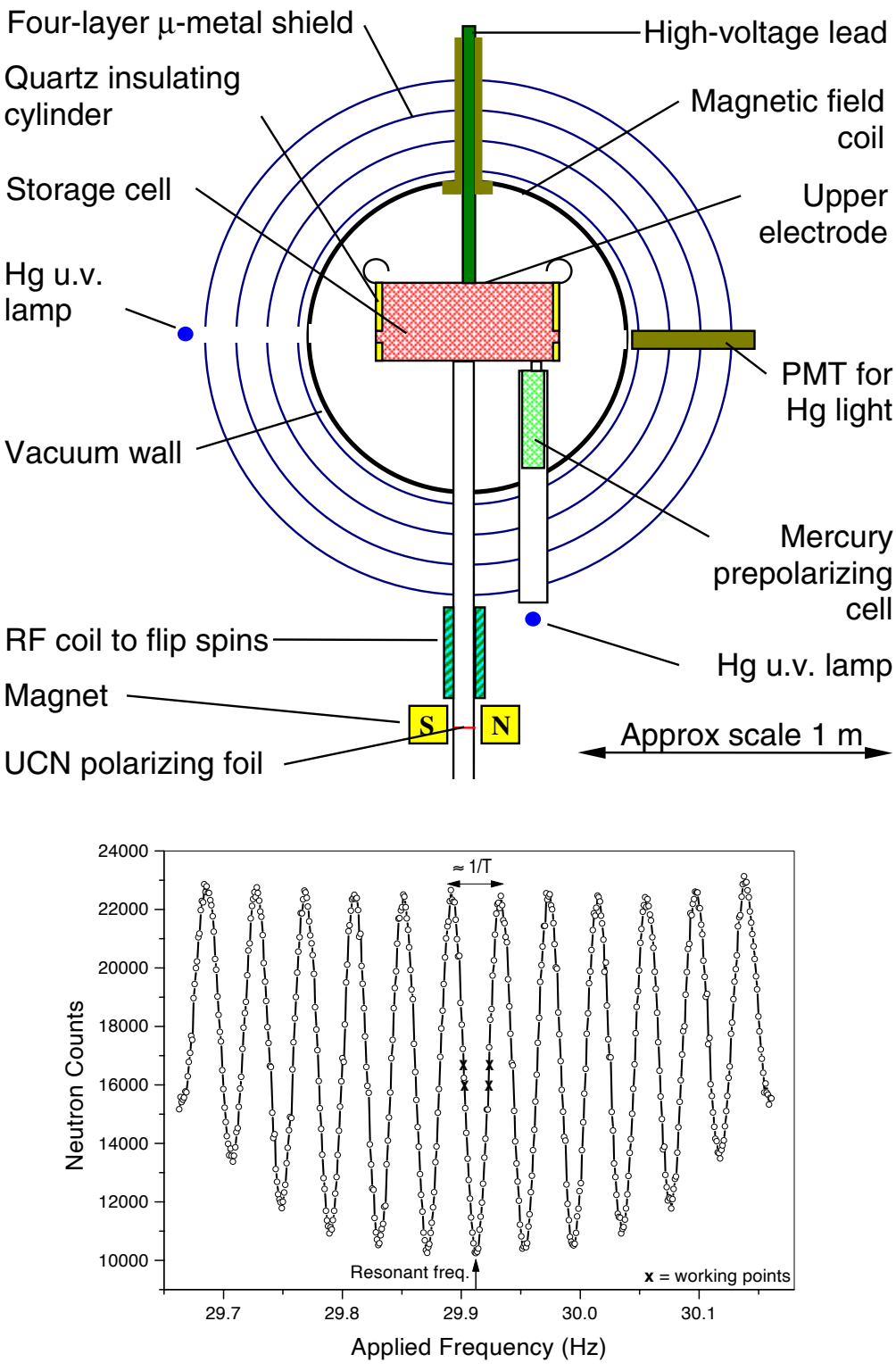

Figure 2.2: A scheme of the UCN method and the Ramsey resonance curve, which are quote from the literature [23, 25].

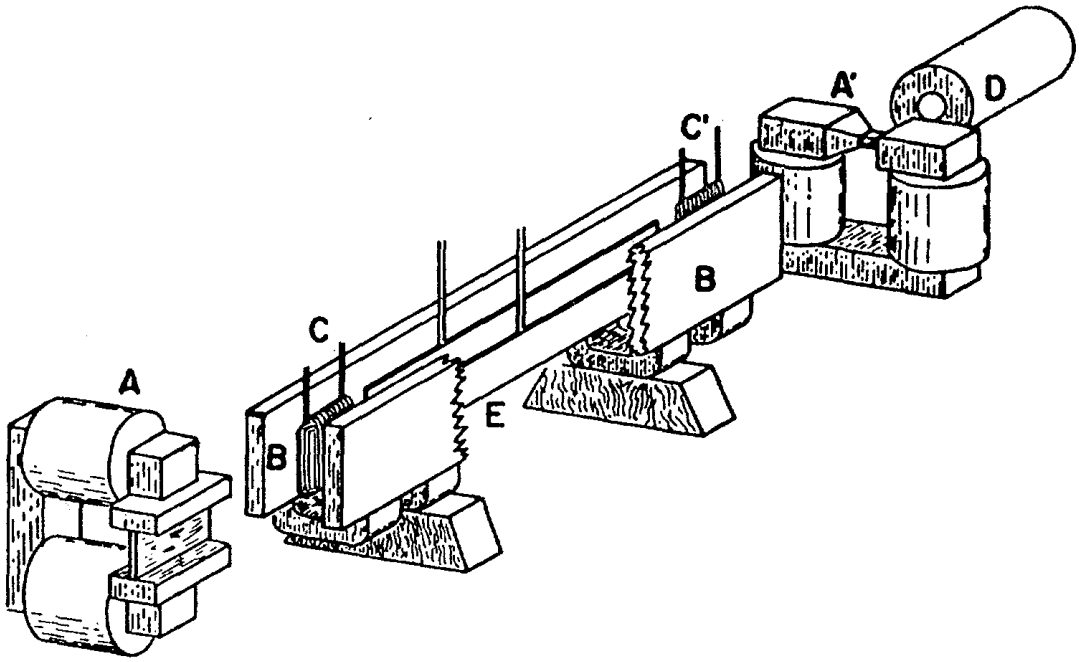

Figure 2.3: Scheme of the first free flight method, which is a quote from the literature [28].
A, the magnetized iron mirror polarizer. A′, the magnetized iron transmission analyzer. B, the pole faces of the homogeneous field magnet. C, C′, the coils for the radio-frequency magnetic field. D, the BF_3 neutron counter. E, the condenser plates that apply the electric field are highly polished nickel-plated copper plates 0.349 cm apart and 135 cm long.

2.3 Free Flight Method

The free flight method was performed by J.H.Smith, E.M.Purcell and N.F.Ramsey in 1957 and gave the first upper limit value of $5 \times 10^{-20}\ e \cdot \mathrm{cm}$ for the purpose of nEDM measurement [28]. The measurement of the frequency of the spin precession in an electromagnetic field and the determination of the nEDM value from the difference in frequency when the direction of the electric field is reversed is the same as the UCN method, and the frequency measurement method is the same as the Ramsey separated-oscillatory-field magnetic resonance. The difference is that thermal neutrons are used. Thermal neutrons are neutrons with energies of about $1 \sim 100$ meV. And instead of storing them in a vessel (thermal neutrons cannot be stored in a vessel), they are flighted freely over a long distance to investigate their precessional motion. Figure 2.3 shows a schematic diagram of the experiment [28].

Thermal neutrons polarized by A fly in the uniform magnetic field indicated by B. E is an electrode that creates an electric field, and the direction of the field can be reversed. C and C′ are Ramsey separated-oscillatory-field. Neutrons analyzed by A′ are counted by the proportional counter D. Compared to the UCN storage method, a strong thermal neutron source can be used, and the number of neutrons counted can be higher, but the interaction time is much longer than that of the UCN storage method. In the case of this experiment, the interaction time is order of 1 msec.

Until the 1970s, this method was the mainstream of nEDM search experiments, but with the development and progress of the UCN storage method, it has not been used until now. However, due to advances in experimental techniques and plans to construct even more powerful thermal neutron sources, plans are underway for experiments with much longer flight distances and beyond the current upper limits [29].

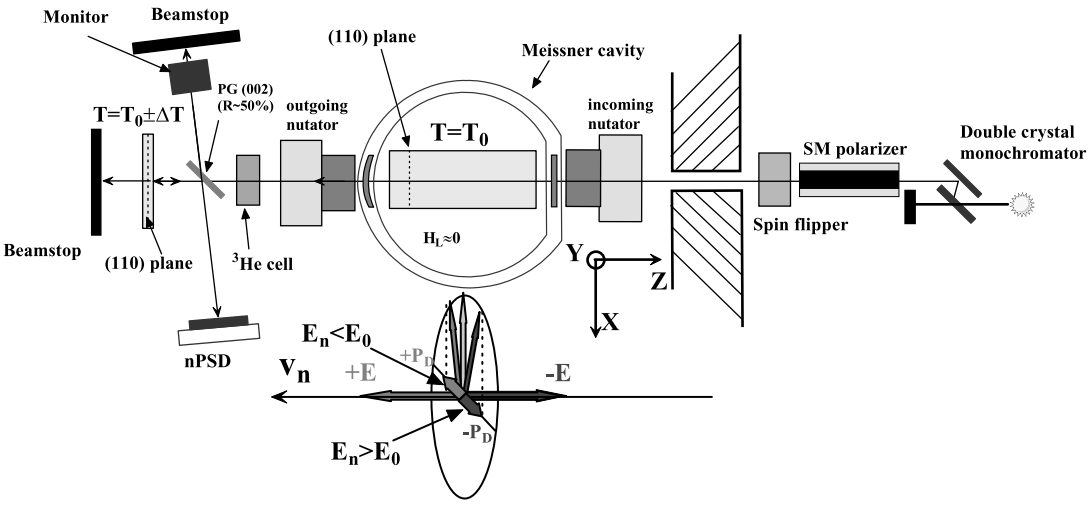

Figure 2.4: Schematic diagram of the crystal diffraction method for nEDM search experiment, which is a quote from Fig.1 of ref. [38].
Neutrons with the wavelength of 0.491 nm selected by the double crystal monochromator are polarized and spin-controlled and injected into the first crystal from the right side of the figure. Crystals are α-quartz. The first crystal is installed in the 3D polarization analysis apparatus (CRYOPAD) and is arranged so that neutrons are injected perpendicular to the crystal plane (110). The second crystal at the rear (left side in the figure) is similarly arranged, but the temperature of both crystals is slightly controlled so that neutrons passing through the first crystal with slightly off the Bragg condition are reflected by the second crystal with the exact Bragg condition. By controlling the spins perpendicular to the intra-crystal electric field and measuring and analyzing the spin polarization due to precession while passing through the first crystal, it is possible to search for nEDM

2.4 Crystal Diffraction Method

The third method, crystal diffraction method, differs from the UCN storage and free-flight methods in the physical quantity measured. In 1967, Shull and Nathans [30] were the first to propose a method using spin rotation due to an electric field in a crystal and obtained an upper limit of $(2.4 \pm 3.9) \times 10^{-22}\ e \cdot \mathrm{cm}$. Later, Forte [31] proposed an nEDM measurement experiment using spin rotation induced by an intra-crystal electric field sensed by diffracted neutrons. The field strength measured at the (110)-plane of α-quartz was $(1.8 \pm 0.2) \times 10^8$ V/cm [32], which is four orders of magnitude stronger than the field strength achievable by the UCN and free flight methods. In 2006, Fedorov et al. proposed a crystal diffraction method based on the Bragg configuration [34, 35] and obtained the value of nEDM of $(2.5 \pm 6.5^{\mathrm{stat}} \pm 5.5^{\mathrm{syst}}) \times 10^{-24}\ e \cdot \mathrm{cm}$ with that method in 2010 [36, 37, 38].

Figure 2.4 shows a schematic diagram of this experiment [38]. A thermal neutron beam enters the experimental setup from the right side of the figure. Neutrons with the wavelength of 0.491 nm selected by the double crystal monochromator (PGM) are polarized by the super mirror polarizer. The direction of polarization can be reversed with a resonance π-flipper. There are two crystals, the first crystal and the second crystal, which are installed so that their crystal planes (110) are parallel (perpendicular to the surface of the paper). The two crystals are controlled to maintain a temperature difference of $\Delta T = +2.0$ K and $\Delta T = -0.4$ K. This makes it possible that neutrons transmitted by the first crystal slightly off the Bragg condition can be reflected by the second crystal at the exact Bragg condition. The first crystal, which is 14 cm in length, is placed in a superconducting magnetically shielded 3D polarization analysis apparatus (CRYOPAD). Spin-controlled neutrons from the CRYOPAD pass through the first crystal with a slight deviation from the Bragg condition, and interact with the electric field in the crystal, resulting in a slight change in polarization due to spin precession. Neutrons coming out of CRYOPAD are analyzed with a ^{3}He spin filter and measured by nPSD after reflected the second crystal and PG. Thus, it is possible to search for nEDM.

This crystal diffraction method, described above, uses the Bragg configuration. Another crystal diffraction method uses the Laue configuration. The Bragg and Laue configurations are discussed in section 3.3. The Laue configuration was proposed by the same Fedorov group [39]. The Bragg configuration method uses

transmitted neutrons that deviate slightly from the Bragg conditions, whereas the Laue configuration uses diffracted neutrons that exactly satisfy the Bragg conditions. The electric field in which neutrons interact within the crystal is maximized when the Bragg condition is satisfied exactly as in the Laue configuration, and is about one orders of magnitude weaker in the Bragg configuration method. Instead, the Bragg configuration has the advantage of increasing the number of neutrons available compared to the Laue configuration.

2.5 Comparison of Three Methods

Although the UCN storage method and the free-flight method differ in that they measure the frequency difference of the Larmor precession, and the crystal diffraction method measures the amount of rotation of the Larmor precession, they both use the Larmor precession in the same way, and their measurement sensitivity depends on the amount of change in the phase of the Larmor precession, which is expressed by Eq. (2.5). Therefore, the measurement sensitivity of EDM, Δd_n, is inversely proportional to the strength of the interacting electric field E and interaction time τ, and inversely proportional to the square root of the number of neutrons N, which is a statistic.

$$\Delta d_n \propto \frac{1}{E\tau\sqrt{N}} \tag{2.6}$$

Table 2.1 shows the characteristics of the three methods. Typical values are given for the parameters that determine the experimental sensitivity of $1 \times 10^{-26}\ e \cdot \mathrm{cm}$ achieved during 100 days are shown. The individual values in Table 2.1 are a mixture of actual and target values.

Table 2.1: Comparison of required parameters of measurement sensitivity for three different measurement methods.
These show the required parameters which realize the experimental sensitivity of $1 \times 10^{-26}\ e \cdot \mathrm{cm}$ achieved during 100 days. Actual and target values exist in order to emphasize the characteristic of three methods.

Parameter	Unit	UCN method	Free flight method	Crystal diffraction method (Laue)
Interaction time τ	sec	$\sim 10^2$	$\sim 10^{-1}$	$\sim 10^{-3}$
Strength of electric field E	V/cm	$\sim 10^4$	$\sim 10^4$	$\sim 10^8$
Count number of neutrons N	sec^{-1}	$\sim 10^2$	$\sim 10^8$	$\sim 10^4$

The main advantage of the UCN method is that it allows a long interaction time, but it is limited by the low neutron intensity. It is difficult to further improve both the interaction time and the electric field strength, and there is a need to improve the neutron intensity. Therefore, the development of more powerful UCN sources is being vigorously pursued [42]. In addition, improvements in the magnetic field environment and cooperating magnetometers are being vigorously pursued to minimize systematic errors due to geometric phase effects caused by magnetic field gradients. For the free flight method, the strong beam intensity is the main advantage, but the shorter interaction time depending on the size of the experimental apparatus is a disadvantage. Therefore, a new plan is underway to increase the flight distance in order to extend the interaction time [29]. According to the report, assuming an interacting flight distance of 50m, the measurement sensitivity of $5 \times 10^{-28}\ e \cdot \mathrm{cm}$ can be achieved. The challenge of systematic uncertainties due to magnetic field gradients is expected to become more difficult as the size of device increases.

The crystal diffraction method we are aiming for has fewer experiments than the UCN storage method, and its upper limit is still two orders of magnitude behind. As shown in Table 1, the electric field strength is overwhelmingly favorable compared to the other methods, but the interaction time and statistics are bottlenecks. In the Bragg configuration method, the statistics are relatively favorable, but the interaction time is short. Therefore, a new idea has been proposed to increase the interaction time by making neutrons go back and forth passing through the crystal [40, 41]. On the other hand, the Laue configuration method diffracts

the Bragg angle closer to 90 degrees, which increases the interaction time, but it is still on the order of 1 msec. Furthermore, the strength of the diffracted neutrons is currently about 1 cps, and the statistics are 4 orders of magnitude lower than the statistics in Table 1. This is the reason why the sensitivity is two orders of magnitude lower than the UCN method.

3 Dynamical Diffraction Theory

In this section, a theoretical description of the behavior of neutrons in a crystal is given.

In real crystals, the complete crystal structure exists only in mosaic blocks, which are small crystal grains. A macroscopic crystal is an a collection of such mosaic blocks. While diffraction phenomena such as a single reflection in a small mosaic block can be described by kinematic diffraction theory, a large perfect crystal or a mosaic crystal with a well-aligned mosaic blocks has a large coherent region, and so the effect of multiple diffraction must be considered. The dynamical theory is a theory that deals with such multiple diffraction phenomena in perfect crystals.

X-ray diffraction was discovered by M. von Laue in 1912, and the dynamical diffraction theory was first developed in the X-ray diffraction field by C.G. Darwin [43, 44], P.P. Ewald [45, 46], and M.v. Laue [47], each in their each own way, Ewald developed the theory in terms of the sequential oscillation, scattering, and propagation of an incident X-ray wave by considering a crystal as a set of dipoles in a three-dimensional lattice, while Laue replaced the point-like dipoles with a continuous electron density distribution. The theory was then developed into a dynamical theory of electron diffraction, and the first dynamical formulation of the neutron theory was given by Goldberger and Seitz [48] in 1947. Review papers summarizing neutron diffraction include Sears [49] and Rauch [50], and so on.

The most important difference between X-ray and neutron dynamical theory is the interaction potential in a crystal. For X-rays, the crystal structure factor is derived from the electron distribution in the crystal cell. For neutrons, on the other hand, it is the very localized neutron-nucleus interaction, which is given by the Fermi pseudo potential. The crystal structure factor is determined by the scattering length of the nuclei describing the neutron-nucleus interaction. Furthermore, due to the relatively low absorption of neutrons, the dynamical diffraction effects occur, which can only be observed in thin crystals in X-rays.

Here we treat and discuss the dynamical diffraction theory based on the basic plane-wave theory.

3.1 The Interaction Potential of a Neutron in a Non-Magnetic Crystal

The interaction potential of a neutron in a nonmagnetic crystal can be written as the sum of the nuclear force potential with the nucleus, the relativistic magnetic field potential and the electric field potential of the nEDM;

$$V(\boldsymbol{r}) = V^{\mathrm{N}}(\boldsymbol{r}) + V^{\mathrm{S}}(\boldsymbol{r}) + V^{\mathrm{E}}(\boldsymbol{r}). \tag{3.1}$$

The nuclear force potential can be written in terms of the Fermi pseudo-potential as

$$V^{\mathrm{N}}(\boldsymbol{r}) = \frac{2\pi\hbar^2}{m_n} \sum_{n,d} b_{\mathrm{c}}^d \delta\left(\boldsymbol{r} - \boldsymbol{R}_n - \boldsymbol{\rho}_d\right). \tag{3.2}$$

This equation will be discussed in the next section. The relativistic magnetic field potential is the interaction potential between the neutron magnetic moment and the relativistic magnetic field sensed by a neutron moving in an electric field. In a crystal, there is an electric potential due to the distribution of nuclei and electrons. A neutron propagating through a crystal feels a potential averaged by its probability density. Let it be called the effective intra-crystal electric field in this paper. The relativistic magnetic field potential can be written as

$$V^{\mathrm{S}}(\boldsymbol{r}) = -\mu_n \frac{\boldsymbol{\sigma} \cdot [\boldsymbol{E} \times \boldsymbol{v}]}{c^2}. \tag{3.3}$$

The interaction potential between nEDM and its effective intra-crystal electric field is given by

$$V^{\mathrm{E}}(\boldsymbol{r}) = -d_n \boldsymbol{\sigma} \cdot \boldsymbol{E}. \tag{3.4}$$

As a typical example, in the (110)-plane of α-quartz with the Bragg angle of 30 degrees, if the intra-crystal electric field is 2.0×10^8 V/cm and the value of nEDM is $1.8 \times 10^{-26}\, e \cdot \mathrm{cm}$, the respective magnitudes are $V^{\mathrm{N}} = 36$ neV, $V^{\mathrm{S}} = 2.2 \times 10^{-2}$ neV and $V^{\mathrm{E}} = 3.6 \times 10^{-9}$ neV. Since the nuclear force potential is by far the largest, it can be treated as $V(\boldsymbol{r}) \simeq V^{\mathrm{N}}(\boldsymbol{r})$ in this section, which would discuss wave fields in a crystal.

3.2 Crystal Structure Factor

As mentioned above, when discussing diffraction phenomena, we only need to consider V^{N}, since V^{S} and V^{E} are much smaller than V^{N}. Hereafter, $V^{\mathrm{N}}(\boldsymbol{r}) = V(\boldsymbol{r})$. Since $V(\boldsymbol{r})$ has the periodicity of the crystal, it can be Fourier expanded using the reciprocal lattice vector.

$$V(\boldsymbol{r}) = \sum_{\boldsymbol{g}} V_{\boldsymbol{g}} \exp(\mathrm{i}\boldsymbol{g}\cdot\boldsymbol{r}). \tag{3.5}$$

The reciprocal lattice vector $\boldsymbol{g}$ of the crystal plane with the Miller index $(h\ k\ l)$ is represented as

$$\boldsymbol{g} = h\boldsymbol{G}_1 + k\boldsymbol{G}_2 + l\boldsymbol{G}_3, \tag{3.6}$$

where $\boldsymbol{G}_1$, $\boldsymbol{G}_2$ and $\boldsymbol{G}_3$ are the basic reciprocal lattice vector and defined as

$$\boldsymbol{G}_1 = 2\pi\frac{[\boldsymbol{b}\times\boldsymbol{c}]}{v_{\mathrm{c}}},\ \boldsymbol{G}_2 = 2\pi\frac{[\boldsymbol{c}\times\boldsymbol{a}]}{v_{\mathrm{c}}},\ \boldsymbol{G}_3 = 2\pi\frac{[\boldsymbol{a}\times\boldsymbol{b}]}{v_{\mathrm{c}}}, \tag{3.7}$$

where $\boldsymbol{a}, \boldsymbol{b}$, and $\boldsymbol{c}$ are the crystal lattice vectors and v_{c} is the volume of a unit cell. $V_{\boldsymbol{g}}$ can be written as follows by inverse Fourier transforming Eq. (3.5) and using Eq. (3.2).

$$\begin{aligned} V_{\boldsymbol{g}} &= \frac{1}{v_{\mathrm{c}}N_{\mathrm{c}}}\int V(\boldsymbol{r})\exp(-\mathrm{i}\boldsymbol{g}\cdot\boldsymbol{r})\mathrm{d}\boldsymbol{r} \\ &= \frac{1}{v_{\mathrm{c}}N_{\mathrm{c}}}\frac{2\pi\hbar^2}{m_n}\sum_{n,d}\int b_{\mathrm{c}}^{d}\delta\left(\boldsymbol{r}-\boldsymbol{R}_n-\boldsymbol{\rho}_d\right)\exp(-\mathrm{i}\boldsymbol{g}\cdot\boldsymbol{r})\mathrm{d}\boldsymbol{r} \\ &= \frac{2\pi\hbar^2}{m_n v_{\mathrm{c}}}F_{\boldsymbol{g}}, \end{aligned} \tag{3.8}$$

where N_{c} is the number of a unit cell and b_{c}^{d} is the bound coherent scattering length of a nucleus d positioned at $\boldsymbol{\rho}_d$ that is the position vector in a unit cell and $\boldsymbol{R}_n$ is the position vector of a unit cell (see Fig. 3.1). The relation with the bound coherent scattering length and free coherent scattering length a_{c}^{d} is

$$b_{\mathrm{c}}^{d} = \frac{m_d + m_n}{m_d}a_{\mathrm{c}}^{d}, \tag{3.9}$$

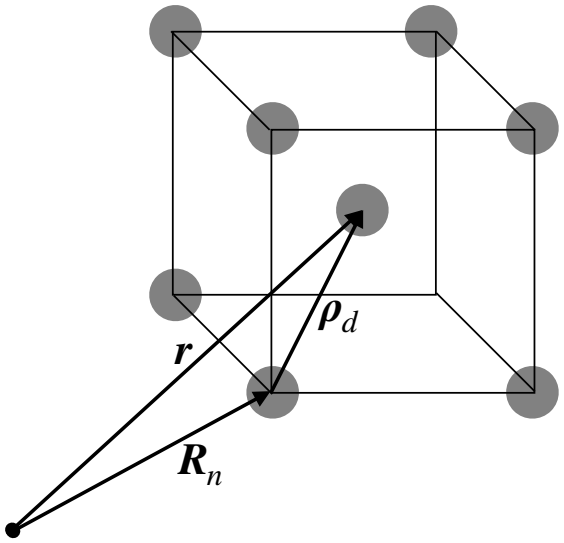

Figure 3.1: The nucleus position in a unit cell

where m_d is the mass of nucleus d. $F_{\boldsymbol{g}}$ is the crystal structure factor.

$$F_{\boldsymbol{g}} = \sum_d b_{\mathrm{c}} c^d \exp(-\mathrm{i}\boldsymbol{g}\cdot\boldsymbol{\rho}_d). \tag{3.10}$$

Here we assume that the atoms are stationary at their respective positions in the crystal lattice, but in fact they are thermally oscillating around their equilibrium positions, depending on the temperature of the crystal. If the deviation of the d-th atom in the unit cell from its equilibrium position is denoted by $\boldsymbol{\delta}_d(t)$, the position of the atom can be written as

$$\boldsymbol{\rho}_d(t) = \boldsymbol{\rho}_d + \boldsymbol{\delta}_d(t). \tag{3.11}$$

The crystal structure factor can then be written as

$$\begin{aligned} F_{\boldsymbol{g}} &= \sum_d b_{\mathrm{c}}^d \exp\left[-\mathrm{i}\boldsymbol{g}\cdot(\boldsymbol{\rho}_d + \boldsymbol{\delta}_d)\right] \\ &= \sum_d b_{\mathrm{c}}^d \exp(-\mathrm{i}\boldsymbol{g}\cdot\boldsymbol{\rho}_d)\left[1 - \mathrm{i}\boldsymbol{g}\cdot\boldsymbol{\rho}_d - \frac{1}{2}(\boldsymbol{g}\cdot\boldsymbol{\delta}_d)^2 + \cdots\right]. \end{aligned} \tag{3.12}$$

If the oscillations are spatially random, the average is considered to be the same as the time average of the oscillations. Therefore when the time average is expressed by $< \cdots >$, the crystal structure factor can be approximated as follows, considering that the odd power term is zero.

$$\begin{aligned} F_{\boldsymbol{g}} &= \sum_d b_{\mathrm{c}}^d \exp(-\mathrm{i}\boldsymbol{g}\cdot\boldsymbol{\rho}_d) \exp\left[-\frac{1}{2} < (\boldsymbol{g}\cdot\boldsymbol{\delta}_d)^2 >\right] \\ &= \sum_d b_{\mathrm{c}}^d \exp(-\mathrm{i}\boldsymbol{g}\cdot\boldsymbol{\rho}_d) \exp(-W_d), \end{aligned} \tag{3.13}$$

$$\begin{aligned} W_d &= \frac{1}{2} < (\boldsymbol{g}\cdot\boldsymbol{\delta}_d)^2 \\ &= 8\pi^2 < \delta_{d\perp}^2 > \frac{\sin^2\theta_{\mathrm{B}}}{\lambda^2}, \end{aligned} \tag{3.14}$$

where $\delta_{d\perp}$ is the vibration component perpendicular to the diffraction plane. The effect of thermal oscillation can be expressed by multiplying the scattering length b_{c}^d by $\exp(-W_d)$, and this $\exp(-W_d)$ is called the Debye-Waller factor.

In this study, we used α-quartz, a low-temperature SiO_2 crystal. Silicon dioxide (SiO_2) has a variety of crystal structures at different temperatures and pressures. α-quartz, which is trigonal at room temperature at 1 atmosphere, undergoes a phase transition to hexagonal β-quartz at 573°C. β-quartz is fully hexagonal and has a six-fold rotational symmetry axis, whereas α-quartz is trigonal and has only a three-fold rotational symmetry axis due to slight comtraction. This contraction leads to non-centrosymmetry. α-quartz (and β-quartz) has a spiral structure, and a crystal with a left-handed spiral is called a right-handed quartz, which shows right-handed rotatory polarization. α-quartz with a right-handed spiral is called a left-handed quartz, and it exhibits left-handed rotatory polarization. Right-handed quartz and left-handed quartz are optical isomers of each other. In this study, artificial α-quartz was used, which is right-handed α-quartz.

Figure 3.2 show the crystal structure and atomic configuration coordinates of α-quartz. The coordinate values are normalized by the cell size. The magnitudes of thermal vibrations of Si and O atoms in α-quartz at room temperature are

$$< \delta_{\mathrm{Si}\perp}^2 > \sim 0.006, \quad < \delta_{\mathrm{O}\perp}^2 > \sim 0.017, \tag{3.15}$$

and the magnitude of each Debye-Waller factor is ~ 0.98 and ~ 0.95, respectively. The crystal structure factors for several crystal planes of α-quartz can be calculated using the atomic configuration coordinates in Fig. 3.2.

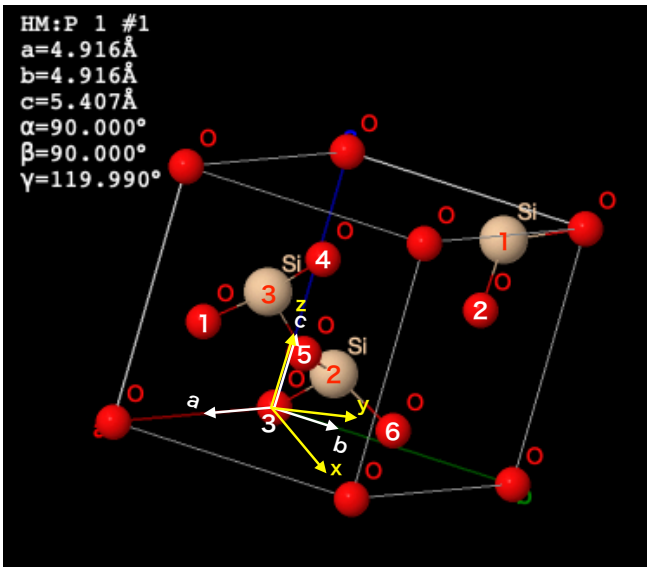

Atom coordinates

Atom	a	b	c
O 1	0.8521	0.1465	0.4281
O 2	0.3172	0.8787	0.6648
O 3	0	0	0
O 4	0.731	0.4647	0.7627
O 5	0.4386	0.3189	0.3317
O 6	0.1722	0.5861	0.0958
Si 1	0.0551	0.7326	0.8801
Si 2	0.1149	0.2626	0.2135
Si 3	0.585	0.2021	0.5467

Figure 3.2: The crystal structure and atom coordinates of α-quartz.
The crystal structure of α-quartz and the positions of its constituent atoms within the unit cell. The coordinate values are expressed in terms of the lattice vectors $\boldsymbol{a}$, $\boldsymbol{b}$, and $\boldsymbol{c}$, normalized by the unit cell size (lattice constant). One unit cell contains three SiO_2 molecules. Quated from AtomWork.

3.3 One Wave Approximation

Consider the case of a perfectly collimated parallel neutron beam with a fixed wavelength incident on a crystal. Since the actual neutron beam has a wavelength spread and a finite divergence angle, it cannot simply be described by a monochromatic plane wave. However, considering that neutrons are described by a single-particle wave function because of a Fermi particle, we can consider the neutron beam to be an ensemble of monochromatic plane waves with a spread of wave-number space. The wave function of a neutron flying freely in vacuum and injected on a crystal with a wave number vector $\boldsymbol{k}$ is

$$\psi_{\text{in}}(\boldsymbol{r}) = u_{\text{in}} \exp(\mathrm{i}\boldsymbol{k}\cdot\boldsymbol{r}), \tag{3.16}$$

where u_{in} denotes the amplitude of the wave function and $|\psi_{\text{in}}(\boldsymbol{r})|^2 = u_{\text{in}}^2$ is a space density of neutrons. Since diffraction experiments with neutron beams are generally stationary, the time factor is omitted. Neutrons incident on a crystal interact with a potential $V(\boldsymbol{r})$ in a crystal and their wave motion is described by the Schrödinger equation

$$\left[-\frac{\hbar^2}{2m_n}\nabla^2 + V(\boldsymbol{r})\right]\Psi_{\text{cry}}(\boldsymbol{r}) = E\Psi_{\text{cry}}(\boldsymbol{r}), \tag{3.17}$$

where E is the energy of the neutron and m_n is the mass of the neutron. Due to the periodic boundary conditions of the crystal, the wave function of the neutron can be described as a superposition of Bloch waves with a wave number vector $\boldsymbol{K}^{(j)}$;

$$\Psi_{\text{cry}}(\boldsymbol{r}) = \sum_j u^{(j)}(\boldsymbol{r}) \exp\left(\mathrm{i}\boldsymbol{K}^{(j)}\cdot\boldsymbol{r}\right). \tag{3.18}$$

The wave number vector of the waves in a crystal is denoted by a capital letter $\boldsymbol{K}^{(j)}$, and $u^{(j)}(\boldsymbol{r})$ denotes the amplitude of the wave field. The suffix (j) is the label of each Bloch wave field. The amplitude $u^{(j)}(\boldsymbol{r})$ can be Fourier expanded in terms of the reciprocal lattice vector $\boldsymbol{g}$ as same as the potential $V(\boldsymbol{r})$ in Eq. (3.5).

$$u^{(j)}(\boldsymbol{r}) = \sum_{\boldsymbol{g}} u_{\boldsymbol{g}}^{(j)} \exp(\mathrm{i}\boldsymbol{g}\cdot\boldsymbol{r}). \tag{3.19}$$

Substituting Eq. (3.18), (3.19) and (3.5) into Eq. (3.17), a homogenous system of equations for $u_{\boldsymbol{g}}^{(j)}$ can be obtained as

$$\left[-\frac{\hbar^2}{2m_n}\left(\boldsymbol{K}^{(j)}+\boldsymbol{g}\right)^2-E\right]u_{\boldsymbol{g}}^{(j)}=-\sum_{\boldsymbol{g}}V_{\boldsymbol{g}-\boldsymbol{g}'}u_{\boldsymbol{g}'}^{(j)}. \tag{3.20}$$

The ratio of $V_{\boldsymbol{g}}$ to the thermal neutron energy $E=\hbar^2k^2/2m_n$ is of the order of $\sim 10^{-5}$. For example, the thermal neutron energy at a wavelength of 2.5 Å is about 13 meV and $V_{\boldsymbol{g}}$ of (110)-crystal plane of α-quartz is 52.5 neV, so $V_{\boldsymbol{g}}/E\sim 4\times 10^{-6}$. This small ratio can be used to approximately solve for $u_{\boldsymbol{g}}^{(j)}$.

The homogenous equation Eq. (3.20) for the Fourier coefficient $u_{\boldsymbol{g}}^{(j)}$ of $u^{(j)}(\boldsymbol{r})$ can be written as follows,

$$\frac{\left(\boldsymbol{K}^{(j)}+\boldsymbol{g}\right)^2-\boldsymbol{k}^2}{k^2}u_{\boldsymbol{g}}^{(j)}=\sum_{\boldsymbol{g}'}\frac{V_{\boldsymbol{g}-\boldsymbol{g}'}}{E}u_{\boldsymbol{g}'}^{(j)}\quad(j=0,1,2,\cdots). \tag{3.21}$$

The coefficient V/E appearing on the right-hand side is very small for thermal neutrons, of the order of 10^{-5}, so for $u_{\boldsymbol{g}}^{(j)}$ to have a significant magnitude must be

$$\left(\boldsymbol{K}^{(j)}+\boldsymbol{g}\right)^2-\boldsymbol{k}^2\cong 0. \tag{3.22}$$

This is satisfied only if $\boldsymbol{g}=0$ or if a particular $\boldsymbol{g}$ satisfies the following general Bragg condition;

$$\lambda=2d_g\sin\theta_{\mathrm{B}}, \tag{3.23}$$

where $\lambda=2\pi/K$ is a wavelength of a neutron and $d_g=2\pi/g$ is a lattice spacing corresponding to a reciprocal lattice vector $\boldsymbol{g}$. If there is no $\boldsymbol{g}$ such that the Bragg condition is satisfied, then Eq. (3.21) becomes only a linear equation for $u_0^{(j)}$;

$$\left[\frac{\hbar^2}{2m}K^{(j)2}-E\right]u_0^{(j)}=-V_0^{(j)}u_0^{(j)}. \tag{3.24}$$

Strictly, the wave field corresponding to $u_{\boldsymbol{g}}^{(j)}(\boldsymbol{g}\neq 0)$ is also excited in a crystal, but its intensity is very small, of the order of $\sim 10^{-10}$, and can be neglected in practice. This approximation, in which only the wave field corresponding to $\boldsymbol{g}=0$ exists, is called the one-wave approximation. This is the case when there is no crystal plane $\boldsymbol{g}$ that satisfies the Bragg condition.

By solving Eq. (3.24), $\boldsymbol{K}^{(j)}$ is uniquely determined, which we will write as $\boldsymbol{K}_0$. Its magnitude is

$$K_0\approx k\left(1-\frac{V_0}{2E}\right)=k(1-\varepsilon), \tag{3.25}$$

where

$$\varepsilon=\frac{V_0}{2E}\ll 1. \tag{3.26}$$

Writing $u_0^{(j)}$ as u_0, the wave field in a crystal $\Psi_{\mathrm{cry}}(\boldsymbol{r})$ can be written as

$$\Psi_{\mathrm{cry}}(\boldsymbol{r})=u_0\exp\left(\mathrm{i}\boldsymbol{K}_0\cdot\boldsymbol{r}\right) \tag{3.27}$$

In the case of the one wave approximation, when a neutron of wave number vector $\boldsymbol{k}$ enters a crystal, only one wave field of wave number vector $\boldsymbol{K}_0$ is excited inside the crystal, which is lower in energy by the internal potential V_0. According to Eq. (3.13),

$$F_0=\sum_d b_{\mathrm{c}}^d\exp(-W_d)=b_{\mathrm{c}}Nv_{\mathrm{c}}, \tag{3.28}$$

where

$$b_{\mathrm{c}}=\frac{\sum_d b_{\mathrm{c}}^d\exp(-W_d)}{Nv_{\mathrm{c}}}, \tag{3.29}$$

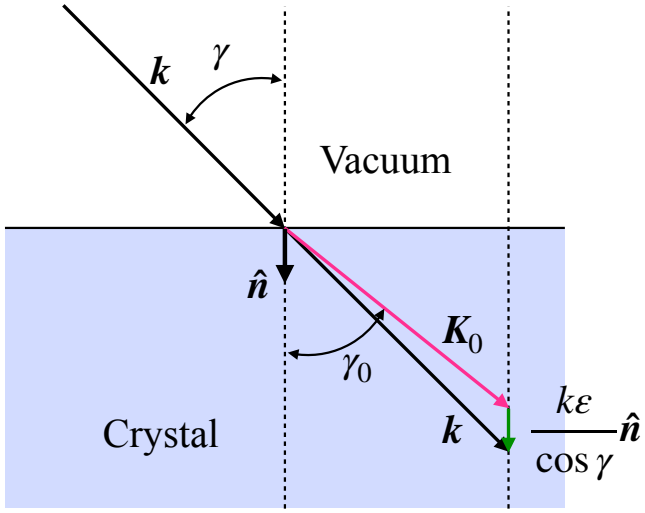

Figure 3.3: Schematic diagram of one wave approximation:
$\hat{\boldsymbol{n}}$:Unit normal vector of the incident plane. $\boldsymbol{k}$:Wave number vector of the incident wave in vacuum. $\boldsymbol{K}_0$:Wave number vector of the diffracted wave in a crystal. γ and γ_0 is the angle between $\hat{\boldsymbol{n}}$ with $\boldsymbol{k}$ and $\boldsymbol{K}_0$, respectively.

and from Eq. (3.8)

$$V_0 = \frac{2\pi\hbar^2 F_0}{m_n v_c} = \frac{2\pi\hbar^2 b_c N}{m_n}, \tag{3.30}$$

where N is a number density of nucleus and so Nv_c is a number of nucleus in a unit cell. b_c is called the average bounded scattering length. V_0 is also called the optical potential.

The relation between $\boldsymbol{k}$ and $\boldsymbol{K}_0$ is shown in Fig. 3.3. When $\hat{\boldsymbol{n}}$ is the unit normal vector of the incident plane toward the inside of the crystal, the incident angle is γ and refraction angle is γ_0,

$$\boldsymbol{K}_0 = \boldsymbol{k} - \frac{k\varepsilon}{\cos\gamma}\hat{\boldsymbol{n}}. \tag{3.31}$$

From the conservation of momentum in the tangential direction of the incident plane,

$$K_0 \sin\gamma_0 = k\sin\gamma, \tag{3.32}$$

$$\xi = \frac{\sin\gamma}{\sin\gamma_0} = \frac{K_0}{k} = 1-\varepsilon. \tag{3.33}$$

ξ is the refractive index and this is the Snell's law.

3.4 Two Wave Approximation

If there is a $\boldsymbol{g}$ other than $\boldsymbol{g}=0$ that satisfies Eq. (3.22), i.e., satisfies the Bragg condition, Eq. (3.21) becomes a binary system of $u_0^{(j)}$ and $u_{\boldsymbol{g}}^{(j)}$. This approximation, which assumes that only two waves, the refracted wave at $\boldsymbol{g}=0$ (hereafter referred to as the transmitted wave) and the reflected wave at $\boldsymbol{g}$, which satisfy the Bragg condition, have significant magnitude, and that other waves can be ignored, is called the two-wave approximation. Each of the transmitted and reflected waves actually has two more wave components, as we will see below.

From Eq. (3.21),

$$\begin{cases} \left[\dfrac{\hbar^2}{2m_n}\boldsymbol{K}^{(j)2} - E + V_0\right]u_0^{(j)} + & V_{-\boldsymbol{g}}u_{\boldsymbol{g}}^{(j)} = 0 \\ V_{\boldsymbol{g}}u_0^{(j)} + & \left[\dfrac{\hbar^2}{2m_n}\left(\boldsymbol{K}^{(j)}+\boldsymbol{g}\right)^2 - E + V_0\right]u_{\boldsymbol{g}}^{(j)} = 0 \end{cases} \tag{3.34}$$

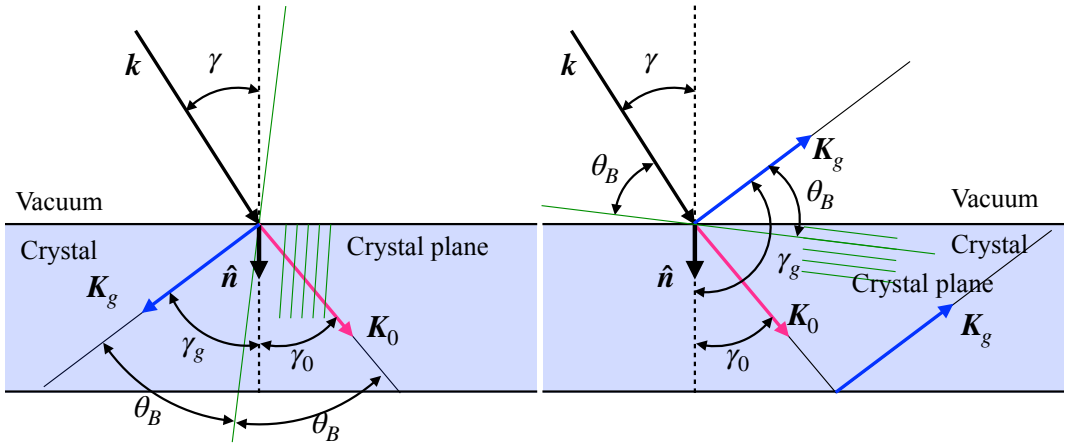

(a) Laue configulation : $b \equiv \dfrac{\cos\gamma_0}{\cos\gamma_g} > 0$ (b) Bragg configulation : $b \equiv \dfrac{\cos\gamma_0}{\cos\gamma_g} < 0$

Figure 3.4: Schematic diagram of Laue and Bragg configurations:
(a) Laue configuration: no reflected waves exist on the incident side.
(b) Bragg configuration: reflected waves exist on the incident side.

For this binary system of equations to have a non-zero solution, the eigenvalue equation must be zero.

$$\begin{vmatrix} \left[\frac{\hbar^2}{2m_n}\boldsymbol{K}^{(j)2} - E + V_0\right] & V_{-\boldsymbol{g}} \\ V_{\boldsymbol{g}} & \left[\frac{\hbar^2}{2m_n}\left(\boldsymbol{K}^{(j)} + \boldsymbol{g}\right)^2 - E + V_0\right] \end{vmatrix} = 0 \tag{3.35}$$

Introduce the following parameters;

$$\alpha \equiv \frac{|\boldsymbol{k}+\boldsymbol{g}|^2 - |\boldsymbol{k}|^2}{|\boldsymbol{k}|^2} = \frac{\boldsymbol{g}^2 + 2\boldsymbol{k}\cdot\boldsymbol{g}}{k^2} = 2(\theta_{\mathrm{B}} - \theta)\sin 2\theta_{\mathrm{B}}, \tag{3.36}$$

$$b \equiv \frac{\cos\gamma_0}{\cos\gamma_g}, \quad \cos\gamma_0 = \hat{\boldsymbol{K}}_0 \cdot \hat{\boldsymbol{n}}, \quad \cos\gamma_g = \hat{\boldsymbol{K}}_{\boldsymbol{g}} \cdot \hat{\boldsymbol{n}} \tag{3.37}$$

Here, to clarify the meaning of the parameters α and b, the Laue and Bragg configurations are explained. As shown in Fig. 3.4, the Laue configuration has no reflected waves on the incident side, while the Bragg configuration has reflected waves on the incident side. γ_0 and γ_g are the angles between the inside normal vector $\hat{\boldsymbol{n}}$ of the crystal with the transmitted wave vector $\boldsymbol{K}_0$ and the reflected wave vector $\boldsymbol{K}_g$, respectively. From the definition of the parameter b (Eq. (3.37)), $b > 0$ for the Laue configuration and $b < 0$ for the Bragg configuration. In particular, when $b = 1$, it is called the symmetric Laue configuration, and when $b = -1$, it is called the symmetric Bragg configuration. This is equivalent to the symmetric Laue configuration when the crystal plane is perpendicular to the incident plane and the symmetric Bragg configuration when it is parallel to the incident plane.

As Eq. (3.36) indicates, α is a quantity proportional to the magnitude of the deviation of the incident angle θ from the Bragg angle θ_{B}, and it represents the percentage change in the magnitude of the reflected wave number vector when the incident angle is shifted by $(\theta_{\mathrm{B}} - \theta)$. Naturally, if there is no deviation from the Bragg angle, $\alpha = 0$.

Using Eq. (3.26), (3.31) and parameters of α and b, the eigenvalue equation Eq. (3.35) can be rewritten as follows.

$$\begin{vmatrix} -2\varepsilon + V_0/E & V_{-\boldsymbol{g}}/E \\ V_{\boldsymbol{g}}/E & -2\varepsilon/b + \alpha + V_0/E \end{vmatrix} = 0 \tag{3.38}$$

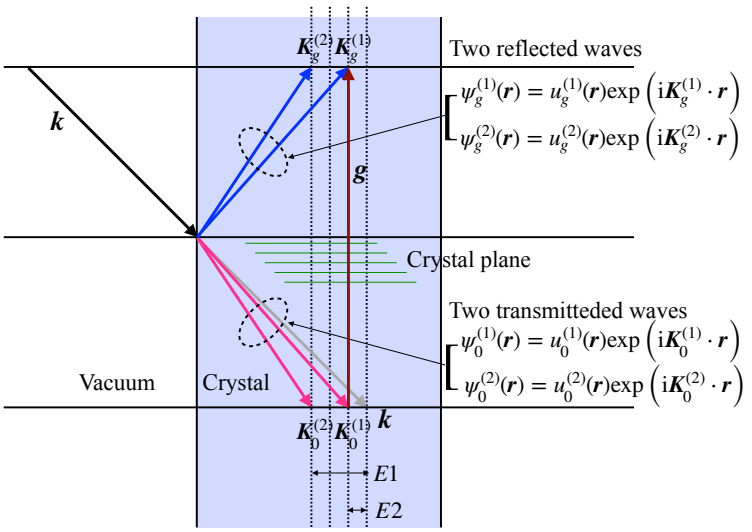

Figure 3.5: Schematic diagram of two wave approximation in the symmetric Laue configuration:
The incident wavenumber vector $\boldsymbol{k}$ splits into a transmitted wave and a reflected wave in a crystal, each of which consists of a wave with a slightly larger wavenumber vector (called the α-wave $\psi_0^{(1)}$ and $\psi_g^{(1)}$) and a slightly smaller wavenumber vector (called the β-wave $\psi_0^{(2)}$ and $\psi_g^{(2)}$). $E1$ corresponds to the decrease of β-wavenumber vector and $E2$ corresponds to the decrease of α-wavenumber vector due to the periodic potential energy $V_{\boldsymbol{g}}$.

Solving this yields two eigenvalues $\varepsilon_1, \varepsilon_2$,

$$\varepsilon_{1,2} = \frac{1}{4}\left[\alpha b + \frac{V_0}{E}(1+b) \pm \sqrt{\left(\alpha b - (1-b)\frac{V_0}{E}\right)^2 + 4b\frac{V_g V_{-g}}{E^2}}\right]. \tag{3.39}$$

This allows for the two wavenumber vectors of the transmitted waves and reflected waves. Respectively, from Eq. (3.31),

$$\boldsymbol{K}_0^{(1,2)} = \boldsymbol{k} - \frac{k\varepsilon_{1,2}}{\cos\gamma}\hat{\boldsymbol{n}}, \tag{3.40}$$

$$\boldsymbol{K}_g^{(1,2)} = \boldsymbol{k} + \boldsymbol{g} - \frac{k\varepsilon_{1,2}}{\cos\gamma}\hat{\boldsymbol{n}}. \tag{3.41}$$

There are a total of four waves in a crystal, and the wave function inside the crystal Ψ_{cry} is a superposition of these waves.

$$\begin{aligned}\Psi_{\text{cry}}(\boldsymbol{r}) &= \psi_0^{(1)}(\boldsymbol{r}) + \psi_0^{(2)}(\boldsymbol{r}) + \psi_g^{(1)}(\boldsymbol{r}) + \psi_g^{(2)}(\boldsymbol{r}) \\ &= u_0^{(1)}\exp\left(i\boldsymbol{K}_0^{(1)}\cdot\boldsymbol{r}\right) + u_0^{(2)}\exp\left(i\boldsymbol{K}_0^{(2)}\cdot\boldsymbol{r}\right) \\ &\qquad + u_g^{(1)}\exp\left(i\boldsymbol{K}_g^{(1)}\cdot\boldsymbol{r}\right) + u_g^{(2)}\exp\left(i\boldsymbol{K}_g^{(2)}\cdot\boldsymbol{r}\right)\end{aligned} \tag{3.42}$$

Figure 3.5 schematically shows the wave field in the crystal in the two-wave approximation using wavenumber vectors in the case of a symmetric Laue configuration. The incident neutron with wavenumber vector $\boldsymbol{k}$ splits into a transmitted wave and a reflected wave in the crystal, each of which consists of a wave with a slightly larger wavenumber vector (called the α wave) $\psi_0^{(1)}$, $\psi_g^{(1)}$ and a slightly smaller wavenumber vector (called the β wave) $\psi_0^{(2)}$, $\psi_g^{(2)}$. The transmitted wave is refracted by the optical potential as in the one-wave approximation, and the reflected wave is reflected by the momentum transfer corresponding to the reciprocal lattice vector. The fact that each wave is composed of two waves with slightly different wavenumber vector magnitudes corresponds to eigenvalues of periodic nuclear potential owing to the crystal lattice. For the case of symmetric Laue configurations, Eq. (3.39) becomes

$$\varepsilon_{1,2} = \frac{1}{4}\left[\alpha + \frac{2V_0}{E} \pm \sqrt{\alpha^2 + 4\frac{V_g V_{-g}}{E^2}}\right] \tag{3.43}$$

If $V_g = V_{-g}$ and V_g/E is approximated as small, we get further

$$\varepsilon_1 = \frac{V_0}{2E} + \frac{1}{2}\alpha + \frac{V_g^2}{2E^2}, \tag{3.44}$$

$$\varepsilon_2 = \frac{V_0}{2E} + \frac{1}{2}\alpha - \frac{V_g^2}{2E^2}. \tag{3.45}$$

3.5 Wave Field Inside a Plane Slab in the Laue Configuration

When a monochromatic plane wave is incident on a crystal, satisfying the Bragg condition at crystal plane $\boldsymbol{g}$, the wave field in the crystal is represented by Eq. (3.42). Its amplitudes, $u_0^{(1,2)}$ and $u_g^{(1,2)}$, are determined from the boundary conditions. In the Laue configuration, there is no reflected wave at the crystal plane of incidence $(\hat{\boldsymbol{n}} \cdot \boldsymbol{r}) = 0$, and the intensity of the incident and the transmitted waves must be equal (conservation of neutron number).

$$u_0^{(1)} + u_0^{(2)} = u_{\text{in}} \qquad (\hat{\boldsymbol{n}} \cdot \boldsymbol{r} = 0) \tag{3.46}$$

$$u_g^{(1)} + u_g^{(2)} = 0 \qquad (\hat{\boldsymbol{n}} \cdot \boldsymbol{r} = 0) \tag{3.47}$$

Before solving Eq. (3.34) under these boundary conditions, the following parameters are introduced to improve the prospects of the discussion.

$$\Delta_0 \equiv \frac{\lambda E\sqrt{|\cos\gamma_0 \cos\gamma_g|}}{\sqrt{|V_g V_{-g}|}} = \frac{v_c k\sqrt{|\cos\gamma_0 \cos\gamma_g|}}{2|F_g|} \tag{3.48}$$

$$y \equiv \frac{\alpha b - (1-b)V_0/E}{2\sqrt{|b|}\sqrt{|V_g V_{-g}|}/E} \tag{3.49}$$

Δ_0 is called the Pendellösung length, and its physical meaning is the spatial period of the Pendellösung fringes intensity distribution that will discuss later. y is a quantity related to the deviation from the Bragg angle, as can be seen from the inclusion of α in its definition formula. Using these parameters to rewrite Eq. (3.39), we get

$$\varepsilon_{1,2} = \frac{\pi\cos\gamma_0}{k\Delta_0}\left(y \pm \sqrt{y^2 + \text{sgn}b}\right)\hat{\boldsymbol{n}} + \frac{V_0}{2E}\hat{\boldsymbol{n}}. \tag{3.50}$$

Substituting for Eq. (3.40) and Eq. (3.41), the wavenumber vectors are expressed as

$$\boldsymbol{K}_0^{(1,2)} = \boldsymbol{k} - \frac{kV_0}{2E\cos\gamma_0}\hat{\boldsymbol{n}} + \frac{\pi}{\Delta_0}\left(-y \mp \sqrt{y^2 + \text{sgn}b}\right)\hat{\boldsymbol{n}}, \tag{3.51}$$

$$\boldsymbol{K}_g^{(1,2)} = \boldsymbol{k} - \frac{kV_0}{2E\cos\gamma_0}\hat{\boldsymbol{n}} + \frac{\pi}{\Delta_0}\left(-y \mp \sqrt{y^2 + \text{sgn}b}\right)\hat{\boldsymbol{n}} + \boldsymbol{g}. \tag{3.52}$$

The first term is the wavenumber vector of the incident wave, and the second term represents the refraction (one-wave approximation) due to the optical potential. The third term represents the separation of the α and β waves due to the periodic potential. $\boldsymbol{g}$ at the end of $K_g^{(1,2)}$ represents the reflection by the reciprocal lattice vector $\boldsymbol{g}$. If the Bragg condition is satisfied exactly in the symmetric Laue configuration ($b = 1,\ y = 0$), then

$$\boldsymbol{K}_0^{(1,2)} = \boldsymbol{k} - \frac{kV_0}{2E\cos\gamma}\hat{\boldsymbol{n}} + \frac{\pi}{\Delta_0}\hat{\boldsymbol{n}}, \tag{3.53}$$

$$\boldsymbol{K}_g^{(1,2)} = \boldsymbol{k} - \frac{kV_0}{2E\cos\gamma}\hat{\boldsymbol{n}} + \frac{\pi}{\Delta_0}\hat{\boldsymbol{n}} + \boldsymbol{g}. \tag{3.54}$$

Eq. (3.34) corresponding to $\varepsilon_{1,2}$ in Eq. (3.50) is as follows

$$\begin{cases} \left[-2\varepsilon_{1,2} + \dfrac{V_0}{E}\right] u_0^{(1,2)} + & \dfrac{V_{-\boldsymbol{g}}}{E} u_{\boldsymbol{g}}^{(1,2)} = 0 \\ \dfrac{V_{\boldsymbol{g}}}{E} u_0^{(1,2)} + & \left[\dfrac{-2\varepsilon_{1,2}}{b} + \alpha + \dfrac{V_0}{E}\right] u_{\boldsymbol{g}}^{(1,2)} = 0 \end{cases} \tag{3.55}$$

Solving this under the boundary condition Eq. (3.47), the amplitude of the 4-component wave fields for the Laue configuration are

$$u_0^{(1,2)} = \frac{u_{\text{in}}}{2}\left(1 \pm \frac{y}{\sqrt{1+y^2}}\right) \tag{3.56}$$

$$u_g^{(1,2)} = \frac{u_{\text{in}}}{2}\sqrt{b}\frac{V_{\boldsymbol{g}}}{\sqrt{|V_{\boldsymbol{g}}V_{-\boldsymbol{g}}|}}\frac{\mp 1}{\sqrt{1+y^2}} \tag{3.57}$$

The incident intensity I_i is

$$I_{\text{i}} = |\psi_{\text{in}}|^2 = u_{\text{in}}^2. \tag{3.58}$$

The intensity of the diffracted wave I_d is

$$I_{\text{d}} = |\psi_0^{(1)} + \psi_0^{(2)} + \psi_g^{(1)} + \psi_g^{(2)}|^2 \tag{3.59}$$

$$= |\psi_0^{(1)} + \psi_0^{(2)}|^2 + |\psi_g^{(1)} + \psi_g^{(2)}|^2 \tag{3.60}$$

$$= I_0 + I_g, \tag{3.61}$$

where the intensity of $(\psi_0^{(1)} + \psi_0^{(2)})^*(\psi_g^{(1)} + \psi_g^{(2)}) + (\psi_0^{(1)} + \psi_0^{(2)})(\psi_g^{(1)} + \psi_g^{(2)})^*$ oscillates rapidly in the space and so much small to be negligible to be smeared by averaging. (We will revisit this point later in Section 6.) Therefore we need only consider the intensity of the transmitted wave $I_0 = |\psi_0^{(1)} + \psi_0^{(2)}|^2$ and the intensity of the reflected wave $I_g = |\psi_g^{(1)} + \psi_g^{(2)}|^2$. The intensity of transmitted and reflected waves is

$$I_0 = u_{\text{in}}^2\left[\cos^2\left(\frac{\pi t}{\Delta_0}\sqrt{y^2+1}\right) + \frac{y^2}{1+y^2}\sin^2\left(\frac{\pi t}{\Delta_0}\sqrt{y^2+1}\right)\right] \tag{3.62}$$

$$I_g = u_{\text{in}}^2\left(\frac{bV_{\boldsymbol{g}}^2}{|V_{\boldsymbol{g}}V_{-\boldsymbol{g}}|}\frac{1}{1+y^2}\right)\sin^2\left(\frac{\pi t}{\Delta_0}\sqrt{y^2+1}\right). \tag{3.63}$$

In the case of the symmetric Laue configuration and $V_{\boldsymbol{g}} = V_{-\boldsymbol{g}}$, Eq. (3.62) does not change and Eq. (3.63) becomes

$$I_g = u_{\text{in}}^2\frac{1}{1+y^2}\sin^2\left(\frac{\pi t}{\Delta_0}\sqrt{y^2+1}\right). \tag{3.64}$$

The average of the intensity of I_0 and I_g in the symmetric Laue configuration are as follow,

$$\bar{I}_0 = u_{\text{in}}^2\frac{1+2y^2}{2(1+y^2)}. \tag{3.65}$$

$$\bar{I}_g = u_{\text{in}}^2\frac{1}{2(1+y^2)}. \tag{3.66}$$

Figure 3.6 illustrates Eq. (3.64) and (3.66). The average reflection intensity $\bar{I}_g$ does not change with thickness, but the oscillation with respect to y becomes finer in proportion to thickness. $y = 1$ is on the order of 1 arcsec angle width. In reality, the divergence angle of a well collimated neutron beam is on the order of

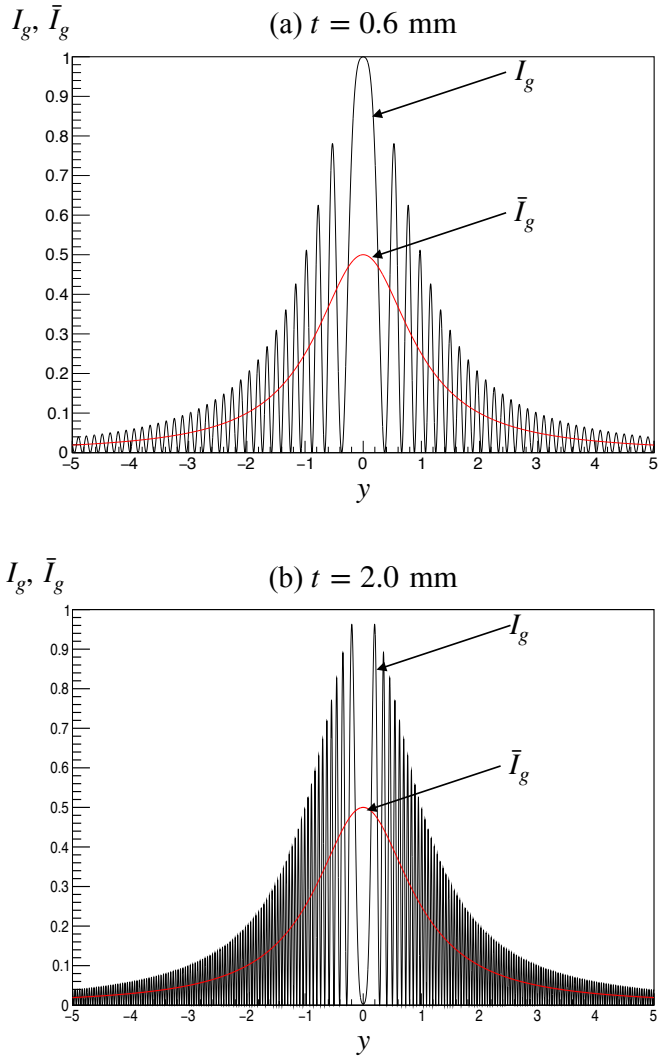

Figure 3.6: Rocking curve.:
The vertical axis is normalized as $u_0^2 = 1$. Thickness of a crystal is (a) $t = 0.6$mm and (b) $t = 2.0$mm, respectively. The average reflection intensity $\bar{I}_g$ does not change with thickness, but the oscillation with respect to y becomes finer in proportion to thickness. $y = 1$ corresponds to the order of 1 arcsec angle width. so what can actually be observed is the average reflection intensity distribution.

10 arcsec, so what can actually be observed is the average reflected intensity distribution. This is called the rocking curve in the symmetric Laue configuration. This full width of half maximum (FWHM) corresponds to $y = \pm 1$. From Eq. (3.49) in the symmetric Laue configuration the relation of y and $\delta\theta = (\theta_B - \theta)$ is

$$y = \frac{\Delta_0}{d_g}\delta\theta, \tag{3.67}$$

so FWHM $= 2d_g/\Delta_0$. As a typical example, in the case of a (110)-plane of SiO with a Bragg angle of 30 degrees, FWHM $\simeq 6.1$ μradian.

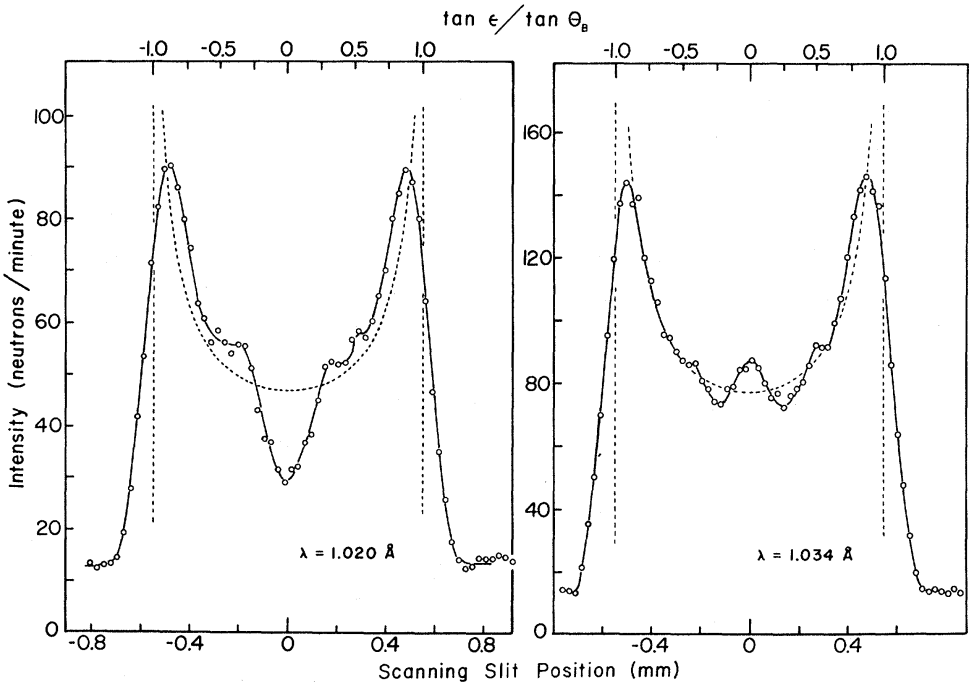

Figure 3.7: The spatial intensity distribution of the crystal injection surface.
In the case of symmetric Laue configuration with silicon (111) crystallographic plane. The left is wave length of $\lambda = 1.020$ Å and the right is wavelength of $\lambda = 1.024$ Å. It can be seen that the intensity of the central area differs from left to right. This is an appearance of the Pendellösung fringes. Quoted from C. G. Shull [51].

3.6 Intensity Distribution of a Plane Slab

In this section, we would discuss how a neutron beam incident on a plane slab crystal generates an intensity distribution on the crystal ejection surface. The interference effects of dynamical diffraction also appear in the spatial intensity distribution of the crystal ejection surface. Figure 3.7 is the result measured by Shull [51].

Considering the case of a plane wave incident on an infinitely wide plane slab crystal, transmitted and reflected waves with a uniform intensity are emitted from the ejection surface. The average intensities depend on only the parameter y as shown in Eq. (3.65) and (3.66), so the intensity profile as like as Fig. 3.7 can not be observed. In reality, the neutron beam has a fairly wide divergence angle relative to the FWHM of the rocking curve, so it is necessary to integrate by the divergence angle. Furthermore, when the incident neutrons are limited by a narrow slit, the Poynting vector of the diffracted neutron wave field, which depends on y, must be considered. Even though it is a narrow slit, its width is on the order of 0.1–1 mm, which is sufficiently wide compared to the neutron wavelength of ~ 1 Å, and the neutron beam can be well approximated by a plane wave.

The solution of the two-wave approximation Eq. (3.42) is divided into α- and β-waves, and the Poynting vector (here called the neutron current) of each would be considered. The neutron current is defined as

$$\boldsymbol{J} \equiv \frac{\hbar}{2\mathrm{i}m}\left(\psi^* \boldsymbol{\nabla}\psi - \psi \boldsymbol{\nabla}\psi *\right) \tag{3.68}$$

Based on this, the neutron currents $\boldsymbol{J}_{1,2}$ for the α and β waves, respectively, are calculated as follows;

$$\boldsymbol{J}_{1,2} = \frac{\hbar k}{m}\left[\left|u_0^{(1,2)}\right|^2 \hat{\boldsymbol{k}}_{\mathrm{B}} + \left|u_g^{(1,2)}\right|^2 \hat{\boldsymbol{k}}_g\right]. \tag{3.69}$$

Here, since the wavenumber vector of diffracted neutrons in the crystal $\boldsymbol{K}_0^{(1,2)}$ and the wavenumber vector of incident neutrons $\boldsymbol{k}$ are almost the same (difference of the order of 10^{-5}), we use the approximation that $\boldsymbol{K}_0^{(1,2)} = \boldsymbol{k}_{\mathrm{B}}$ and $\boldsymbol{K}_g^{(1,2)} = \boldsymbol{k}_{\mathrm{B}} + \boldsymbol{g} = \boldsymbol{k}_g$. Figure 3.8 (a) illustrates schematically the neutron current

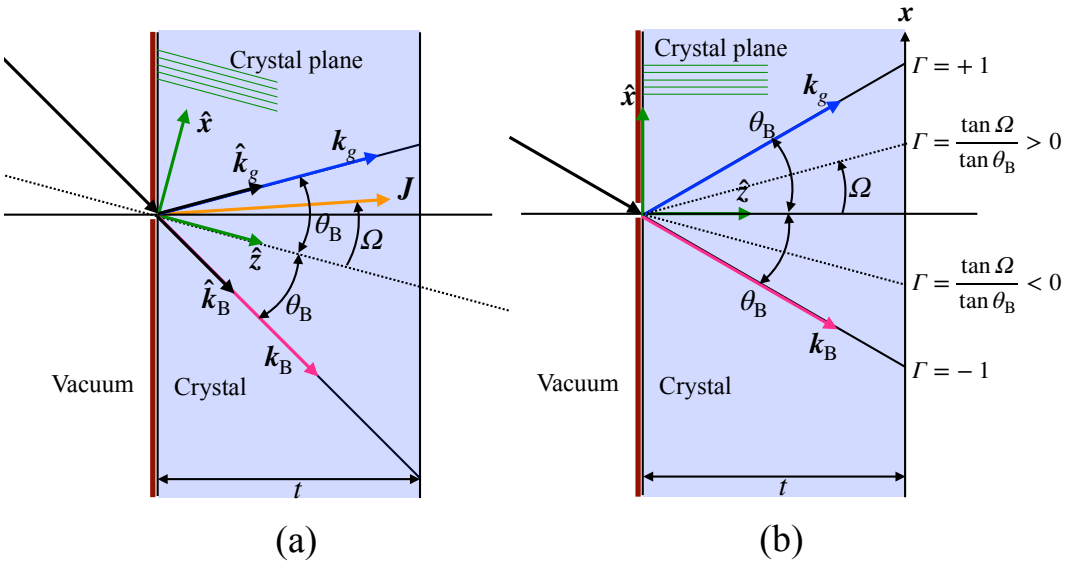

Figure 3.8: Neutron current and the definition of Γ.:
(a) Schematic diagram of the neutron current. Neutrons incident through a narrow slit (shownnby the bold brown line) can be described as neutron current $\boldsymbol{J}$. (b) The definition of Γ is described in the symmetrical Laue configuration.

according to Eq. (3.69). Eq. (3.69) is expressed in diagonal coordinates $(\hat{\boldsymbol{k}}_B, \hat{\boldsymbol{k}}_g)$, so rewriting it in Cartesian coordinates $(\hat{\boldsymbol{x}}, \hat{\boldsymbol{z}})$ with the Borrmann fan centerline as the z-axis yields

$$\boldsymbol{J}_{1,2} = \frac{\hbar k}{m}\left[-\sin\theta_B\left(\left|u_0^{(1,2)}\right|^2 - \left|u_g^{(1,2)}\right|^2\right)\hat{\boldsymbol{x}} + \cos\theta_B\left(\left|u_0^{(1,2)}\right|^2 + \left|u_g^{(1,2)}\right|^2\right)\hat{\boldsymbol{z}}\right]. \tag{3.70}$$

Let Ω be the angle that the neutron current makes with the center of the Borrmann fan. From Eq. (3.70), Ω and θ_B have the following relationship;

$$\tan\Omega_{1,2} = \tan\theta_B \frac{\left|u_0^{(1,2)}\right|^2 - \left|u_g^{(1,2)}\right|^2}{\left|u_0^{(1,2)}\right|^2 + \left|u_g^{(1,2)}\right|^2}. \tag{3.71}$$

Figure 3.9 shows the neutron current for (a) the case where it deviates from the Bragg condition in a smaller direction, (b) the case where the Bragg condition is completely satisfied, and (c) the case where it deviates from the Bragg condition in a larger direction. As shown, when the Bragg condition is fully satisfied ($\delta\theta = 0$), the neutron currents have the same magnitude and travel through the center of the Borrmann fan. When the incident angle is slightly smaller than the Bragg angle ($\delta\theta > 0$), $\boldsymbol{J}_1$ travels in the transmission direction and $\boldsymbol{J}_2$ travels in the reflection direction with a large separation. When the incident angle is slightly larger than the Bragg angle ($\delta\theta < 0$), $\boldsymbol{J}_2$ travels in the transmission direction and $\boldsymbol{J}_1$ travels in the reflection direction with a large separation.

Here the normalized coordinate Γ would be introduced instead of x, as shown in Fig. 3.8 (b).

$$\Gamma \equiv \frac{\tan\Omega}{\tan\theta_B}, \tag{3.72}$$

By the definition, $\Gamma_{1,2}$ are represent the ejection points of $\boldsymbol{J}_{1,2}$ as follows,

$$\Gamma_{1,2} = \frac{\tan\Omega_{1,2}}{\tan\theta_B}. \tag{3.73}$$

And, from Eq. (3.70)

$$\Gamma_{1,2} = -\frac{1 - \left|u_g^{(1,2)}\right|^2 / \left|u_0^{(1,2)}\right|^2}{1 + \left|u_g^{(1,2}\right|^2 / \left|u_0^{(1,2)}\right|^2}. \tag{3.74}$$

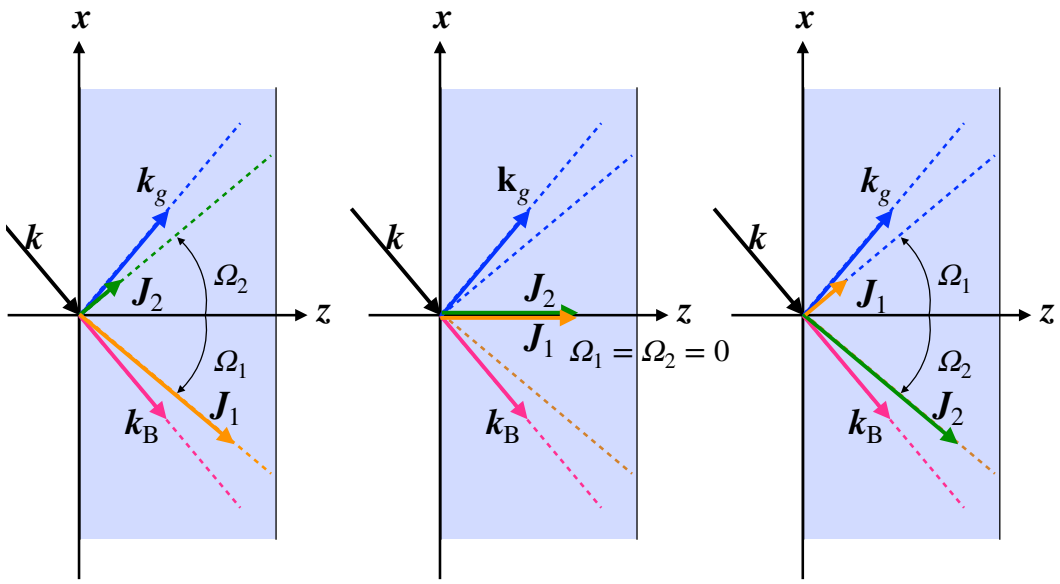

Figure 3.9: Schematic diagrams of the neutron currents in the 3 cases of the 3 different $\delta\theta$ in the symmetric Laue configuration of α-quartz:
(a) When the incident angle is slightly smaller than the Bragg angle, $\boldsymbol{J}_1$ travels in the transmission direction and $\boldsymbol{J}_2$ travels in the reflection direction with a large separation. (b) When the Bragg condition is fully satisfied, the neutron currents of $\boldsymbol{J}_1$ and $\boldsymbol{J}_2$ have the same magnitude and travel through the center of the Borrmann fan. (c) When the incident angle is slightly larger than the Bragg angle, $\boldsymbol{J}_2$ travels in the transmission direction and $\boldsymbol{J}_1$ travels in the reflection direction with a large separation.

Furthermore, from Eq. (3.56), (3.57) and Eq. (3.49), $\Gamma_{1,2}$ are represented as the function of y as follows.

$$\Gamma_{1,2} = -\frac{1-|b|y \mp \sqrt{y^2+\mathrm{sgn}b}}{1+|b|y \mp \sqrt{y^2+\mathrm{sgn}b}}. \tag{3.75}$$

In the case of symmetrical Laue configuration,

$$\Gamma_{1,2} = \mp\frac{y}{\sqrt{y^2+1}}. \tag{3.76}$$

Since the factor, Δ_0/d_g connecting y and the deviation $\delta\theta$ as shown in Eq. (3.67) is on the order of 10^5, even a small deviation will result in a large value of y and nearly $\Gamma = 1$. For example, in the case of (110)-plane of a α-quartz, Δ_0/d_g is $\simeq 3\times10^5$ and when $\delta\theta = 10$ μradian, $y \simeq 3.25$ and $\Gamma \simeq 0.956$. So the direction of neutron current will rapidly converge in the transmission and reflection directions ($\Gamma \to \mp 1$). This is the reason for the sharp peaks on both sides of $\Gamma = \mp 1$ in Fig. 3.7.

As mentioned above, a monochromatic plane wave cannot explain the intensity distribution as shown in Fig. 3.7. Since the actual neutron beam has a finite divergence angle and a finite wavelength dispersion, wave fields with different values of y would be excited in the crystal, and the actual intensity distribution is obtained by adding them together [50].

$$\Psi(\boldsymbol{r}) = \int_{-\infty}^{+\infty} dy\psi(\boldsymbol{r},y). \tag{3.77}$$

The intensity amplitude $I(\Gamma)dy$ of the crystal's injection plane is given by considering that the wave fields α and β are in the same neutron-current direction. That is, $\boldsymbol{J}_1(-y)$ and $\boldsymbol{J}_2(y)$ are superimposed at the position

Γ of the injection plane, as can be seen from Eq. (3.76). The following equation is obtained by variable transformation from y to Γ.

$$I_{0,g}(\Gamma)d\Gamma = \int_{-\infty}^{+\infty} \left| \psi_{0,g}^{(1)}(-y) + \psi_{0,g}^{(2)}(+y) \right|^2 |dy/d\Gamma| \, d\Gamma. \tag{3.78}$$

The stationary phase method can be used to find the the intensity amplitude can be written as

$$I_0(\Gamma) = 2u_{\mathrm{in}}^2 \Delta_0 \tan\theta_{\mathrm{B}} \left[\frac{1-\Gamma}{(1+\Gamma)\sqrt{1-\Gamma^2}} \right] \cos^2\left(\frac{\pi t}{\Delta_0}\sqrt{1-\Gamma^2} + \frac{\pi}{4} \right) d\Gamma, \tag{3.79}$$

$$I_g(\Gamma) = 2u_{\mathrm{in}}^2 \Delta_0 \tan\theta_{\mathrm{B}} \left[\frac{1}{\sqrt{1-\Gamma^2}} \right] \sin^2\left(\frac{\pi t}{\Delta_0}\sqrt{1-\Gamma^2} + \frac{\pi}{4} \right) d\Gamma. \tag{3.80}$$

And the relative intensity distribution can be written as

$$P_0(\Gamma) = \left[\frac{1-\Gamma}{(1+\Gamma)\sqrt{1-\Gamma^2}} \right] \cos^2\left(\frac{\pi t}{\Delta_0}\sqrt{1-\Gamma^2} + \frac{\pi}{4} \right) d\Gamma, \tag{3.81}$$

$$P_g(\Gamma) = \left[\frac{1}{\sqrt{1-\Gamma^2}} \right] \sin^2\left(\frac{\pi t}{\Delta_0}\sqrt{1-\Gamma^2} + \frac{\pi}{4} \right) d\Gamma. \tag{3.82}$$

The averaged relative intensity distributions become

$$\bar{P}_0(\Gamma) = \frac{1-\Gamma}{2(1+\Gamma)\sqrt{1-\Gamma^2}} d\Gamma. \tag{3.83}$$

$$\bar{P}_g(\Gamma) = \frac{1}{2\sqrt{1-\Gamma^2}} d\Gamma. \tag{3.84}$$

Figure 3.10 shows the calculation results of $P_{0,g}(\Gamma)$ and $\bar{P}_{0,g}(\Gamma)$ with the (110)-plane of α-quartz, the value of Γ is set from -0.999 to 0.999, because the intensity is infinite at $\Gamma = \pm 1$. In reality, as Fig. 3.7 shows, it does not go to infinity, and the range of Γ also slightly exceeds ± 1. The reason why the range exceeds ± 1 is because the slit width and divergence angle are finite. When the entrance slit is 0.6 mm, with the thickness of 10 mm, and the divergence angle is 1 mradian, the calculation result of $P_g(\Gamma)$ of (110)-plane of α-quartz becomes Fig. 3.11. However, again, the integral range of gamma is restricted to the range of -0.999 to +0.999.

Theories that avoid infinity magnitude at $\Gamma = \pm 1$ and treat diffraction intensity distributions in realistic crystals including mosicity and defects include the spherical wave theory and the statistical dynamical diffraction theory. In this paper, however, we attempt to explain realistic intensity distributions with plane wave theory. The reason why the intensity goes to infinity at $\Gamma = \pm 1$ can be attributed to the fact that the integral with respect to y is integrated with the same weight from $-\infty$ to $+\infty$ in Eq. (3.77). In real, as shown in Fig. 3.6, the reflective intensity is decrease as $|y|$ increase. Appropriate weighting is considered necessary.

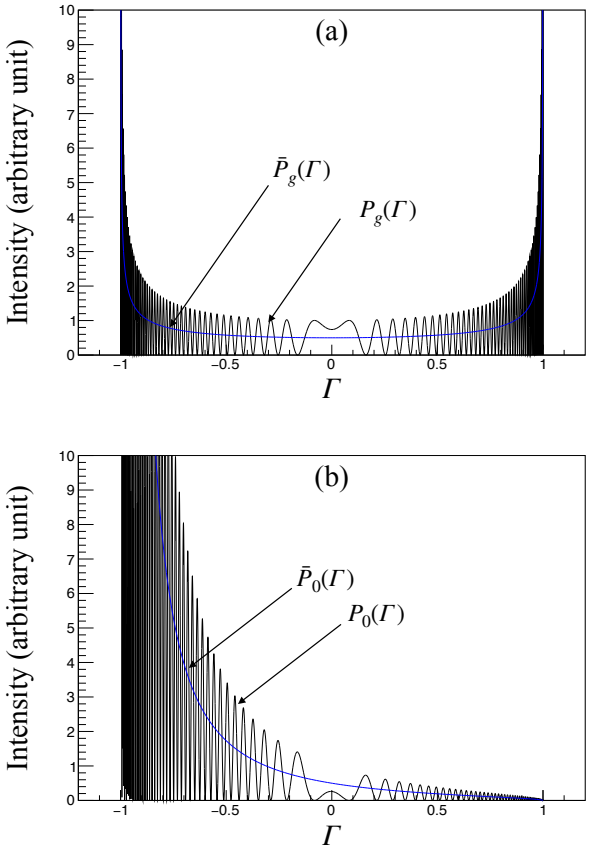

Figure 3.10: Diffraction intensity distribution of the (110)-plane of α-quartz:
Calculation was performed within $\Gamma = -0.999$ and $\Gamma = 0.999$ in the ideal case with the width of slits of 0 and beam divergence angle of 0

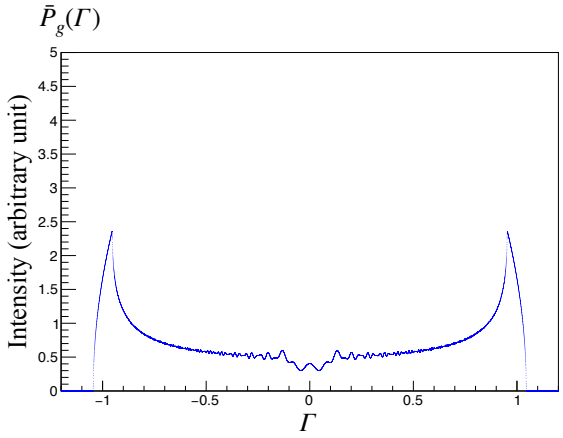

Figure 3.11: Diffraction intensity distribution of the (110)-plane of α-quartz in more realistic case:
Calculation was performed within $\Gamma = -0.999$ and $\Gamma = 0.999$ in the realistic case when the entrance slit is 0.6 mm with the thickness of 10 mm, and the divergence angle is 1 mradian.

4 Principles of nEDM Measurement by the Crystal Diffraction Method

In this section, the measurement principle of the nEDM search experiment using crystal diffraction, quantitative calculations of its effects and false signal is described. It also touches on non-centrosymmetric crystal candidates that are expected to have strong intra-crystal electric fields.

4.1 Principles of nEDM Measurement by the Crystal Diffraction Method

As described in Section 2, the measurement principle of the nEDM search experiment uses the precession of the spin magnetic moment and the nEDM in an electromagnetic field. In this section, we give a quantitative explanation of the measurement principle of the crystal diffraction method in the case of the symmetric Laue configuration.

When neutrons satisfying the Bragg condition are incident on a crystal in the symmetric Laue configuration, the wave field in the crystal can be expressed as a superposition of four waves as shown in Eq. (3.42. In the symmetric Laue configuration, the amplitudes of 4 waves are as follows from Eq. (3.56)and Eq. (3.57);

$$u_0^{(1)} = u_0^{(2)} = u_g^{(2)} = \frac{1}{2}, \;\; u_g^{(1)} = -\frac{1}{2}. \tag{4.1}$$

$$\begin{aligned}\psi_{\mathrm{cry}}(\boldsymbol{r}) = \frac{1}{2}\exp\left(\mathrm{i}\boldsymbol{K}_0^{(1)}\cdot\boldsymbol{r}\right) - \frac{1}{2}\exp\left(\mathrm{i}\boldsymbol{K}_g^{(1)}\cdot\boldsymbol{r}\right) \\ + \frac{1}{2}\exp\left(\mathrm{i}\boldsymbol{K}_0^{(2)}\cdot\boldsymbol{r}\right) + \frac{1}{2}\exp\left(\mathrm{i}\boldsymbol{K}_g^{(2)}\cdot\boldsymbol{r}\right)\end{aligned} \tag{4.2}$$

The intensity distribution of transmitted and reflected waves was explained in Section 3. Here we will take a different view and divide the wave field into two waves, α- and β-waves.

$$\psi^{\alpha} = \psi_0^{(1)} + \psi_g^{(1)}, \tag{4.3}$$

$$\psi^{\beta} = \psi_0^{(2)} + \psi_g^{(2)}. \tag{4.4}$$

The intensity distribution of α- and β-waves is calculated as follows.

$$|\psi^{\alpha}|^2 = \sin^2\left(\frac{\boldsymbol{g}}{2}\cdot\boldsymbol{r}\right), \tag{4.5}$$

$$|\psi^{\beta}|^2 = \cos^2\left(\frac{\boldsymbol{g}}{2}\cdot\boldsymbol{r}\right). \tag{4.6}$$

This is shown schematically in Fig. 4.1. It can be seen that α-wave has a sin-wave intensity distribution with respect to the crystal lattice period, while β-wave has a cos-wave intensity distribution. In other words, α-wave propagates in the crystal as a standing wave with its maximum on the middle of the crystal lattice plane, and β-wave propagates as a standing wave with its maximum on the crystal lattice plane. Since the neutron, a Fermi particle, is a single-particle wave function, a single neutron is a superposition of these α- and β-waves. The electromagnetic interaction of a neutron such a different intensity distribution in the crystal is important of the nEDM search by crystal diffraction method in the Laue configuration. It is important to note that it is the nuclear potential, which has an overwhelming magnitude as mentioned in section 3.1, that determines the intensity distribution of such neutrons. Therefore, the intensity distribution of neutrons has the same period and phase as the crystal lattice.

All materials contain nuclei and electrons of the same charge. The electric field in a material is determined by the distribution of these nuclei and electrons exists in the material. The positive charge of nuclei and the negative charge of electrons cancel each other as a whole, but it is considered to be very strong when

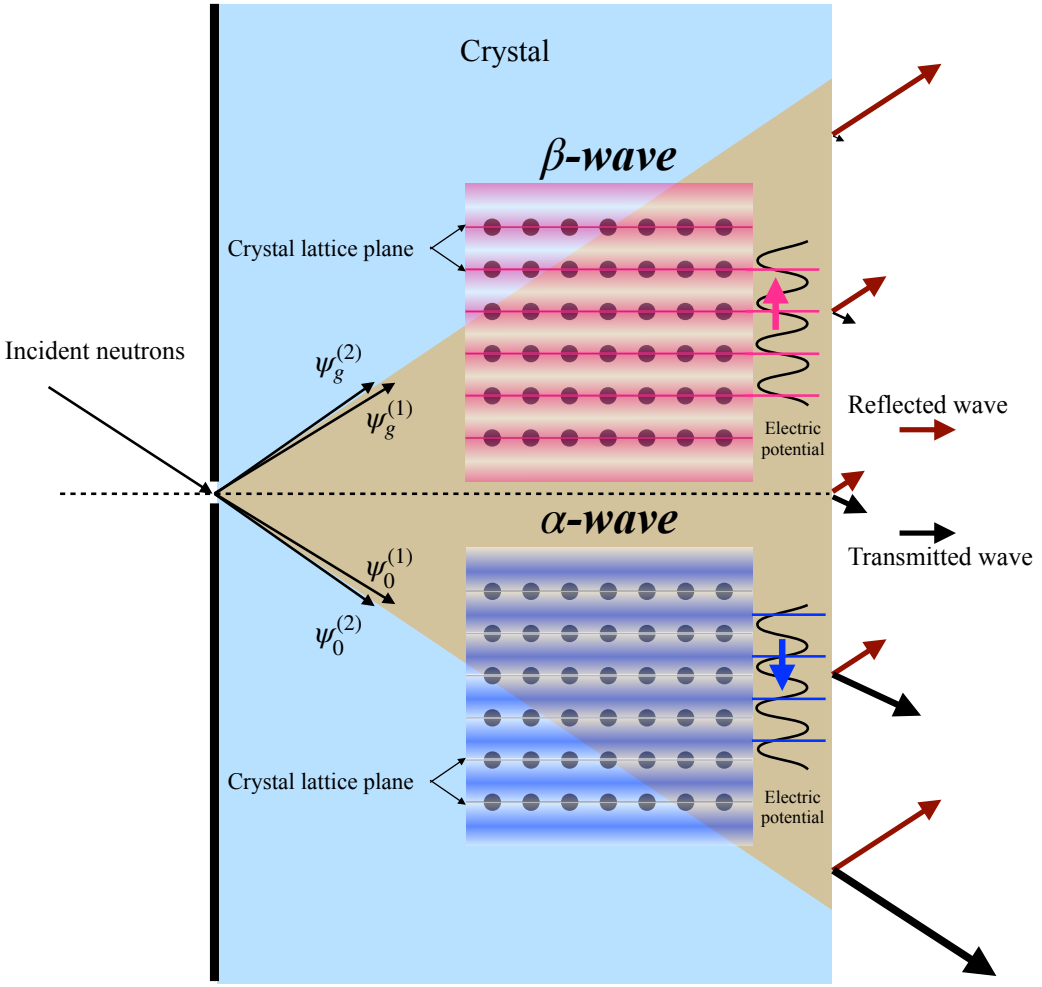

Figure 4.1: α-and β-waves in a crystal in the symmetric Laue configuration:
The waves $\psi_0^{(1)}$ and $\psi_g^{(1)}$ form an α-wave, which is a standing wave with a maximum (shown in dark blue) in the center of the lattice plane; The waves $\psi_0^{(2)}$ and $\psi_g^{(2)}$ form a β-wave, which is a standing wave with a maximum (shown in dark red) on the lattice plane. While the neutron intensity distribution is in phase with the lattice plane, the phase of the electric potential is shifted from the lattice plane at a certain $\boldsymbol{g}$-plane of the non-centrosymmetric crystal, as shown on the right side of the figure. In this case, because the neutron intensity distribution and the phase of the electric potential are out of phase, the α-and β-waves experience electric fields in opposite directions, as indicated by the arrows in the figure

viewed at the atomic level. The electric potential $U^{\mathrm{E}}(\boldsymbol{r})$ due to the charge distribution in a crystal can be Fourier-expanded in terms of $\boldsymbol{g}$,

$$U^{\mathrm{E}}(\boldsymbol{r}) = \sum_{\boldsymbol{g}} U_g^{\mathrm{E}} \exp(\mathrm{i}\boldsymbol{g}\cdot\boldsymbol{r}) \tag{4.7}$$

In the two-wave approximation, only U_0^{E} and U_g^{E} with $\boldsymbol{g}$ satisfying the Bragg condition are meaningful. Because neutron wave has meaningful strength only ψ_0 and ψ_g against to $\mathbf{0}$ and $\boldsymbol{g}$, respectively, as shown Eq. (3.42). Since $U_0^{\mathrm{E}} = 0$ as averaged electric potential, we need only consider U_g^{E}. In many crystals, U_g^{E} has the same period and phase as the crystal lattice, i.e. as same as the α- and β-waves, so the electric field integrated over the intensity distribution of α- and β-waves is zero. However, in some types of non-centrosymmetric crystals, the phase of U_g^{E} is out of phase with the crystal lattice for a particular crystal plane $\boldsymbol{g}$. In this case, the intensity distribution of neutrons and the phase of the electric potential U_g^{E} are out of phase, and so the neutrons feel the effective electric field $\boldsymbol{E}_g^{\mathrm{eff}}$ as a result of integration over the unit cell. As shown schematically in Fig. 4.1, the intra-crystal electric field felt by the α- and β-wave components is in opposite directions because the α- and β-wave has intensity distribution of sine-wave and cosine-wave, respectively. If neutrons have the nEDM, an interaction potential with the effective intra-crystal electric field

is generated;

$$V^{\mathrm{E}} = -d_n \boldsymbol{\sigma} \cdot \boldsymbol{E}_g^{\mathrm{eff}}. \tag{4.8}$$

A neutron moving in an electric field senses the following relativistic magnetic field.

$$\boldsymbol{B}_{\mathrm{S}} = \frac{[\boldsymbol{E}_g^{\mathrm{eff}} \times \boldsymbol{v}]}{c^2}, \tag{4.9}$$

where $\boldsymbol{v}$ is the velocity of the neutron relative to the electric field and c is the speed of light. Hereafter in this paper, this relativistic magnetic field will be referred to as the Schwinger magnetic field. Since neutrons have a spin magnetic moment, an interaction potential with the Schwinger magnetic field is generated;

$$V^{\mathrm{S}} = -\mu_n \boldsymbol{\sigma} \cdot \boldsymbol{B}_{\mathrm{S}}. \tag{4.10}$$

Therefore, neutrons diffracted dynamically in a crystal will interact with the effective intra-crystal electric field and the Schwinger magnetic field. The principle of the crystal diffraction method for nEDM search is to study neutron spin by using these electromagnetic field.

4.2 Calculation of the nEDM Effect

The nEDM effect of crystal diffraction in the Laue configuration, which is the amount of spin rotation due to the precession of a finite nEDM, is given by

$$\varphi^{\mathrm{EDM}} = \frac{4 d_n E_g^{\mathrm{eff}} \tau}{\pi \hbar} \tag{4.11}$$

In this section, we would derive it. Figure 4.2 schematically illustrates the precession of neutron spins due to the interaction of nMDM and nEDM with the Schwinger magnetic field and the effective intra-crystal electric field, respectively. Note here that the interaction potential V^{S} of the Schwinger magnetic field is much larger than the interaction potential V^{E} of the effective intra-crystal electric field. For example, for (110)-plane of α-quartz at the Bragg angle of 87 degrees, V^{S} is 10^5 orders of magnitude larger than V^{E} of the current nEDM upper limit, so the precession of nEDM is 10^{-5} orders of magnitude smaller than that of nMDM.

A neutron incident on the crystal is composed of two components, α- and β-waves, due to the dynamical diffraction. When the effective intra-crystal electric field exists at the crystal plane $\boldsymbol{g}$, the neutron senses it and the resulting Schwinger magnetic field. In the Fig. 4.2, it is assumed that there is the effective intra-crystal electric field in the $\boldsymbol{x}$ direction for the α-wave, which generates the Schwinger magnetic field in the $\boldsymbol{z}$ direction. In contrast, the β-wave is subjected to the effective intra-crystal electric field in the opposite $-\boldsymbol{x}$ direction, which also generates the Schwinger magnetic field in the $-\boldsymbol{z}$ direction. As a result, the α- and β-waves have opposite spin precessions. α-wave is rotating clockwise and β-wave is rotating counterclockwise around the $\boldsymbol{z}$-axis due to the Schwinger magnetic field. The presence of the nEDM causes a slight precession around the effective intra-crystal electric field as well, with the α-wave rotating clockwise and the β-wave rotating counterclockwise around the $\boldsymbol{x}$-axis. This results in spin polarization in the $\boldsymbol{y}$-axis direction, which can be measured to search for nEDM. The amount of spin rotation by the nEDM when the spin polarization in the $\boldsymbol{x}$-axis is zero as a result of $\pi/2$ rotation by the Schwinger magnetic field is given by Eq. (4.11). The measurement need be made when the spin polarization in the $\boldsymbol{x}$-axis is zero as discussed in the next section.

The precession angular frequency ω_{S} according to the Schwinger magnetic field is

$$\omega_{\mathrm{S}} = \frac{2\mu_n B_{\mathrm{S}}}{\hbar}, \tag{4.12}$$

and the precession angular frequency ω_{E} by the effective intra-crystal electric field is

$$\omega_{\mathrm{E}} = \frac{2 d_n E_g^{\mathrm{eff}}}{\hbar}. \tag{4.13}$$

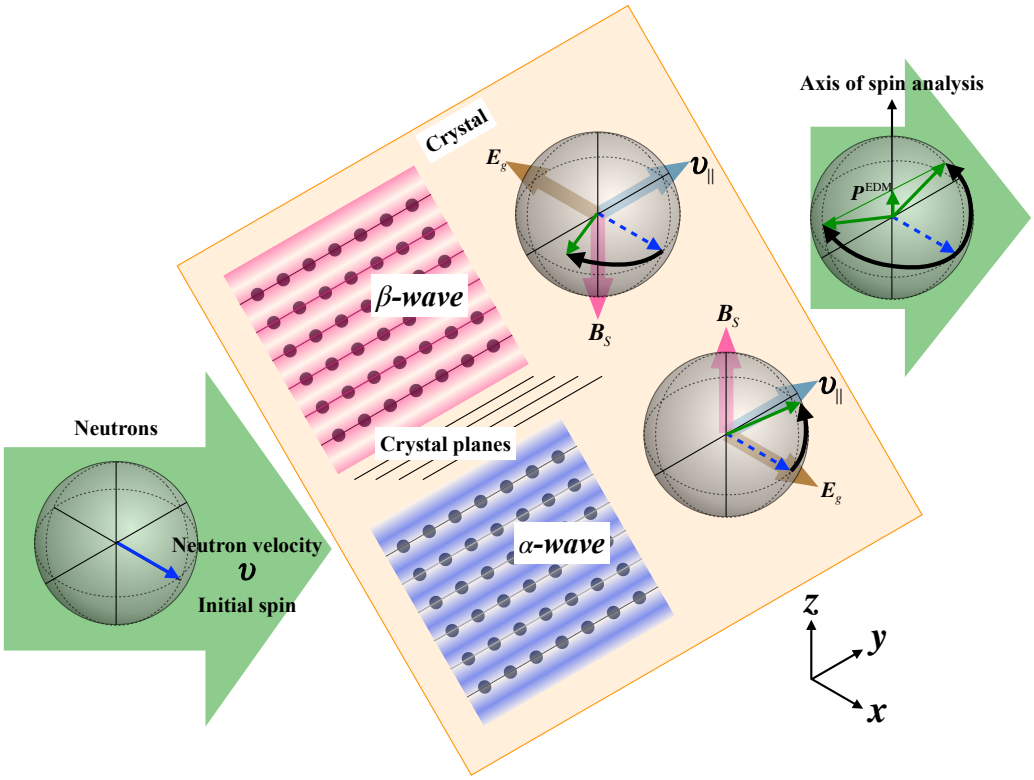

Figure 4.2: Precession of nMDM and nEDM:
Neutrons enter the crystal from left side with the spin parallel to the velocity of the neutron. Neutrons in the crystal consist of α- and β-waves. When α-wave senses the effective intra-crystal electric field in the $\boldsymbol{x}$ direction, the Schwinger magnetic field $\boldsymbol{B}_{\mathrm{S}}$ is generated in the $\boldsymbol{z}$ direction and causes precession in the clockwise direction of $\boldsymbol{z}$. On the other hand, β wave senses the effective intra-crystal electric field in the $-\boldsymbol{x}$ direction, the Schwinger magnetic field is generated in the $-\boldsymbol{z}$ direction and causes precession in the counterclockwise direction of $\boldsymbol{z}$. At the same time, since the precession of nEDM due to the effective intra-crystal electric field occurs clockwise and counterclockwise around the $\boldsymbol{x}$ axis, respectively, the polarization of $\boldsymbol{z}$ is observed as the effect of nEDM when the polarization of $\boldsymbol{x}$ is zero.

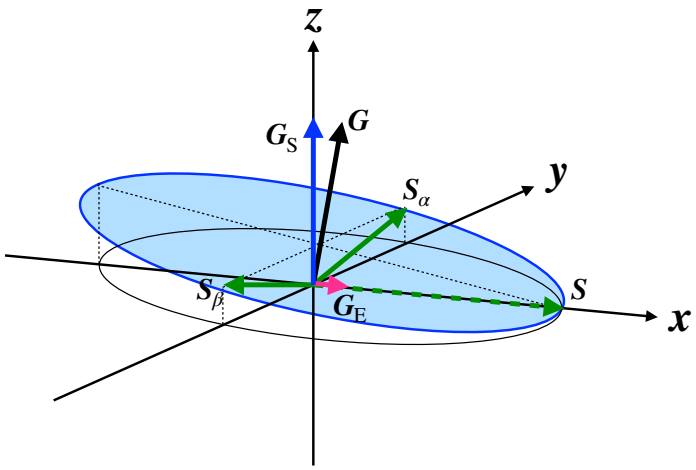

Figure 4.3: Rotation vector and Spin rotation:
$\boldsymbol{G}_{\mathrm{S}}$ and $\boldsymbol{G}_{\mathrm{E}}$ is the rotation vector due to the Schwinger magnetic field and the intra-crystal electric field, respectively, and $\boldsymbol{G}$ is the composite rotation vector of those. $\boldsymbol{S}$ is the initial spin state and $\boldsymbol{S}_\alpha$ and $\boldsymbol{S}_\beta$ is the spin state of α- and β-wave, respectively after the precession of $\pi/2$ due to the Schwinger magnetic field. The spin precess on the plane colored by blue.

Since both precessions occur simultaneously, the actual precession is the composite of the rotation vectors due to the Schwinger magnetic field and the effective intra-crystal electric field. This rotation vector $\boldsymbol{G}$ becomes as follows and is shown in Fig. 4.3.

$$\boldsymbol{G} = \frac{2\mu_n B_{\mathrm{S}}}{\hbar}\hat{\boldsymbol{z}} + \frac{2d_n E_g^{\mathrm{eff}}}{\hbar}\hat{\boldsymbol{x}} \tag{4.14}$$

The components of the unit vector of $\boldsymbol{G}$ are denote (n_x, n_y, n_z) and the rotation operator around this axis is as follows.

$$n_x = \frac{\omega_{\mathrm{E}}}{\sqrt{\omega_{\mathrm{E}}^2 + \omega_{\mathrm{S}}^2}}, n_y = 0, n_z = \frac{\omega_{\mathrm{S}}}{\sqrt{\omega_{\mathrm{E}}^2 + \omega_{\mathrm{S}}^2}} \tag{4.15}$$

$$\mathscr{R}(\Theta : \hat{\boldsymbol{G}}) = \begin{pmatrix} \cos\frac{\Theta}{2} - \mathrm{i}n_z \sin\frac{\Theta}{2} & \mathrm{i}n_x \sin\frac{\Theta}{2} \\ -\mathrm{i}n_x \sin\frac{\Theta}{2} & \cos\frac{\Theta}{2} + \mathrm{i}n_z \sin\frac{\Theta}{2} \end{pmatrix} \tag{4.16}$$

Since the rotation due to the effective intra-crystal electric field is very small compared to the rotation due to the Schwinger magnetic field, the amount of rotation angle Θ can be considered as the rotation angle due to only the Schwinger magnetic field. The wave function of the incident neutron is

$$\psi_{in} = \frac{1}{2}[|z;+\rangle + |z;-\rangle]\psi^{\alpha} + \frac{1}{2}[|z;+\rangle + |z;-\rangle]\psi^{\beta} \tag{4.17}$$

The wave function after rotation is

$$\begin{aligned}
\psi_{rot} &= \mathscr{R}(\Theta : \hat{\boldsymbol{G}})\left\{\frac{1}{2}[|z;+\rangle + |z;-\rangle]\psi^{\alpha}\right\} + \mathscr{R}(-\Theta : \hat{\boldsymbol{G}})\left\{\frac{1}{2}[|z;+\rangle + |z;-\rangle]\psi^{\beta}\right\} \\
&= \frac{1}{2}\psi^{\alpha}\left\{\left[\cos\left(\frac{\Theta}{2}\right) - \mathrm{i}(n_z + n_x)\sin\left(\frac{\Theta}{2}\right)\right]|z;+\rangle + \left[\cos\left(\frac{\Theta}{2}\right) + \mathrm{i}(n_z - n_x)\sin\left(\frac{\Theta}{2}\right)\right]|z;-\rangle\right\} \\
&\quad + \frac{1}{2}\psi^{\beta}\left\{\left[\cos\left(\frac{\Theta}{2}\right) + \mathrm{i}(n_z + n_x)\sin\left(\frac{\Theta}{2}\right)\right]|z;+\rangle + \left[\cos\left(\frac{\Theta}{2}\right) - \mathrm{i}(n_z - n_x)\sin\left(\frac{\Theta}{2}\right)\right]|z;-\rangle\right\}
\end{aligned} \tag{4.18}$$

Note that the rotation angles of the α- and β-waves are reversed in the $\pm$ direction. Spin analysis in the z-axis gives the polarization P in the z-axis direction as

$$P = 2n_x n_z \sin^2\left(\frac{\Theta}{2}\right). \tag{4.19}$$

The relation between the polarization and the spin rotation is

$$P = \sin\varphi^{\mathrm{EDM}} \simeq \varphi^{\mathrm{EDM}}, \tag{4.20}$$

where φ^{EDM} is so small. Therefore the spin rotation is

$$\begin{aligned}
\varphi^{\mathrm{EDM}} &= 2n_x n_z \sin^2\left(\frac{\Theta}{2}\right) \\
&= \frac{2d_n E_g}{\mu_n B_{\mathrm{S}}}\sin^2\left(\frac{\Theta}{2}\right).
\end{aligned} \tag{4.21}$$

When the rotation angle of Θ due to the Schwinger magnetic field is $\pi/2$,

$$\frac{2\mu_n B_{\mathrm{S}}}{\hbar}\tau = \frac{\pi}{2}. \tag{4.22}$$

Substituting this relation into Eq. (4.21), we obtain Eq. (4.11).

The nEDM signal varies periodically with the $\sin^2$-function for the rotation around the Schwinger field, and reaches its maximum of 2 times of Eq. (4.11) at $(2n+1)\pi$ rotation. However, as described in next section, the measurement is performed at $(2n+1)/2\pi$ rotation, when the spin polarization is $P = 0$ in the x-axis direction, to minimize the false signal due to the tilt of the spin analysis axis.

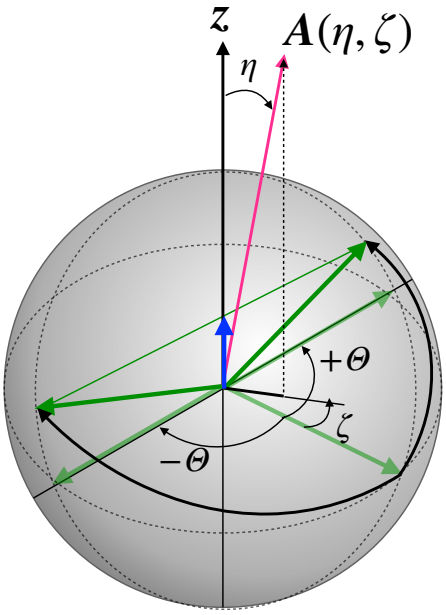

Figure 4.4: Tilt of spin analysis axis and false signal of EDM effect:
The case where the spin analysis axis $\boldsymbol{A}$ is tilted by an angle (η, ζ) with respect to the spin rotation axis $\boldsymbol{z}$ is shown.

4.3 False Signal of EDM Effect

In the nEDM search experiment using crystal diffraction in the Laue configuration, small polarization effects perpendicular to the spin quantization axis of the incident neutrons are measured. In the following discussion, the z-axis is regarded as the axis of spin rotation because the actual spin rotation axis $\boldsymbol{G}$ and the z-axis in Fig. 4.3 are considered almost identical.

As shown in Fig. 4.4, when the initial spin quantization axis is the x-axis and the precession axis is the z-axis, the precession due to the Schwinger magnetic field takes place in the xy-plane and the polarization, which is the EDM effect, occurs in the z-axis direction. If the spin analysis axis is aligned exactly with the z-axis, no false signal appears, but if it is tilted from the z-axis, a false signal appears. If the spin analysis axis $\boldsymbol{A}$ is tilted by an angle (η, ζ) with respect to the z-axis, the polarization in the z-axis direction can be calculated as follows by performing the same calculation as in Section 4.2.

$$P = 2n_z n_x \cos\eta \sin^2\left(\frac{\Theta}{2}\right) + \sin\eta\cos\zeta\left[1 - 2n_z^2 \sin^2\left(\frac{\Theta}{2}\right)\right]. \tag{4.23}$$

The first term is the EDM effect, and the second term is the false signal caused by the tilt of the spin analysis axis.

Figure 4.5 (a) and (b) show the relationship between the rotation angle Θ (around $\pi/2$ radians) due to the Schwinger magnetic field and the tilt angle $(\eta, \zeta = 0)$ of the spin analysis axis for the ratio of the EDM effect to the false signal (S/N ratio) of 10 and 1, respectively. When $\Theta = \pi/2$ radians, the false signal is theoretically zero regardless of the magnitude of η. However, $\eta = 0$ is preferred because the EDM effect is proportional to $\cos\eta$. As Θ deviates from $\pi/2$ radians, η drops sharply. To make η loose, Θ must be exact, and to make Θ loose, η must be close to zero. For example, for $S/N > 10$, if Θ is $\pi/2 \pm 0.01$ radians, η must be within ± 0.000035 radians; even for $S/N = 1$, η must be within ± 0.00035 radians. In actual experiments, it is difficult to achieve such precision. Possible solutions include scanning the tilt angle η or the polarization P_x in the appropriate range with the center of $P_x = 0$ and estimating the minimum value by fitting, or performing a symmetric experiment in which the crystal is inverted exactly 180 degrees without changing the experimental system to cancel out the false signal.

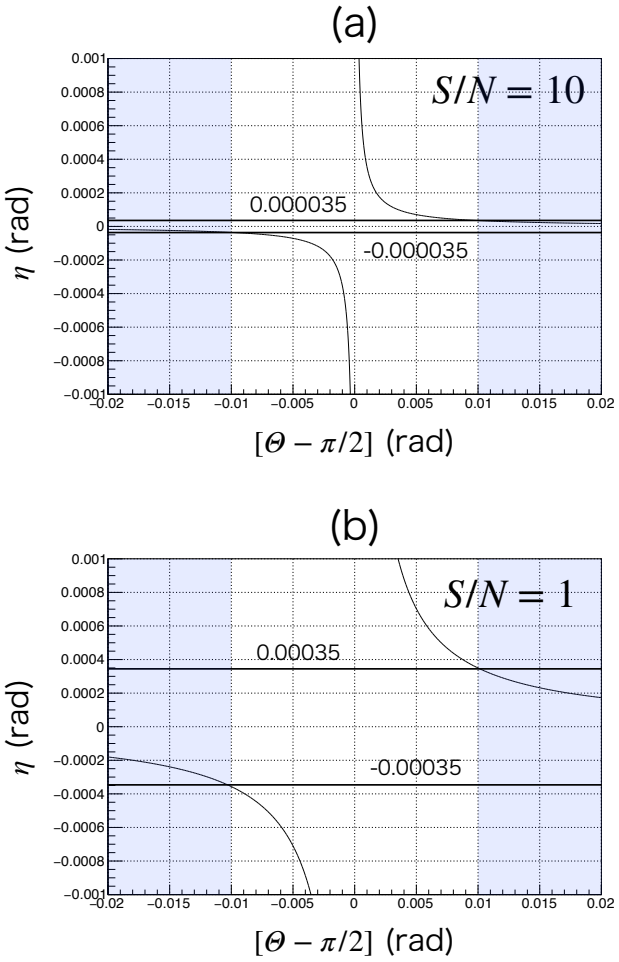

Figure 4.5: Tilt of spin analysis axis and false signal of EDM effect:
When the spin analysis axis is tilted by angle $(\eta, \zeta = 0)$, the relationship between the spin rotation angle Θ due to the Schwinger magnetic field and η is shown in the vicinity of $\Theta = \pi/2$ radians. (a) is when the ratio of the EDM effect to the false signal (S/N) is 10 and (b) is when it is 1. For $S/N = 10$, considering the control of the spin rotation angle to be about 0.01 radians, the tilt of the spin analysis axis must be less than ± 0.000035 radians; even for $S/N = 1$, it must be less than ± 0.00035 radians.

4.4 Candidates of Non-Centrosymmetric Crystal

The crystal diffraction method uses non-centrosymmetric crystals in which an effective intra-crystal electric field exists. A list of typical non-centrosymmetric crystal candidates is given in Table 4.1. The requirements for use in crystal diffraction method are as follows.

(1) The crystal must be a non-centrosymmetric crystal.
(2) Stable, high-quality crystals of sufficient size can be obtained.
(3) Strong effective intra-crystal electric field.
(4) Low neutron absorption coefficient.

In the case of the symmetric Laue configuration, the spin rotation angle due to the Schwinger field should be $\pi/2$ to suppress the false signal described in Section 4.3. Therefore, from Eq. (4.22), the required crystal thickness is

$$L = \frac{\pi \hbar c^2}{4 \mu_n E_g^{\mathrm{eff}}} \tag{4.24}$$

Table 4.1: Candidates of non-symmetric crystal for the diffraction method:
d_{hkl}:Distance between lattice planes. $E_g^{\rm eff}$:The effective intra-crystal electric field. L:Thickness of crystal required to $\pi/2$ spin rotation due to the Schwinger magnetic field. τ: Passing time through the crystal when the Bragg angle is 87 degrees.
$E_g^{\rm eff}\tau$ is proportional to the magnitude of the EDM effect.

Crystal	Symmetry Groupe	Crystal-plane	d_{hkl}	$E_g^{\rm eff}$	L	τ	$E_g^{\rm eff}\tau$
		(unit)	Å	10^8 V/cm	mm	msec	kVs/cm
SiO_2	32(D63)	111	2.24	2.30	33.6	1.45	333
(α-quartz)		110	2.46	2.00	38.6	1.83	366
$Bi_{12}GeO_{20}$	123	433	1.74	5.20	14.8	0.50	259
		312	2.71	2.40	32.2	1.68	403
$Bi_4Si_3O_{12}$	-43m	242	2.10	4.60	16.8	0.68	312
		132	2.75	3.20	24.1	1.28	409
$PbTiO_3$	4mm	411	0.92	17.8	4.3	0.08	137
		002	2.08	14.20	5.4	0.22	309
BeO	6mm	011	2.06	5.40	14.3	0.57	307
		201	1.13	6.50	11.9	0.26	168

and $\tau = L/\upsilon_{\shortparallel}$, the EDM effect is expressed as

$$\varphi^{\rm EDM} = \frac{d_n c^2}{\mu_n \hbar \upsilon_{\shortparallel}} \tag{4.25}$$

Thus, it can be seen that the EDM effect is not related to the strength of the effective intra-crystal electric field $E_g^{\rm eff}$, but related anti-proportional to $\upsilon_{\shortparallel}$. Of course, the stronger the effective intra-crystal electric field, the smaller the crystal thickness required for $\pi/2$ rotation, which is advantageous in terms of crystal availability. As seen in Table 4.1, the required thickness for the (110)-plane of α-quartz is 38.6 mm, while for the (433)-plane of $B1_{12}GeO_{20}$ it is only 14.8 mm. Since the EDM signal becomes larger as $\upsilon_{\shortparallel}$ becomes smaller, a crystal plane with a large lattice spacing d_g is advantageous, and $v_{\shortparallel}$ can be made smaller by setting the Bragg angle $\theta_{\rm B}$ to an angle close to 90 degrees. For example, for the (110)-plane of α-quartz with Bragg angle of 30 degrees, $\upsilon_{\shortparallel} = 1394$ m/s for the Bragg wavelength $\lambda_{\rm B} = 2.56$ Å. With Bragg angle of 87 degrees, $\upsilon_{\shortparallel} = 42$ m/s for the Bragg wavelength $\lambda_{\rm B} = 4.91$ Å, and the EDM effect becomes about 33 times larger. As can be seen from Eq. (4.11), the magnitude of the EDM effect is proportional to $E_g^{\rm eff}\tau$. In view of the above, the (110)-plane of α-quartz is the most promising candidate, especially considering the conditions (2) and (4), and $B1_{12}GeO_{20}$ or $B1_{12}SiO_{20}$ crystals are the next possibilities.

5 Overview of the Dynamical Diffraction from Experimental View Points

In the search for nEDM by crystal diffraction method, the dynamical diffraction theory, which deals with neutron diffraction in a crystal, is important. As discussed in Section 4.1, the existence of α- and β-waves due to multiple diffraction and interference is important in the nEDM search experiment. In this section, we describe our experimental investigations of the Pendellösung interference fringes and the spatial distribution of diffraction intensity, which are basic interference phenomena derived from the dynamical diffraction theory. To confirm these phenomena, we focused our experiments on the best crystal, Si crystal, and the most promising candidate, α-quartz. All experiments were performed at Materials and Life Science Experiment Facility (MLF) in Japan Proton Accelerator Research Complex (J-PARC), which is currently the world's most intense accelerator spallation pulsed neutron source, and these experiments were the first to be performed at a pulsed neutron source.

5.1 Pendellösung Fringes

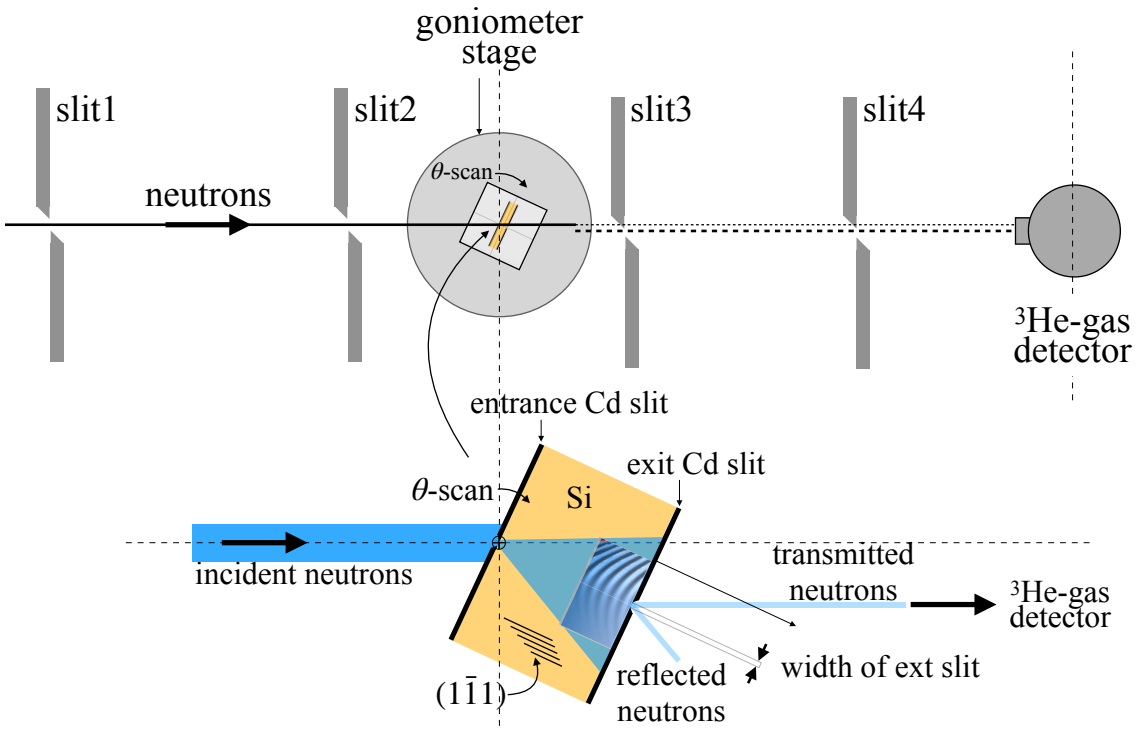

Figure 5.1: The schematic diagram of the experiment to observe the Pendellösung fringes:
Neutron beams collimated by slits 1 and 2 from the left are injected into a Si crystal set on the gonio-stage through the Cadmium entrance slit. Neutrons diffracted dynamically in the crystal are ejected from the ejection surface as transmitted and reflected beams. In the experiment, the transmitted beam ejected from the Cadmium exit slit was measured with the ^{3}He detector. Pendellösung fringes are observed by scanning and measuring the angle of incidence (Bragg angle) with the gonio-stage. Slits 3 and 4 were used to reduce the background.

In the two-wave approximation of the dynamical diffraction theory, we saw in Section 3.1.2 that the wave field of diffracted neutrons in a crystal can be expressed by Eq. (3.42). By dividing it into transmitted and reflected waves, the respective intensity distributions can be written as in Eq. (3.62) and Eq. (3.63) in section 3.1.3. Consider the case of the symmetric Laue configuration that exactly satisfies the Bragg condition,

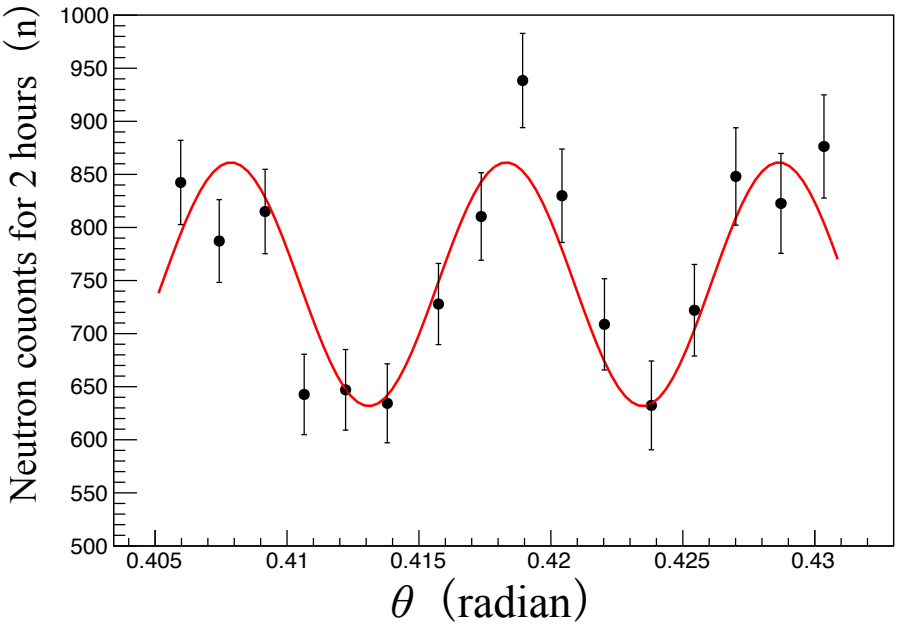

Figure 5.2: Pendellösung fringes of $(1\bar{1}1)$-plane of Si crystal:
The contrast of this Pendellösung fringes is (16 ± 2) %.

$y = 0$ and $b = 1$, and $V_g = V_{-g}$. Equation (3.62) and Eq. (3.63) become

$$I_0 = u_0^2 \cos^2 \left(\frac{\pi t}{\Delta_0} \sqrt{y^2 + 1} \right), \tag{5.1}$$

$$I_g = u_0^2 \sin^2 \left(\frac{\pi t}{\Delta_0} \sqrt{y^2 + 1} \right), \tag{5.2}$$

where Δ_0 is the Pendellösung length defined by Eq. (3.48) and t is the thickness of the crystal. As is clear from this, the diffraction intensity varies periodically with the thickness of the crystal. This periodic intensity distribution is called Pendellösung fringes or equal-thickness interference fringes. Since the phases of the transmitted and reflected waves are exactly $\pi/2$ out of phase, the intensity of the sum of these is constant (absorption is ignored). Equation (3.48) shows that the wavelength is a variable in Δ_0 and so in the phase term in Eq. (5.1) and (5.2), and therefore, interference fringes can be seen by scanning the Bragg angle θ_B.

We performed the Pendellösung fringes measurement using a pulsed neutron source [52]. The experiment was conducted at the beam line BL17 at MLF. The schematic diagram of the experimental setup is shown in Fig. 5.1. We used the Si crystal with a width of 50 mm, height of 50 mm, and thickness of 2.8 mm, which was cut out from a float-zone ingot. $(1\bar{1}1)$-plane was used for the experiment. The surfaces of the crystal were mechanically polished and finally finished by chemical wet etching in order to remove the abraded layers. The width of both the entrance and exit slits was 0.2 mm. The neutron beam divergence was 0.039 degrees. The transmitted neutrons were measured by the ^{3}He-gas detector with a gas pressure of 7 atmospheres. The incident angle to the crystal was scanned by the goniometer from $\theta = 25.0$ degrees to $\theta = 26.5$ degrees with step of 0.1 degrees, where θ was the set angle of the goniometer. The real Bragg angle θ_B was obtained from the value of the TOF-position of the diffraction peak. The measuring time of each step was two hours.

The measured Pendellösung fringes are shown in Fig. 5.2. The contrast of the obtained interference fringes is $16 \pm 2\%$. The scattering length of Si obtained from the period of the interference fringes is $b_{\mathrm{Si}} = (4.125 \pm 0.003^{\mathrm{stat}} \pm 0.028^{\mathrm{syst}})$ fm and is consistent with the NIST standard value. By observing the Pendellösung fringes, the interference effects in dynamical diffraction were successfully verified experimentally, using the pulsed neutron source.

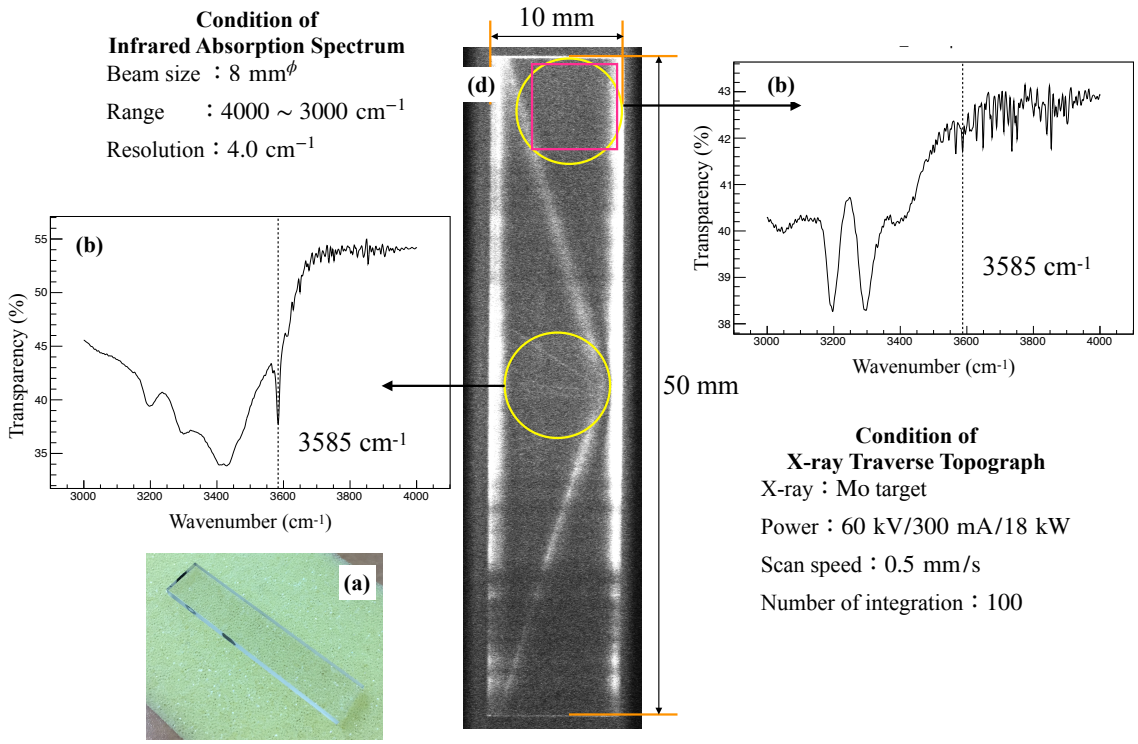

Figure 5.3: Evaluation of crystallinity by X-ray and the region used in the experiment:
(1) α-quartz used in the experiment. (2),(3) Infrared absorption spectra measured at the regions indicated by the yellow circles, respectively. (3) shows a difference against to (2) in the OH group absorption peak at 3585 cm^{-1}, indicating that there are fewer OH groups in (3) than in (2). (4) X-ray transmission traverse topography. The oblique emission lines are thought to be veins in the crystal. The red boxes indicate the region used in this experiment.

However, the contrast of the interference fringes is quite low, even taking into account the decrease due to the width of the incident and exit slits and the decrease due to the beam divergence angle. One possible cause is poor crystallinity. Si is a centrosymmetric crystal and will not be used in the nEDM search experiment. As the next step, we performed the same Pendellösung fringes measurement using α-quartz, which is the most promising candidate for the nEDM search experiment. (110)-plane was used for the experiment. The crystal used was an artificial quartz crystal with a width of 10 mm, a height of 50 mm, and a thickness of 2.8 mm. Since crystallinity is very important in the Pendellösung fringes measurement, we evaluated the crystallinity using X-rays to identify areas with good crystallinity and conducted the experiment. Figure 5.3 summarizes the results of the crystallinity evaluation using X-rays. The area used for the experiment (5mmx5mm surrounded by the red box in Fig. 5.3) was determined based on the results of X-ray topography and the measurement of infrared absorption spectra. . The experimental setup is almost the same as in the Si case. Since the Bragg angle to be scanned is slightly larger at 31 degrees, the entrance and exit slit widths are set to 0.3 mm, corresponding to the Borrmann fan spread. The results of the Pendellösung fringes measurement of α-quartz are shown in Fig. 5.4. It can be seen that the contrast is greatly improved to 55%.

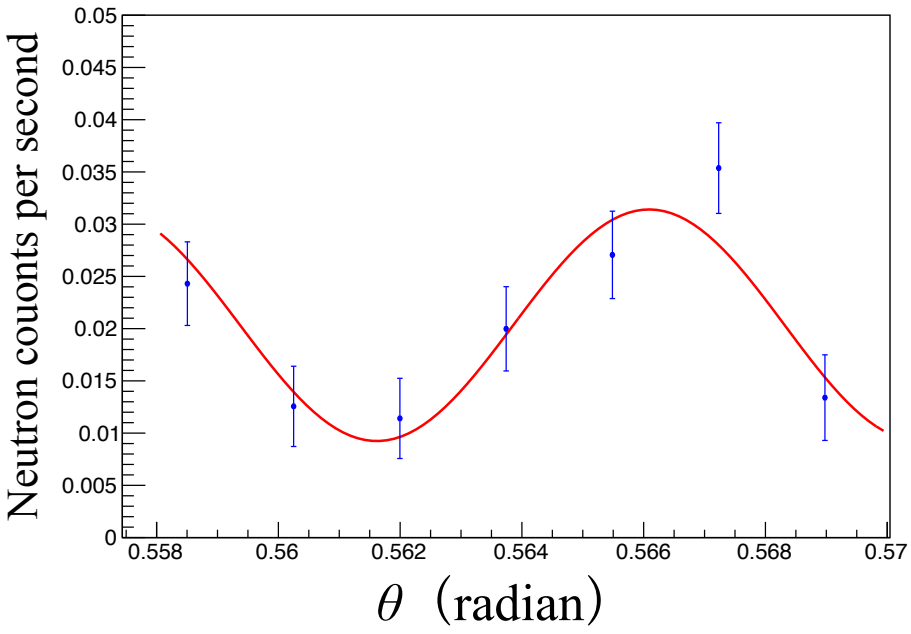

Figure 5.4: Pendellösung fringes of (110)-plane of α-quartz:
This Pendellösung fringes were demonstrated using non-polarized neutrons. The contrast of this is (55 ± 12) %.

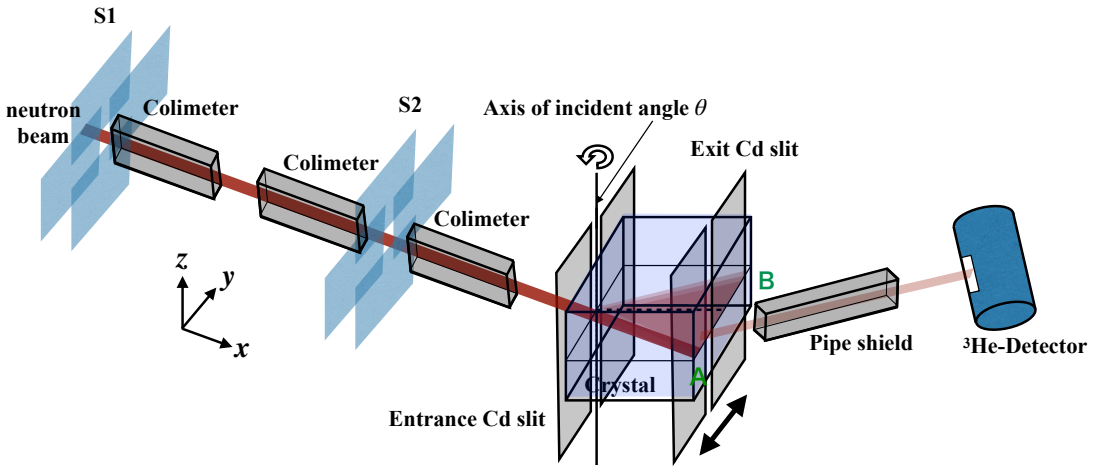

Figure 5.5: Setup of the experiment measuring the intensity distribution.
Neutrons incident on the crystal spread in the Bormann fan, indicated by the triangle in the figure, and produce an intensity distribution on the ejection plane. In the experiment, the intensity distribution was measured by scanning the exit slit along AB indicated in the figure.

5.2 Intensity Distribution on the Exit Surface

In the nEDM search experiment using crystal diffraction in the Laue configuration, only a small fraction of the diffracted neutrons that are widely spread in the Borrmann fan by dynamical diffraction are available. Therefore, it is important to know the intensity distribution as shown in Fig. 3.7 to estimate the fraction of neutrons that can be used to the experiment.

We measured the spatial intensity distribution of reflected waves by focusing on the average intensity distribution, because the detailed stripe pattern is not need to estimate the intensity of neutrons.

5.2.1 Measurement of the Intensity Distribution on the Exit Surface

The experiment was conducted at BL10 at MLF. The experimental setup is shown in Fig. 5.5. The crystal was the same α-quartz used in the Pendellösung fringes demonstration, and the same region with good crystallinity was used. The entrance slit of 0.5mm wide was fixed, and the exit slit of 0.2 mm wide was scanned along the exit surface. The Bragg angle was set to 40 degrees, and so the Borrmann fan spread was 4.7mm, since the thickness was 2.8 mm. In actually, the intensity distribution is wider than that due to the entrance and exit slits and the divergence angle. The scanning was performed at a pitch of 0.2 mm (partly at a pitch of 0.15 mm) over a range of 5.55 mm to cover the width of the Bormann fan. By making the entrance slit wider and taking a larger divergence angle of 0.43 degrees, the detailed stripe pattern was averaged out, making it easier to measure the average intensity distribution. The detector was ^{3}He gas detector and iIts detection window was reduced to the minimum size that could cover the measurement range. A shielding consisting of a pipe-shaped cadmium plate and boron rubber was installed between the crystal and the detector to reduce background. The beam size and divergence angle are adjusted at the quadrant slits, S1 and S2, and three iron collimators are placed before and after S2 to attenuate the fast neutrons.

5.2.2 Measurement Results of the Intensity Distribution

The–measurement results are shown in Fig. 5.6. There appears to be a constant shift in the data between the left side ($\Gamma < 0$) and the right side ($\Gamma > 0$). It is possible that the slit moved during the course of the experiment, but this is unknown. We will ignore this and examine whether the overall profile can be reproduced by plane wave theory.

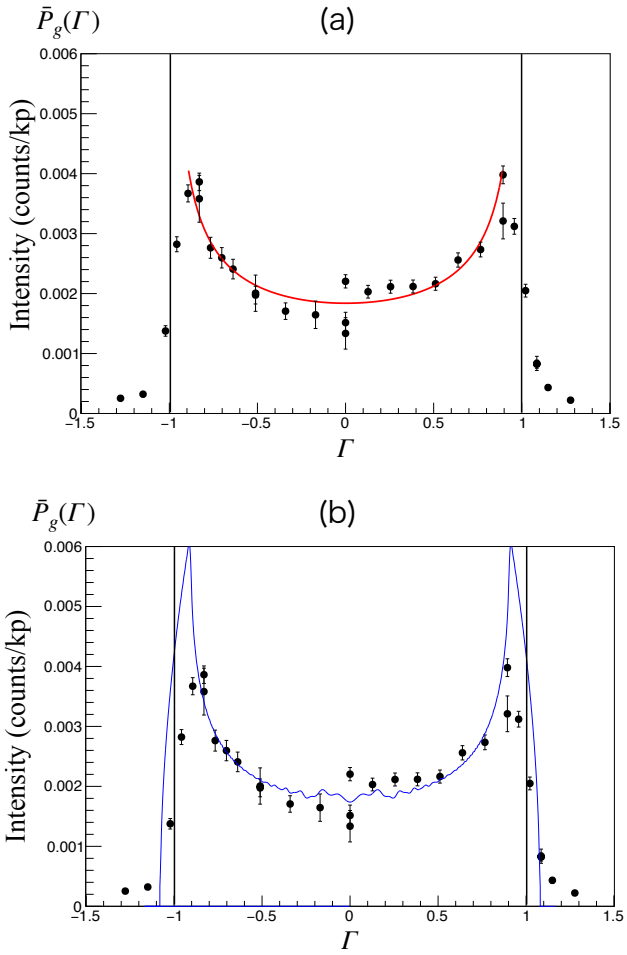

Figure 5.6: The results of experiment and the plane-wave theory:
(a): Plot of experimental results and results of the fit by the plane-wave theory mean intensity distribution equation. The fit range is from $\Gamma = -0.9$ to $\Gamma = +0.9$ because the equation diverges to infinity for $\Gamma = \pm 1$. The effects of slit width and divergence angle are not considered. (b): Plot of the experimental results overlaid with the calculated intensity distribution (blue line) with adjusted scale. Calculations were performed in the range of $\Gamma = \pm 0.999$. The entrance and exit slits are 0.5 mm and 0.2 mm, respectively, and the divergence angle is 0.34 degrees.

Figure 5.6 (a) shows the results of fitting the measured data in the range $\Gamma = -0.9 - \Gamma = +0.9$, using the mean reflection intensity distribution Eq. (3.84) in plane-wave theory. In this range, Eq. (3.84) is a good representation of the actual intensity distribution. However, the effects of entrance and exit slits and divergence angles are not considered. Figure 5.6 (b) shows the result of numerically calculated results (blue line) using Eq. (3.82) in the range of $\Gamma = -0.999 - \Gamma = +0.999$, considering the experimental conditions of 0.5mm entrance slit of 0.5mm, exit slit of 0.2mm, and 0.34degree divergence angle. The results reproduce a fairly averaged curve due to the effects of slit width and divergence angle. Thus, this experiment allows us to measure the average intensity distribution on the injection plane, which is in agreement with that predicted by plane wave theory, except around $\Gamma = \pm 1$.

A more realistic theory that describes diffraction phenomena is the spherical-wave theory. Here, the results of that theory will be shown only as follows,

$$P_0(\Gamma) = \frac{\pi^2 t}{2\Delta_0} \frac{1-\Gamma}{1+\Gamma} \mathscr{J}_1^2 \left(\frac{\pi t}{\Delta_0} \sqrt{1-\Gamma^2} \right), \tag{5.3}$$

$$P_g(\Gamma) = \frac{\pi^2 t}{2\Delta_0} \mathscr{J}_0^2 \left(\frac{\pi t}{\Delta_0} \sqrt{1-\Gamma^2} \right), \tag{5.4}$$

where $\mathscr{J}_{0,1}(x)$ is a Bessel function of first and second order, respectively. When the thickness t of the crystal is sufficiently large compared to the Pendellösung length Δ_0, Eq. (5.3) and (5.4) approximately agree with Eq. (3.81) and (3.82) in plane-wave theory.

There is also a statistical dynamical diffraction theory that deals with imperfect crystals, but this is not discussed here.

5.3 Calculation of the Intensity of Diffraction

The diffraction averaged intensity distribution is given by Eq. (3.83) and (3.84). As seen in the previous section, the actual diffraction intensity distribution was confirmed qualitatively for the reflected beam. Here, we attempt to predict the diffraction intensities quantitatively. Specifically, we calculate the diffraction intensities obtained from the Pendellösung fringes experiment conducted in April 2019; Fig. 5.7 shows the Pendellösung fringes at that time, whose diffraction intensities averaged 0.46 cps. The diffraction intensity can be calculated by the following equation,

$$\text{Diffraction intensity} = \text{Incident neutron intensity} \times \text{Diffraction factor} \times \text{Transmittance} \times \text{Other factors}. \tag{5.5}$$

(1) Incident neutron intensity I_{in}:

This is the neutron intensity incident on the slit on the incident plane of the crystal, and is determined by the source intensity and the geometrical conditions of the experimental setup. If the source intensity is I_{S} [n/cm^2/sec/sr/meV], the entrance slit area is S [cm^2], the beam solid angle viewed from the entrance slit is Ω [stradian], and the beam divergence angle is $\delta\theta$ [radian], the formula of the incident neutron intensity is given by

$$I_{\text{in}} = I_{\text{S}} \times S \times \Omega \times \delta E, \tag{5.6}$$

where δE is the neutron energy width corresponding to the divergence angle $\delta\theta$. Since the pulsed neutron source handles so-called white beams with continuous wavelength spectrum, neutrons with a certain energy width corresponding to the divergence angle are selected and diffracted by the Bragg condition. The energy width is given by

$$\delta E = \frac{2\pi\hbar^2}{m_n} \frac{4\pi d_g \cos\theta_{\text{B}}}{\lambda_{\text{B}}^3} \delta\theta. \tag{5.7}$$

(2) Diffraction factor DF:

A schematic diagram of the intensity of neutrons incident on the crystal in the symmetric Laue configuration and dynamically diffracted is shown in Fig. 5.8. The Lorenz curve in the center is that described by

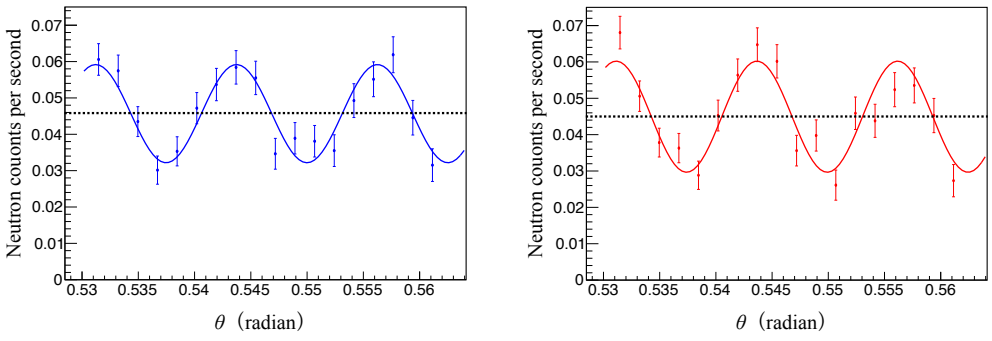

Figure 5.7: The results of Pendellösung fringes experiment in April 2019:
(The left and right sides are the results of Pendellösung fringes measurements when the spin direction of the incident neutron is parallel and antiparallel to the beam direction, respectively. Crystal is α-quartz, entrance and exit slits are 0.3 mm (actually 0.24 mm), beam height is 22.7 mm, divergence angle is 0.0012 radians, Bragg angle is 31 degrees, solid angle is 2.52×10^{-5} sr, with polarizer, without analyzer, detector efficiency is 0.95.

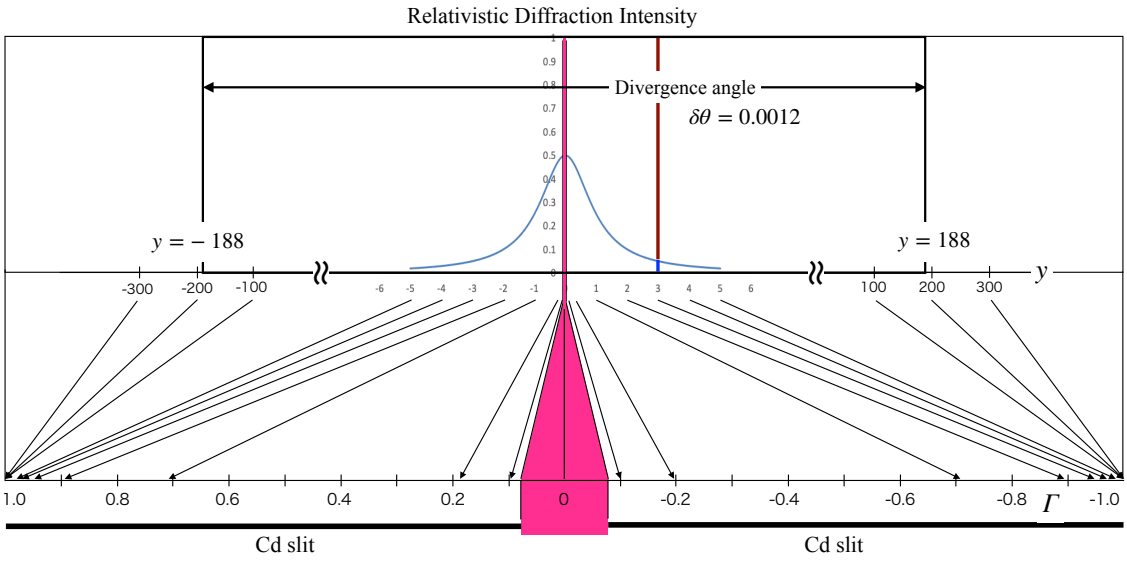

Figure 5.8: Schematic diagram of the calculation of the intensity of diffracted neutrons:
The upper square box represents the intensity distribution of isotropically incident neutrons at a given divergence angle, which is normalized to 1. The blue rocking curve represents the angular dependence of reflected diffracted neutrons in a symmetric Laue configuration, where the lower part of the curve is the reflected diffraction intensity and the upper part is the transmitted diffraction intensity. The value of y is proportional to the deviation from the Bragg angle, for example, if the divergence angle is 0.0012 radians, the value of y is equal to ± 188. The lower horizontal axis represents Γ, and the arrow represents the neutron current of the incident neutron from at a deviation y toward the ejection position Γ indicated by the arrow. As can be seen, the neutron current rapidly converges to $\Gamma = \pm 1$ for small values of y. In other words, only the region with a very small y, shown in red, is ejected from the Cd slits shown at the bottom.

the Eq. (3.66) in Section 3.4. It plots the reflected diffraction intensity in the symmetric Laue configuration with a parameter y, which is the deviation from the Bragg angle. The square height 1 box shows the neutron intensity at a given wavelength incident isotropically over the range of divergence angles. The lower part of the rocking curve represents the reflected diffraction intensity, and the upper part represents the transmitted diffraction intensity distribution. For neutrons incident at the center of the figure, i.e., exactly at the Bragg condition, 1/2 of them are reflected and 1/2 are transmitted; for deviations from the Bragg angle, e.g., $y = 3$, only 1/20 are reflected and the remaining 19/20 are transmitted. On the other hand, there is the following relationship between y and the normalized coordinate Γ of the projection plane;

$$y = -\frac{\Gamma}{\sqrt{1-\Gamma^2}}, \quad \Gamma = -\frac{y}{\sqrt{1+y^2}}. \tag{5.8}$$

This means that, in the neutron current concept, if $y = 0$, i.e., the Bragg condition is exactly satisfied, then neutrons are ejected from $\Gamma = 0$, and if $y = 3$, then ejected from $\Gamma = 0.949$. In the experiment, Cd slits are also installed on the ejection side, so that only neutrons within the range of y corresponding to Γ constrained by the Cd slits are ejected from the Cd slits. Considering neutrons of a given wavelength, of the neutrons isotropically incident within the range of divergence angles (corresponding to the square box), only the part shown in red in the figure will be ejected from the Cd slits. The Γ and y value corresponding to the width of the ejected Cd slits is noted $\pm\Gamma_s$ and y_s, respectively, and then the diffraction factor DF for transmitted beam is given by

$$y_s = -\frac{\Gamma_s}{\sqrt{1-\Gamma_s^2}}, \quad \int_{-y_s}^{+y_s} \left(\frac{1+2y^2}{2(1+y^2)}\right) \mathrm{d}y = 2y_s - \tan^{-1} y_s, \tag{5.9}$$

$$DF = -\frac{2y_s - \tan^{-1} y_s}{\Delta_0 \delta\theta / d_g}. \tag{5.10}$$

(3) Transmittance T:

Assuming that the absorption cross section of the crystalline material is σ, the Avogadro number is N_{A}, the density is ρ, the molar mass is M_{mol}, and the thickness of the crystal is t, the transmittance T is given by the following equation;

$$T = 1 - \exp\left(\frac{N_{\mathrm{A}}\rho\sigma t}{M_{\mathrm{mol}}}\right). \tag{5.11}$$

(4) Other factors:

These will vary depending on the experimental apparatus and method, including the presence or absence of polarization and analyzer, and the efficiency of the detector.

Based on the above results, the diffraction intensity for the April 2019 experiment is calculated to be 0.1 counts per second (cps) against the experimental value of 0.46 cps. In another case, if we look at the Pendellösung fringes measurement experiment in Fig. 5.4 in Section 5.1, the diffraction intensity of the experimental result is 0.2 cps, while the calculated result is 0.44 cps. The difference between the two experimental results is due to the experimental conditions. Both results have a discrepancy of about a factor of 2 from the experimental results, but this has not been clarified at this time. When we discuss the experimental possibilities of the nEDM search experiment later, we will have to multiply the efficiency by 0.5 when estimating the diffraction intensities there.

6 Theory of the Intra-Crystal Electric Field

In Section 4.1 (see Fig. 4.1), we noted that neutrons dynamically diffracting in a crystal consist of two components, α- and β-waves, and that in certain non-centrosymmetric crystals, each of them feels an effective intra-crystal electric field in the opposite direction. In nEDM search experiments by the crystal diffraction method, this effective intra-crystal electric field plays an important role. So far, it has been assumed that components other than α- and β-waves do not contribute anything. As discussed in Section 3.4, they can be neglected in terms of intensity because they are spatially oscillating components with the lattice period. However, in the discussion of the effective intra-crystal electric field of α- and β-waves, lattice periodic oscillations are important in the interaction of neutrons with the electric potential in the crystal. It needs to be investigated whether these components, which have been ignored so far in nEDM search experiments using crystal diffraction, may leave some residual effects.

We now re-examine the theory of the effective intra-crystal electric field interacted with neutrons dynamically diffracting in a crystal. From Eq. (3.42), the intensity distribution of neutrons inside a crystal is as follows,

$$\begin{aligned} I &= |\Psi_{\rm cry}(\boldsymbol{r})|^2 \\ &= \psi_0^{(1)}\psi_0^{(1)*} + \psi_0^{(2)}\psi_0^{(2)*} + \psi_g^{(1)}\psi_g^{(1)*} + \psi_g^{(2)}\psi_g^{(2)*} + \psi_0^{(1)}\psi_0^{(2)*} + \psi_0^{(2)}\psi_0^{(1)*} + \psi_g^{(1)}\psi_g^{(2)*} + \psi_g^{(2)}\psi_g^{(1)*} \\ &\quad + \psi_0^{(1)}\psi_g^{(1)*} + \psi_g^{(1)}\psi_0^{(1)*} + \psi_0^{(2)}\psi_g^{(2)*} + \psi_g^{(2)}\psi_0^{(2)*} + \psi_0^{(1)}\psi_g^{(2)*} + \psi_0^{(2)}\psi_g^{(1)*} + \psi_g^{(1)}\psi_0^{(2)*} + \psi_g^{(2)}\psi_0^{(1)*}. \end{aligned} \tag{6.1}$$

Thus, the intensity distribution in the crystal consists of 16 components, which are combinations of four Bloch waves.

The periodic electric potential in the crystal can be Fourier expanded in terms of the reciprocal lattice vector $\boldsymbol{g}$ and written as in Eq. (4.7). In the two-wave approximation, the only effective Fourier component of the periodic potential in the crystal is the $\boldsymbol{g}$ component, but in the multiple diffraction repeated reflection and transmission also interact with the $-\boldsymbol{g}$ component, so the periodic electric potential can be written as follows,

$$\begin{aligned} U^{\rm E}(\boldsymbol{r}) &= U_g^{\rm E}\exp(\mathrm{i}\boldsymbol{g}\cdot\boldsymbol{r}) + U_{-g}^{\rm E}\exp(-\mathrm{i}\boldsymbol{g}\cdot\boldsymbol{r}) \\ &= v_g^{\rm E}e^{i\phi_g^{\rm E}}\exp(\mathrm{i}\boldsymbol{g}\cdot\boldsymbol{r}) + v_g^{\rm E}e^{-i\phi_g^{\rm E}}\exp(-\mathrm{i}\boldsymbol{g}\cdot\boldsymbol{r}) \\ &= 2v_g^{\rm E}\cos\left(\boldsymbol{g}\cdot\boldsymbol{r}+\phi_g^{\rm E}\right), \end{aligned} \tag{6.2}$$

where $v_g^{\rm E}$ is the amplitude of the electric potential and ϕ_g^E is the phase shift of that relative the crystal lattice plane. $U^{\rm E}$ is the electric potential that exists within the crystal and must be distinguished from the potential $V^{\rm N}$, $V^{\rm S}$, and $V^{\rm E}$ with which the neutron interacts. The main periodic potential in a crystal with which neutrons interact is the nuclear potential based on the nuclear force, which can be written, as in Eq. (6.2),

$$V^{\rm N}(\boldsymbol{r}) = 2v_g^{\rm N}\cos\left(\boldsymbol{g}\cdot\boldsymbol{r}+\phi_g^{\rm N}\right), \tag{6.3}$$

where $v_g^{\rm N}$ is the amplitude of the electric potential and $\phi_g^{\rm N}$ is the phase shift of that relative the crystal lattice plane. What is important in considering the effective intra-crystal electric field in a crystal is the difference in phase $\Delta\phi_g = \phi_g^{\rm E} - \phi_g^{\rm N}$. The nuclear potential $V^{\rm N}$ is much larger than the other potential, $V^{\rm S}$ and $V^{\rm E}$, and so the wave field is almost entirely determined by the nuclear force potential, which is equivalent to placing the origin of the wave field at a lattice point. Namely, $\phi_g^{\rm N} = 0$. Therefore, from now on $\phi_g^{\rm E} = \Delta\phi_g$. The electric field in a crystal can be calculated as

$$\boldsymbol{E}_g(\boldsymbol{r}) = -\nabla U_g^{\rm E}(\boldsymbol{r}) = 2v_g^{\rm E}\boldsymbol{g}\sin(\boldsymbol{g}\cdot\boldsymbol{r}+\Delta\phi_g). \tag{6.4}$$

The expected value of the electric field interacted with neutrons dynamically diffracting inside a crystal,

which is the effective intra-crystal electric field, can be obtained as follows,

$$\begin{aligned}\boldsymbol{E}_g^{\mathrm{eff}}(\boldsymbol{r}) &= \langle \Psi_{\mathrm{cry}}(\boldsymbol{r}) |\, \boldsymbol{E}_g(\boldsymbol{r})\, | \Psi_{\mathrm{cry}}(\boldsymbol{r}) \rangle \\ &= \frac{1}{d_g}\int_0^{d_g} \boldsymbol{E}_g(\boldsymbol{r}) |\Psi_{\mathrm{cry}}(\boldsymbol{r})|^2 \mathrm{d}\boldsymbol{r}.\end{aligned} \tag{6.5}$$

Equation (6.5) can be resolved into 16 terms according to Eq. (6.1). For example, let us calculate the effective intra-crystal electric field for the 9-th term of $|\Psi_{\mathrm{cry}}(\boldsymbol{r})|^2$ in Eq. (6.1).

$$\psi_0^{(1)}\psi_g^{(1)*} = u_0^{(1)} \exp\Big(\mathrm{i}\boldsymbol{K}_0^{(1)}\cdot\boldsymbol{r}\Big) u_g^{(1)} \exp\Big(-\mathrm{i}\boldsymbol{K}_g^{(1)}\cdot\boldsymbol{r}\Big). \tag{6.6}$$

The effective intra-crystal electric field is

$$\boldsymbol{E}_g^{\mathrm{eff}-9}(\boldsymbol{r}) = \frac{1}{d_g}\frac{\int_0^{d_g} \boldsymbol{E}_g(\boldsymbol{r})\psi_0^{(1)}\psi_g^{(1)*}\mathrm{d}\boldsymbol{r}}{|\psi_0^{(1)}\psi_g^{(1)*}|}. \tag{6.7}$$

Taking the $\boldsymbol{x}$-coordinate in the $\boldsymbol{g}$ direction, the equation becomes the following integral, which yields the effective intra-crystal electric field

$$\begin{aligned}\boldsymbol{E}_g^{\mathrm{eff}-9}(\boldsymbol{r}) &= \frac{1}{d_g}\frac{\int_0^{d_g} 2v_g^{\mathrm{E}}\boldsymbol{g}\sin(gx+\Delta\phi_g)u_0^{(1)}u_g^{(1)}\cos(gx)\mathrm{d}\boldsymbol{r}}{|u_0^{(1)}u_g^{(1)}|} \\ &= v_g^{\mathrm{E}}\boldsymbol{g}\sin(\Delta\phi_g).\end{aligned} \tag{6.8}$$

Table 6.1 lists the intensity distributions for the 16 terms and the effective intra-crystal electric field with which each component interacts. In this table, $\Delta\boldsymbol{K} = \boldsymbol{K}_0^{(1)} - \boldsymbol{K}_0^{(2)}$. Terms 1 – 4 represent the intensities of the four Bloch waves, respectively, which are spatially constant and do not contribute to the generation of the effective intra-crystal electric field. Terms 5, 6, and 7, 8 represent the Pendellösung interference of transmitted and reflected waves, respectively, which produces a spatial distribution in the direction of the crystal thickness, but it is constant in the direction perpendicular to the crystal plane, and thus does not contribute to the generation of the effective intra-crystal electric field. Terms 9, 10, and 11, 12 represent the inter-lattice interference of α- and β-waves, respectively. In the symmetric Laue configuration, $u_0^{(1)} = u_0^{(2)} = -u_g^{(1)} = u_g^{(2)} = 1/2$, so the electric field interacting with the α-wave is $(-v_g^{\mathrm{E}}\boldsymbol{g}\sin\Delta\phi_g)$ and the electric field interacting with the β-wave is $(+v_g^{\mathrm{E}}\boldsymbol{g}\sin\Delta\phi_g)$. If $\Delta\phi_g = 0$, there is no effective intra-crystal electric field. So far, this is what is generally understood as the effective intra-crystal electric field interacting with neutrons under the dynamical diffraction in a crystal.

We now turn our attention to the remaining terms 13–16. The effective intra-crystal electric field in these terms includes the $\cos\Delta\phi_g$ term, which contributes to the generation of the effective intra-crystal electric field even when $\Delta\phi_g = 0$. However, as can be easily seen, these terms have $\sin(\Delta\boldsymbol{K}\cdot\boldsymbol{r})$ or $\cos(\Delta\boldsymbol{K}\cdot\boldsymbol{r})$ factors that follow the Pendellösung oscillation and thus cancel out when integrated in the crystal thickness direction. A thickness contribution on the order of the Pendellösung length may remain, but it is negligible: for the (110)-plane of α-quartz with a Bragg angle of 30 degrees, the Pendellösung length is $\Delta_0 = 0.08$ mm, which is less than 1% for a 10 mm thick crystal. Therefore, we have concluded that for $\Delta\phi_g = 0$, there is no effective intra-crystal electric field in a crystal.

In general, Pendellösung interference fringes can never be observed with contrast of 100%. This is partly due to the divergence angle of the neutron beam and other geometrical factors, and it is also largely due to imperfections in the crystal, i.e. defects of crystal. Thus, if the Pendellösung interference is partially broken, oscillating components that should cancel each other may remain uncanceled. In such a case, the interference terms 13–16 cannot be neglected and an effective intra-crystal electric field may be generated even at $\Delta\phi_g = 0$.

We have measured and studied the effective intra-crystal electric field due to spin rotations of dynamically diffracted neutrons from both crystal planes with $\Delta\phi_g \neq 0$ and $\Delta\phi_g = 0$.

Table 6.1: Summary of 16 components.

Summary of the intensity distribution and the effective intra-crystal electric field for 16 components in Eq. (6.1). $\Delta\boldsymbol{K} = \boldsymbol{K}_0^{(1)} - \boldsymbol{K}_0^{(2)}$.

Term	Component	Intensity distribution	Effective intra-crystal electric field
1	$\psi_0^{(1)}\psi_0^{(1)*}$	$\left(u_0^{(1)}\right)^2$	0
2	$\psi_0^{(2)}\psi_0^{(2)*}$	$\left(u_0^{(2)}\right)^2$	0
3	$\psi_g^{(1)}\psi_g^{(1)*}$	$\left(u_g^{(1)}\right)^2$	0
4	$\psi_g^{(2)}\psi_g^{(2)*}$	$\left(u_g^{(2)}\right)^2$	0
5	$\psi_0^{(1)}\psi_0^{(2)*}$	$u_0^{(1)}u_0^{(2)}\cos(\Delta\boldsymbol{K}\cdot\boldsymbol{r})$	0
6	$\psi_0^{(2)}\psi_0^{(1)*}$	$u_0^{(1)}u_0^{(2)}\cos(\Delta\boldsymbol{K}\cdot\boldsymbol{r})$	0
7	$\psi_g^{(1)}\psi_g^{(2)*}$	$u_g^{(1)}u_g^{(2)}\cos(\Delta\boldsymbol{K}\cdot\boldsymbol{r})$	0
8	$\psi_g^{(2)}\psi_g^{(1)*}$	$u_g^{(1)}u_g^{(2)}\cos(\Delta\boldsymbol{K}\cdot\boldsymbol{r})$	0
9	$\psi_0^{(1)}\psi_g^{(1)*}$	$u_0^{(1)}u_g^{(1)}\cos(\boldsymbol{g}\cdot\boldsymbol{r})$	$-v_g^{\mathrm{E}}\boldsymbol{g}\sin\Delta\phi_g$
10	$\psi_g^{(1)}\psi_0^{(1)*}$	$u_g^{(1)}u_0^{(1)}\cos(\boldsymbol{g}\cdot\boldsymbol{r})$	$-v_g^{\mathrm{E}}\boldsymbol{g}\sin\Delta\phi_g$
11	$\psi_0^{(2)}\psi_g^{(2)*}$	$u_0^{(2)}u_g^{(2)}\cos(\boldsymbol{g}\cdot\boldsymbol{r})$	$v_g^{\mathrm{E}}\boldsymbol{g}\sin\Delta\phi_g$
12	$\psi_g^{(2)}\psi_0^{(2)*}$	$u_g^{(2)}u_0^{(2)}\cos(\boldsymbol{g}\cdot\boldsymbol{r})$	$v_g^{\mathrm{E}}\boldsymbol{g}\sin\Delta\phi_g$
13	$\psi_0^{(1)}\psi_g^{(2)*}$	$u_0^{(1)}u_g^{(2)}\left[\cos(\Delta\boldsymbol{K}\cdot\boldsymbol{r})\cos(\boldsymbol{g}\cdot\boldsymbol{r})+\sin(\Delta\boldsymbol{K}\cdot\boldsymbol{r})\sin(\boldsymbol{g}\cdot\boldsymbol{r})\right]$	$v_g^{\mathrm{E}}\boldsymbol{g}\left[\cos(\Delta\boldsymbol{K}\cdot\boldsymbol{r})\sin\Delta\phi_g+\sin(\Delta\boldsymbol{K}\cdot\boldsymbol{r})\cos\Delta\phi_g\right]$
14	$\psi_0^{(2)}\psi_g^{(1)*}$	$u_0^{(2)}u_g^{(1)}\left[\cos(\Delta\boldsymbol{K}\cdot\boldsymbol{r})\cos(\boldsymbol{g}\cdot\boldsymbol{r})-\sin(\Delta\boldsymbol{K}\cdot\boldsymbol{r})\sin(\boldsymbol{g}\cdot\boldsymbol{r})\right]$	$-v_g^{\mathrm{E}}\boldsymbol{g}\left[\cos(\Delta\boldsymbol{K}\cdot\boldsymbol{r})\sin\Delta\phi_g-\sin(\Delta\boldsymbol{K}\cdot\boldsymbol{r})\cos\Delta\phi_g\right]$
15	$\psi_g^{(1)}\psi_0^{(2)*}$	$u_g^{(1)}u_0^{(2)}\left[\cos(\Delta\boldsymbol{K}\cdot\boldsymbol{r})\cos(\boldsymbol{g}\cdot\boldsymbol{r})-\sin(\Delta\boldsymbol{K}\cdot\boldsymbol{r})\sin(\boldsymbol{g}\cdot\boldsymbol{r})\right]$	$-v_g^{\mathrm{E}}\boldsymbol{g}\left[\cos(\Delta\boldsymbol{K}\cdot\boldsymbol{r})\sin\Delta\phi_g-\sin(\Delta\boldsymbol{K}\cdot\boldsymbol{r})\cos\Delta\phi_g\right]$
16	$\psi_g^{(2)}\psi_0^{(1)*}$	$u_g^{(2)}u_0^{(1)}\left[\cos(\Delta\boldsymbol{K}\cdot\boldsymbol{r})\cos(\boldsymbol{g}\cdot\boldsymbol{r})+\sin(\Delta\boldsymbol{K}\cdot\boldsymbol{r})\sin(\boldsymbol{g}\cdot\boldsymbol{r})\right]$	$v_g^{\mathrm{E}}\boldsymbol{g}\left[\cos(\Delta\boldsymbol{K}\cdot\boldsymbol{r})\sin\Delta\phi_g+\sin(\Delta\boldsymbol{K}\cdot\boldsymbol{r})\cos\Delta\phi_g\right]$

7 The Measurement of Intra-Crystal Electric Field by Spin Rotation

In this section, experimental methods and results are described for an experiment measuring the effective intra-crystal electric field using the spin rotation due to the Schwinger magnetic field. The measurement of the effective intra-crystal electric field by the Schwinger magnetic field in the symmetric Laue configuration was performed by Voronin and co-workers [53]. They used the fact that the amount of precession oscillates with the angle between the direction of the Schwinger magnetic field and the direction of the incident spins in order to confirm the spin precession by the Schwinger magnetic field and to measure the effective intra-crystal electric field. We have carried out similar measurements by varying the thickness of the crystal.

7.1 Theory of the Measurement

The principle of measuring the effective intra-crystal electric field using the spin rotation due to the Schwinger magnetic field is basically the same as the principle of nEDM measurement (see Fig. 4.2). When neutrons with spins polarized in the x-direction are injected into the crystal, the dynamically diffracted neutrons are split into α- and β-waves, which undergo precessional rotation around the Schwinger magnetic field and the effective intra-crystal electric field in opposite directions, respectively. In the nEDM search experiment, the nEDM effect appears in the z-direction. On the other hand, here we measure the spin polarization in the x-direction. Here, the spin polarization in the z-direction due to nEDM is very small and can be neglected.

The rotation angle φ_{S} of the precession due to the Schwinger magnetic field is given by the following equation when the thickness of the crystal is t.

$$\varphi_{\mathrm{S}} = \frac{2\mu_n B_{\mathrm{S}}}{\hbar}\tau = \frac{2\mu_n E_g t}{\hbar c^2} \tag{7.1}$$

Since the direction of the effective intra-crystal electric field is opposite for α-wave and β-wave, each angle of precession, $\varphi^{\alpha}_{\mathrm{obs}}$ or $\varphi^{\beta}_{\mathrm{obs}}$, are opposite and of equal magnitude;

$$\varphi^{\alpha}_{\mathrm{obs}} = \varphi_s + \varphi_0, \tag{7.2}$$

$$\varphi^{\beta}_{\mathrm{obs}} = -\varphi_s + \varphi_0, \tag{7.3}$$

where φ_0 is the initial polarization $P_0 = \cos\varphi_0$. The polarization of α-wave and β-wave can be written as $P^{\alpha}_{\mathrm{obs}} = \cos\varphi^{\alpha}_{\mathrm{obs}}$ and $P^{\beta}_{\mathrm{obs}} = \cos\varphi^{\beta}_{\mathrm{obs}}$, respectively. However, since the α- and β-waves cannot be observed separately, the sum of the two can be observed. Under the condition that the α- and β-waves have the same intensity in a symmetric Laue configuration, the observed polarization P_{obs} becomes

$$\begin{aligned} P_{\mathrm{obs}} &= \frac{1}{2}\left(P^{\alpha}_{\mathrm{obs}} + P^{\beta}_{\mathrm{obs}}\right) \\ &= \cos\varphi_{\mathrm{S}}\cos\varphi_0 \end{aligned} \tag{7.4}$$

Therefore, by measuring the initial polarization and the polarization after precession by the Schwinger magnetic field, the effective intra-crystal electric field can be obtained as follows.

$$\frac{P_{\mathrm{obs}}}{P_0} = \cos\varphi_S, \tag{7.5}$$

$$\frac{P_{\mathrm{obs}}}{P_0} = \cos\frac{2\mu_n E_g t}{\hbar c^2}, \tag{7.6}$$

In the experiment, the measurement was performed by tilting the crystal around the axis in Fig. 7.1, changing the effective thickness of the crystal. If the tilt angle is ξ and the offset of the tilt angle is ξ_0, Eq. (7.6) is expressed as follows.

$$\frac{P_{\mathrm{obs}}}{P_0} = \cos\frac{2\mu_n E_g}{\hbar c^2}\frac{t}{\cos(\xi - \xi_0)}, \tag{7.7}$$

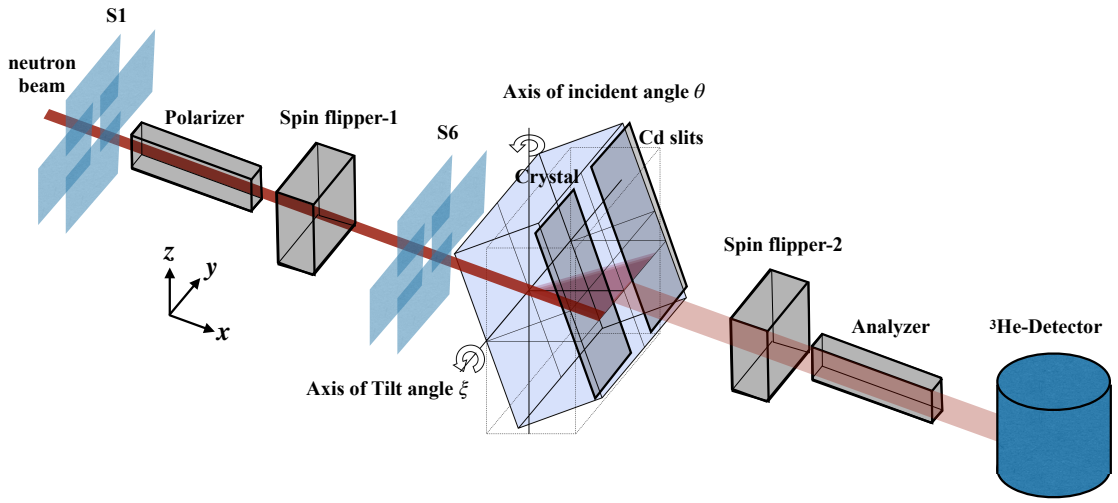

Figure 7.1: Setup of the experiment of the spin rotation:
The neutron beam was shaped by S1 and S6 to be a width of 2 mm and a height of 5 mm at the crystal incidence plane. Spin polarization was done by Polarizer in the direction of the beam axis, and then selectable between parallel (p-mode) and antiparallel (m-mode) to the beam axis by the spin flipper-1. The detected beam width was set by the Cd slit on the neutron ejection plane. The width of the Cd slit was adjusted to detect the same fraction of the diffraction spread (the Borrmann fan) in the center. The direction of the detected neutron spins can be switched between p-mode and m-mode by the spin flipper-2 and the analyzer. The detector is a ^{3}He detector.

7.2 Setup of the Experiment

The experiment was carried out at the MLF in the J-PARC. A schematic diagram of the experiment is shown in Fig. 7.1. The spin of neutrons polarized by the upstream polarizer is maintained along the beam axis by a guiding magnetic field. The direction of the neutron spins can be switched between parallel and antiparallel to the beam axis by means of a spin π flipper after the polarizer. The crystal is held in an aluminum holder. A cadmium slit is placed in front of the injection plane and its width is fixed at 0.6 mm. The incident neutrons are collimated by slit S1 and the incident cadmium slit, and their divergence angle is 0.04 degrees. The crystal is α-quartz, and the diffraction plane is (110). The cadmium slit was also placed on the backside of the crystal, and its width was adjusted to detect the same fraction of the diffraction spread (the Borrmann fan) in the center. Of the diffracted neutron beam, only the transmitted beam passing through the cadmium slit on the injection surface is detected. The spin π flipper is placed in front of the spin analyzer to switch between the spin parallel to the beam axis and the spin antiparallel to the beam axis for detection. In the experiment, four different modes were measured while switching between them for different combinations of incident and detected spin orientations. The four modes are represented by pp, pm, mm, and mp, where the direction parallel to the beam axis is "plus (p)" and the direction antiparallel to the beam axis is "minus (m)". In the experiment, the measurements were performed by sequentially switching between pp and mm modes for 10s and pm and mp modes for 60s. Since the counts in the pm and mp modes are lower than in the pp and mm modes, they were set so that the statistics were approximately the same in each mode. The detector is a ^{3}He 0-dimensional detector. No special magnetic shields or guiding magnetic fields were installed before and after the crystal, but the residual magnetic field plus the Earth's magnetic field were left in place, and the effect of these fields was corrected by measuring the magnetic fields before and after the crystal. Outside the crystal, the magnetic field environment around the crystal and the guiding magnetic field environment before and after the crystal are connected loosely coupled enough to keep the neutron spins remain adiabatically oriented in the direction of the magnetic field. The initial polarization was measured with and without the crystal, with the direct beam polarization measured in the undiffracted state at an angle of incidence of 90 degrees to the crystal.

The α-quartz used in the experiment were 30 mm in diameter and 10 mm in thickness. The artificial

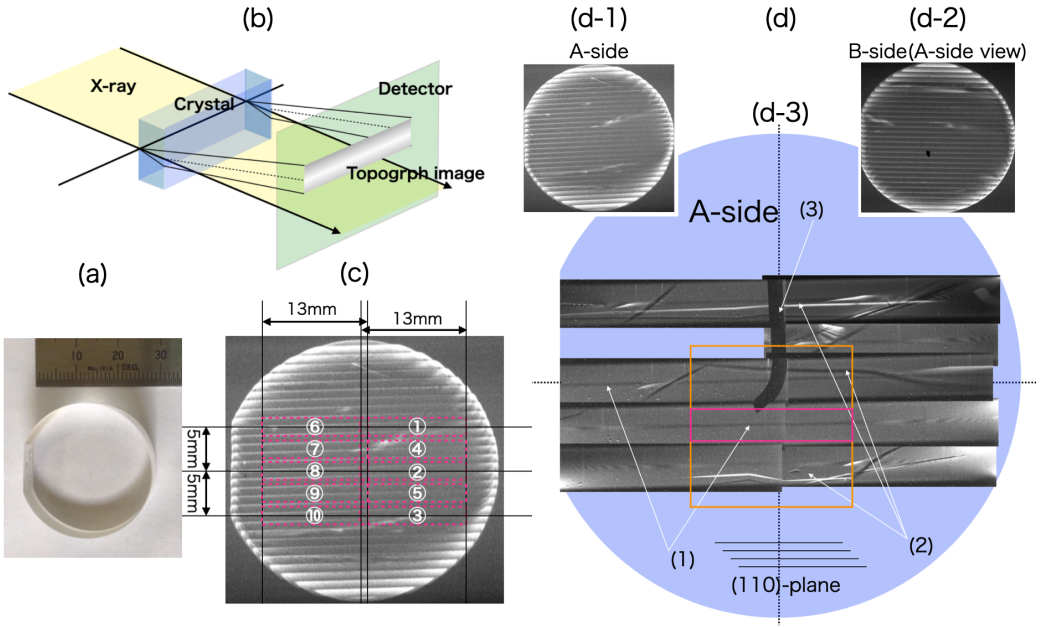

Figure 7.2: Evaluation of crystallinity by X-ray and determination of the measurement region.
(a) Appearance of α-quartz. The diameter is 30 mm and the thickness is 10 mm. The straight part on the left side is for directional identification. (b) Schematic diagram of the X-ray transmission topography. (c) Location of the X-ray transmission topography. (d) Topography results. (d-1),(d-2) The measurement results of the reflection X-ray topography are shown. A few bright lines can be seen, but many areas are good on the surface. (d-3) shows the results of transmission X-ray topography. The dark line in the center shown in (1) indicates that the Pendellösung fringes are visible. The bright and dark lines shown in (2) are considered to be veining during crystal growth. More veining can be seen than on the surface. The area indicated by the yellow frame is the area used in the experiment, and the red frame shows the neutron incident area.

crystals were manufactured by Nihon Dempa Kogyo and are the highest grade in the industry standard. An example of the standard is shown in Table 7.1. Prior to the experiment, X-ray topographic measurements were made, and an area (10 mm x 10 mm) with good crystallinity was selected for the experiment. The appearance of the crystals and the results of the X-ray transmission topography measurements are shown in Fig. 7.2. Several defect structures were observed, which are thought to be veins associated with crystal growth. The experimental area was chosen so that these striae would not enter the Borrmann fan as much as possible. The rectangular box in the figure shows the area used in the experiment.

Table 7.1: Industry Standard for an artificial α-quartz.
This table complies with IEC60758. This shows the highest grade standards: grade 1a for foreign particles, grade Aa for infrared absorption coefficient, and grade 1aa for etch channel density.

Foreign particles (Size and allowable number of foreign particles in 1 cm^3			
10–30 μm	30–70 μm	70–100 μm	100 μm ¡
≤ 2	≤ 1	0	0
Infrared absorption coefficient (wave length 3585 cm^{-1}			Q-value (Reference)
$\leq$ 0.015			$\geq 3.8 \times 10^5$
Etch channel density (cm^{-3})			
$\leq$ 2			

7.3 The Preliminary Experiment

Prior to this experiment, a preliminary experiment was carried out in the same experimental setup with a solenoid coil in place of the crystal to measure the spin rotation due to the magnetic field of the solenoid coil. The direction of the solenoid magnetic field was set to be in the z direction of Fig. 7.1, parallel to the Schwinger magnetic field $\boldsymbol{B}_{\mathrm{S}}$ in this experiment. Since the incident neutrons perform spin rotation proportional to the time they pass through the solenoid, the TOF spectrum of their polarization shows oscillations as shown in Fig. 7.3, and the solenoid magnetic field can be obtained from its period. The length of the path for neutrons to pass through the solenoid is 120 mm, and four different solenoid magnetic fields were measured: 1.0, 2.5, 5.0, and 7.0 Gauss ($\pm$ 0.1 Gauss each).

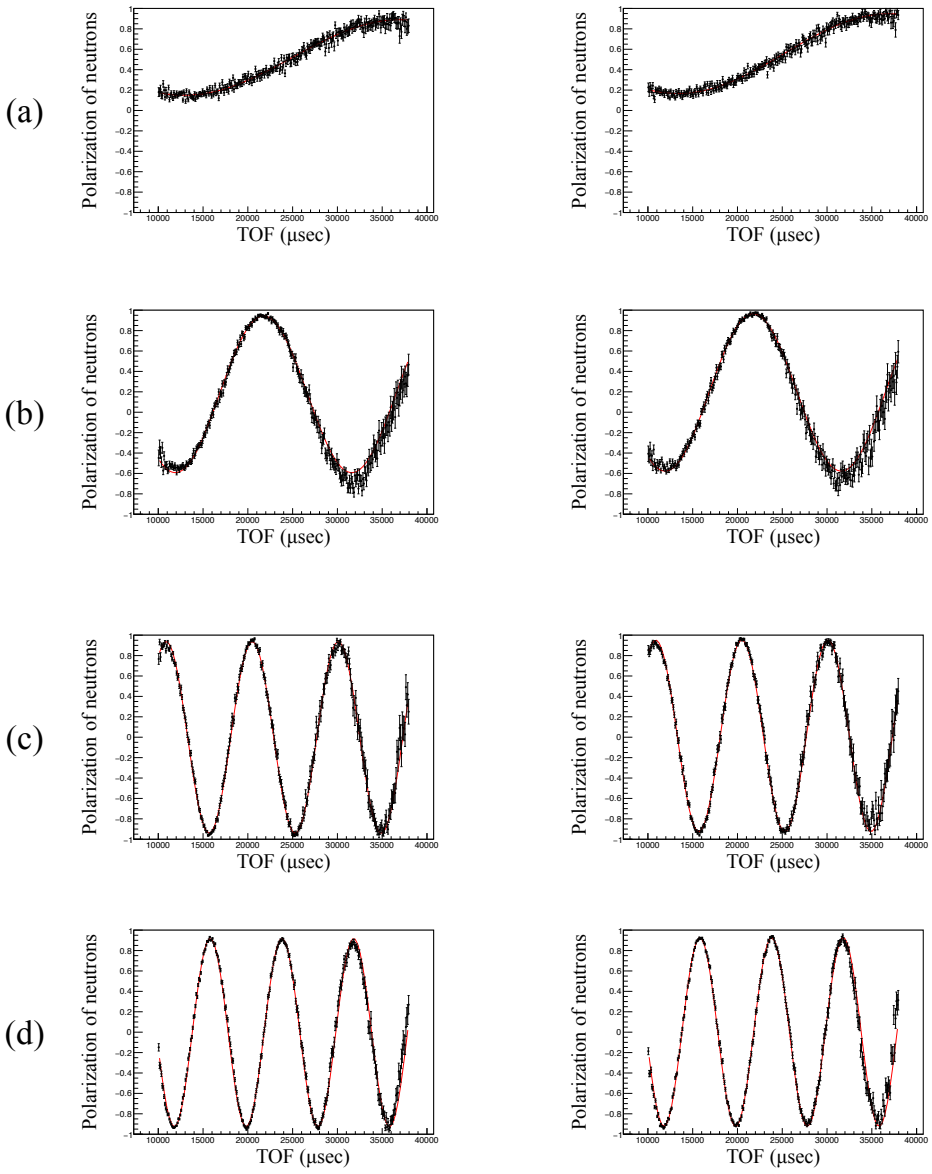

Figure 7.3: TOF spectra of neutron polarization passed through the solenoid coil using the pulsed neutron beam.

The four spectra on the left and four spectra on the right show the cases where the direction of the incident spin is parallel and antiparallel to the beam direction, respectively. (a), (b), (c), and (d) show the spectra at solenoid magnetic fields of 1.0, 2.5, 5.0, and 7.0 Gauss, respectively. Since the spin rotation is proportional to the time it takes to pass through the crystal, the spectra oscillate as shown in the figure when the TOF, which is inversely proportional to the neutron velocity, is taken as the horizontal axis. The stronger the magnetic field of the solenoid, the faster the rotation.

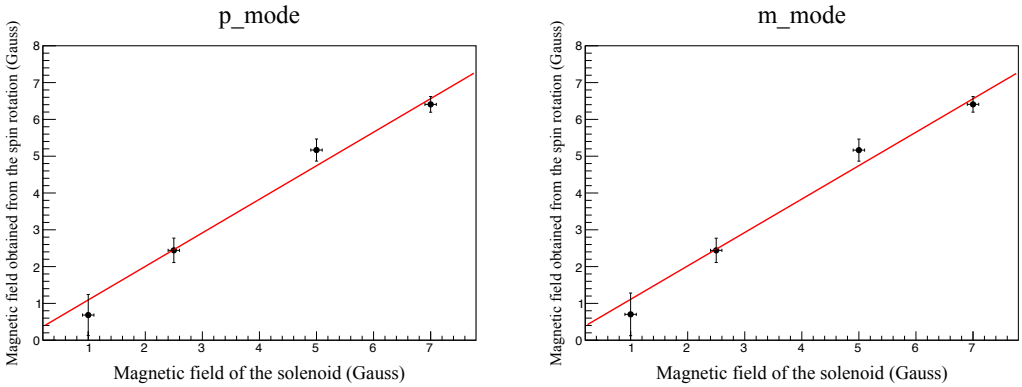

Figure 7.4: The magnetic field of solenoid coil obtained from the spin rotation.
The horizontal axis is the set value of the solenoid magnetic field measured by the gauss meter. The spin direction of incident neutrons is parallel to the beam direction on the left and antiparallel on the right.

The results are shown in Fig. 7.4. The vertical axis shows the magnitude of the solenoid magnetic field obtained from the spin rotation, and the horizontal axis is the set value of the solenoid magnetic field. It was confirmed that the solenoid magnetic field calculated from the measured spin rotation is in good agreement with the set magnetic field. In the low-field region, the deviation from the set value is relatively large. This is considered to be due to the effect of the external magnetic field. At 3 Gauss, which is the typical strength of the relativistic magnetic field in the crystal in this experiment, the systematic experimental uncertainty in this experimental system can be estimated to be within ± 0.65 Gauss.

7.4 Results of (110)-Plane with $\Delta\phi_g \neq 0$ in the Symmetric Laue Configuration

Spin rotation was measured at five tilt angles: 0°, 30°, -45°, 47.5°, and 37.5°. Figure 7.5 shows the TOF (Time of Flight) spectra at each tilt angle. The left spectra in the figure show the full TOF range from 10000 to 38100 μsec, and the right spectra show the extended TOF range from 11000 to 13000 μsec. The peak around 11700 μsec is the diffraction peak of the (110)-plane. The TOF of the (110)-plane, which is the symmetric Laue configuration, remains almost the same even when the tilt angle is changed. In fact, there is a slight shift due to an error in the Bragg angle setting. On the other hand, the peaks from other crystal planes shift, disappear, or appear when the tilt angle is changed. This is because these planes are in asymmetric Laue configuration or Bragg configuration.

The analysis was performed on the (110)-plane with $\Delta\phi_g \neq 0$ and the $(0\bar{2}1)$-, (011)-, and $(11\bar{1})$-planes with $\Delta\phi_g = 0$. In this section the analysis and result of the (110)-plane will be discussed, and in the next section the other asymmetric planes will be discussed.

7.4.1 Evaluation of the Diffraction Intensity

Figure 7.6 shows the TOF spectrum of the tilt angle of 0° by measurement mode, for the typical example. Since the measurement is performed in four modes (pp, mm, pm, and mp), four TOF spectra are obtained as shown in (a) of the figure. The TOF spectra of each mode are shown separately in (c): pp mode, (d): pm mode, (e): mm mode, and (f): mp mode. (b) is the sum of the four modes. The exact peak position was obtained from the TOF spectrum of the sum of the four modes of measurement to improve statistics (see Fig. 7.5). The following fit function with Extreme function and linear function was used for decision of the peak position [52];

$$f = F_0 \exp\left[-\exp\left(-\frac{x-F_1}{F_2}\right) - \frac{x-F_1}{F_2}\right] + F_3(x-x_0) + F_4, \tag{7.8}$$

where $F_0 - F_4$ are fit parameters, and F_1 is the peak position. The peak intensity was calculated by the sum of counts in the range of -100 μs and $+264$ μs in TOF with respect to the fitted peak position.

As for the background, diffraction peaks from crystal planes other than (110) migrate and appear at different positions near the (110)-peak by each tilt angle, so it is necessary to identify their positions and evaluate them so that they are not included. Fig. 7.7 shows the TOF spectrum at the tilt angle of 37.5°. In this case, diffraction peaks of $(0\bar{3}1), (11\bar{2}), (\bar{1}01), (\bar{1}30), (1\bar{3}2)$ appear other than (110)-peak between 11000 μs and 13000 μs in TOF. Since the background is considered to be almost constant in this range, we evaluated the background as the average of all the areas excluding these diffraction peaks. Then, the background was subtracted from the intensity of the earlier peak intensity to obtain the diffraction intensity. Assuming that the diffraction intensities for each of the four modes of measurement, pp, pm, mm and mp, are $N^{\mathrm{pp}}, N^{\mathrm{pm}}, N^{\mathrm{mm}}$ and N^{mp}, respectively, the polarization of the p-mode ($P^{\mathrm{p}}_{\mathrm{obs}}$) and the polarization of m-mode ($P^{\mathrm{m}}_{\mathrm{obs}}$) are as follows:

$$P^{\mathrm{p}}_{\mathrm{obs}} = \frac{N^{\mathrm{pp}} - N^{\mathrm{pm}}}{N^{\mathrm{pp}} + N^{\mathrm{pm}}}, \tag{7.9}$$

$$P^{\mathrm{m}}_{\mathrm{obs}} = \frac{N^{\mathrm{mm}} - N^{\mathrm{mp}}}{N^{\mathrm{mm}} + N^{\mathrm{mp}}}, \tag{7.10}$$

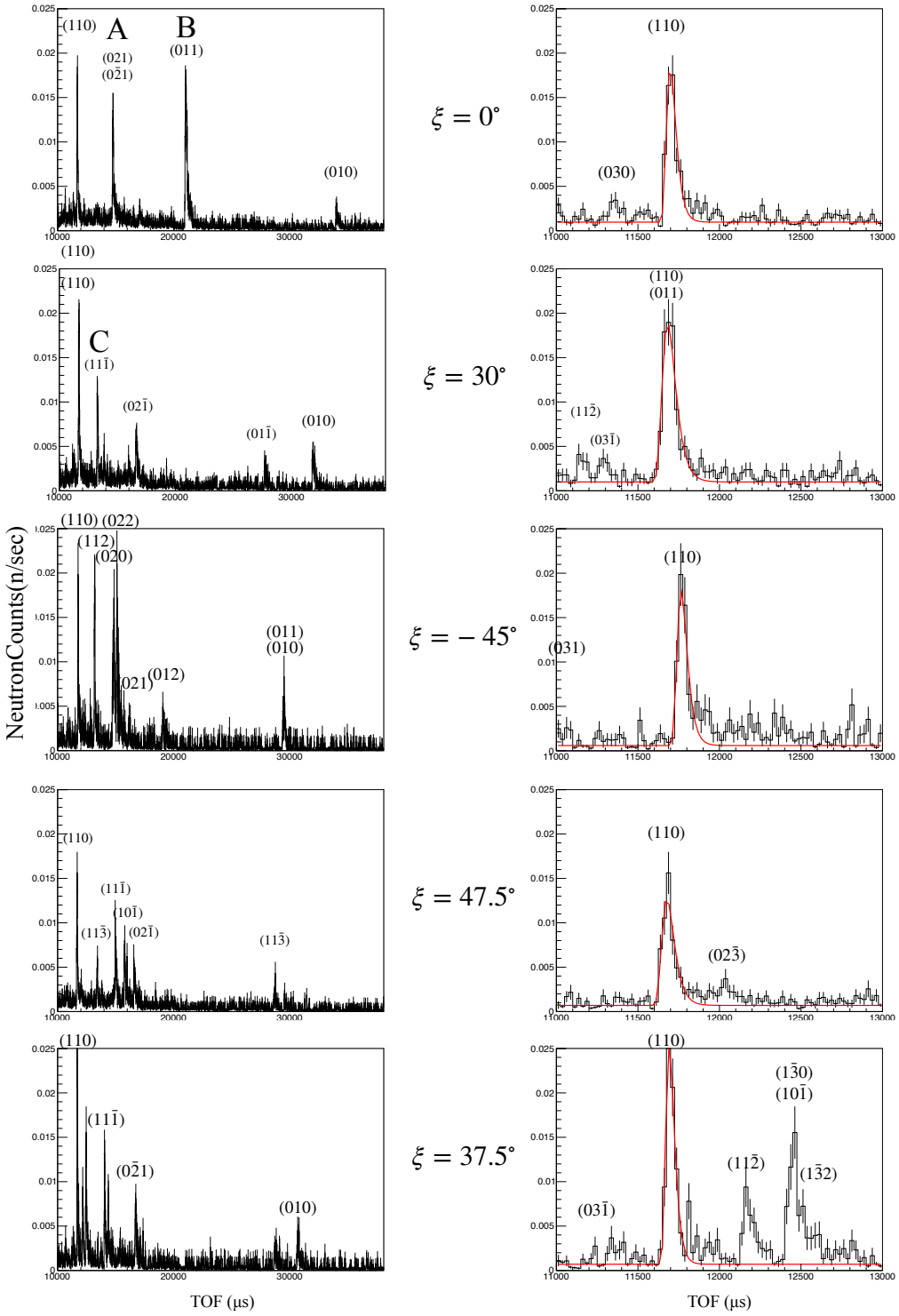

Figure 7.5: TOF spectrum at each tilt angle with the bin width of 25 μsec:
The left spectra in the figure show the entire TOF range from 10000 to 38100 μsec, and the right spectra show the expanded TOF range from 11000 to 13000 μsec. The peak around 11700 μsec is the diffraction peak of the (110)-plane. A, B, and C show the diffraction peaks of the crystal planes, $(0\bar{2}1)$, (011), and $(11\bar{1})$, respectively, in the asymmetric Laue configuration with $\Delta\phi_g = 0$, which will be analyzed in Section 7.5. The red curve is the result of the peak fit by Eq. (7.8)

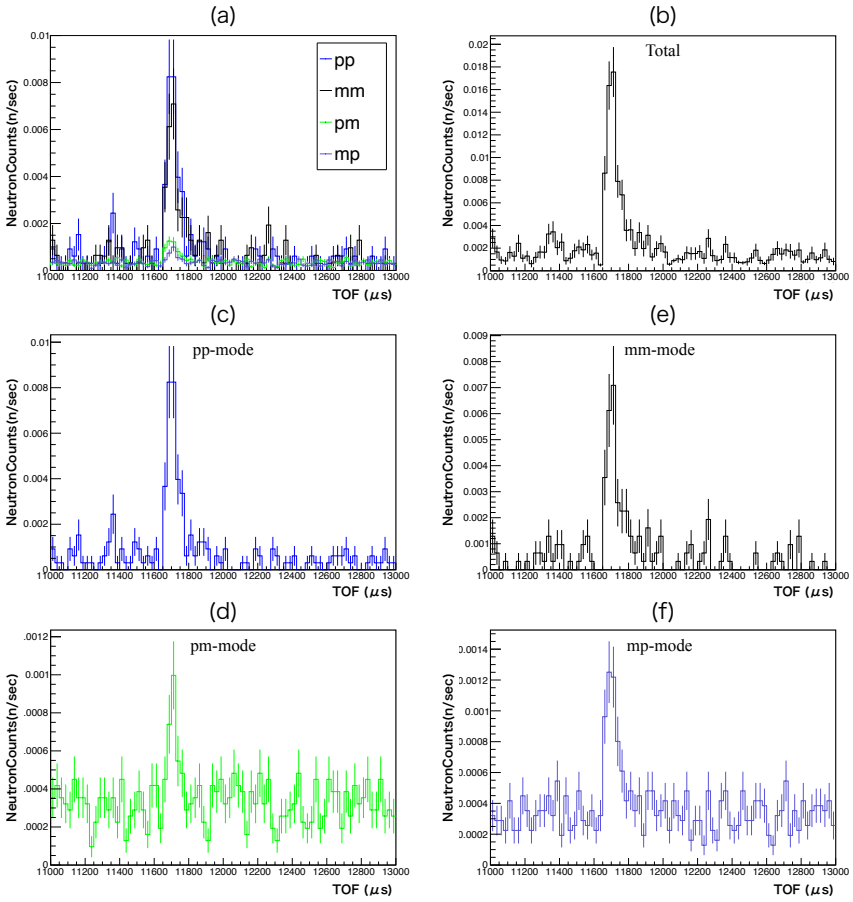

Figure 7.6: TOF spectrum of the tilt angle of 0 degrees for each measurement with the bin width of 25 μsec:
As a representative example, the TOF spectra at the tilt angle of 0 degrees are shown. (a) is the TOF spectrum measured in four measurement modes. (c),(d),(e), and (f) are shown separately for each measurement mode. These TOF spectra are used to evaluate peak intensity and background. (b) is the sum of the four measurement modes and is used to accurately determine the peak position.

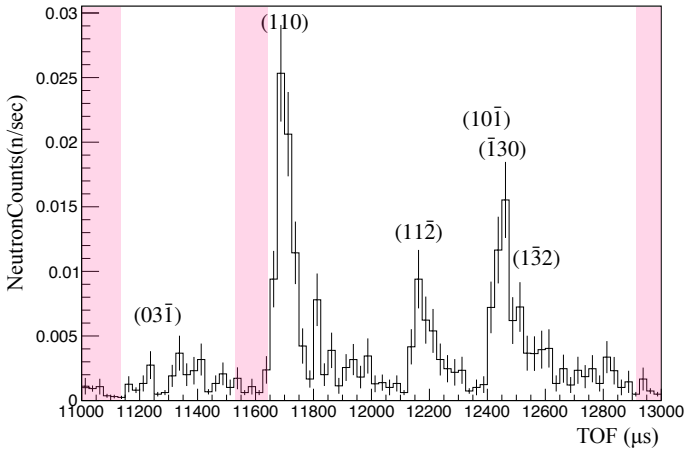

Figure 7.7: TOF spectrum at tilt angle of 37.5 degrees for evaluation of the background:
5 peaks other than (110) appear in the range of 11,000μs to 13,000μs. The background was estimated from the portion of the spectrum that excluded all of these peak regions (They correspond to the bands of pink color).

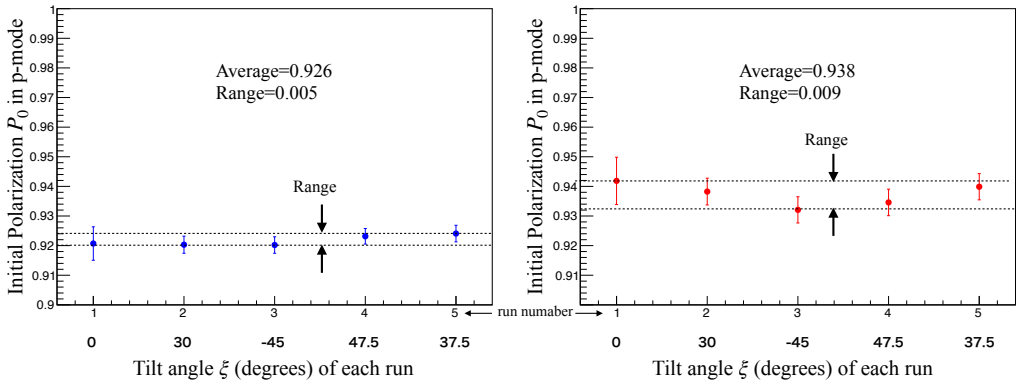

Figure 7.8: Initial polarization by the tilt angle and the measurement mode:
The plots shows the initial polarization for each tilt angle. The left side shows the initial polarization for the p-mode measurement, and the right side shows the initial polarization for the m-mode measurement. In the analysis of the spin rotation, the initial polarization for each tilt angle was used. The range of the changes over time were evaluated as the systematic uncertainty.

7.4.2 Initial Polarization

The initial polarization was measured immediately after the spin rotation measurement at each tilt angle, with the incident angle $\theta = 0^\circ$. The initial polarization value immediately after this tilt angle measurement was used in the calculation of Eq. (7.7). The method of measuring and calculating of the polarizations is the same as in the previous section. The results of the initial polarization at each tilt angle are shown in Fig. 7.8. The initial polarization of the m-mode is about 0.01 higher than that of the p-mode. This is considered to be an instrumental feature of the experimental line. Therefore, we decided to analyze the p-mode and m-mode separately and finally take the average of both. For each tilt angle, the initial polarization values vary in the range of 0.005 for the p-mode and 0.009 for the m-mode. Since this is above the statistical uncertainty, we decided to treat it as a systematic uncertainty. The larger of the two ranges, 0.009, was assumed to be equal to 2σ of the systematic uncertainty.

7.4.3 Spin Rotation

Figure 7.9 plots the relationship between P_{obs}/P_0 and tilt angle γ obtained in the previous two sections. P_{obs}/P_0 at each tilt angle is the average of the p-mode and m-mode at that tilt angle. Five tilt angles were measured, but as can be seen in Fig. 7.5, the diffraction peaks of the (110)-plane and (011)-plane overlap at a tilt angle of 30°, so they were excluded from the plot. The curves in the figure are the result of fitting based on Eq. (7.7). From this result, the spin rotation of the (110)-plane in a 10 mm thick α-quartz was obtained as follows;

$$\varphi^{\mathrm{obs}}_{(110)} = 0.45 \pm 0.03.$$

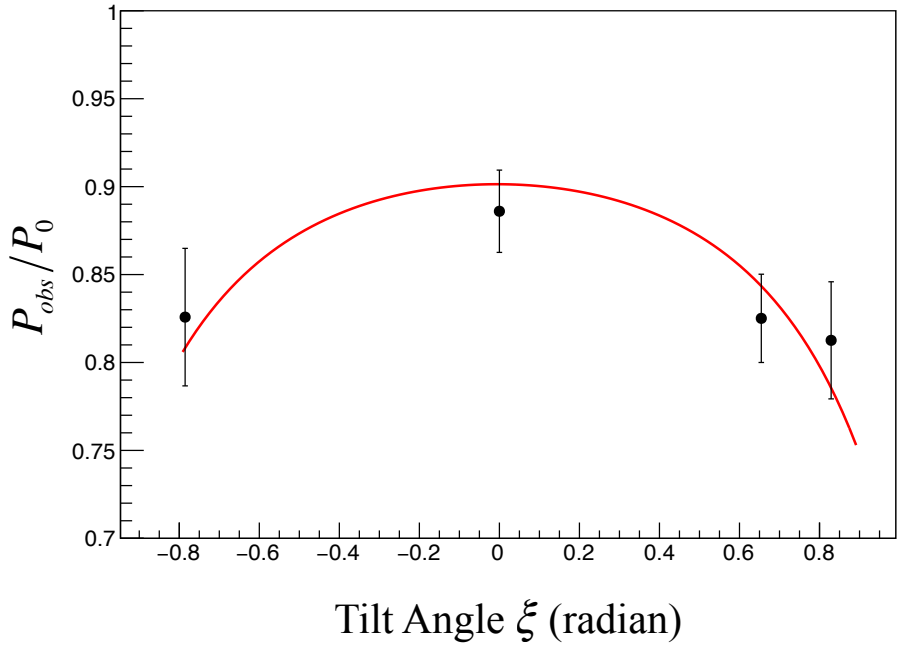

Figure 7.9: The relationship of $P_{\rm obs}/P_0$ and the tilt angle γ.
$P_{\rm obs}/P_0$ at each tilt angle is the average of p-mode and m-mode at the tilt angle. The data at the tilt angle of 30° was excluded from the plot, because the diffraction peaks of (110)- and (011)-plane overlap. The red curve shows the result of the fit by Eq. (7.7).

7.4.4 Compensation for External Magnetic Field

In the experiment, no magnetic shielding was used. Therefore, there is an external magnetic field inside the crystal, and the spin performs precessional rotation around the composite field of the relativistic and external magnetic fields. Therefore, it is necessary to compensate for this. If the unit vectors of composition of the relativistic magnetic field and external magnetic field for α- and β-waves are expressed as $\boldsymbol{n}^\alpha = (n_x^\alpha, n_y^\alpha . n_z^\alpha)$ and $\boldsymbol{n}^\beta = (n_x^\beta, n_y^\beta, n_z^\beta)$, respectively, the amount of spin rotation including the effect of the external magnetic field is given by

$$P = \frac{1}{2}\left\{\cos\varphi_{\rm c}^\alpha + \cos\varphi_{\rm c}^\beta + 2\left[(n_x^\alpha)^2\sin^2\left(\frac{\varphi_{\rm c}^\alpha}{2}\right) + (n_x^\beta)^2\sin^2\left(\frac{\varphi_{\rm c}^\beta}{2}\right)\right]\right\}, \tag{7.11}$$

where $\varphi_{\rm c}^\alpha$ and $\varphi_{\rm c}^\beta$ is the spin rotation angle by the composite magnetic field of α- and β-wave, respectively. The external magnetic field was measured with a Gauss meter at the position of 6 mm in front and behind the crystal, respectively. The result was linearly interpolated into the crystal and the magnetic field inside the crystal was estimated as (0.3. 0.65, -0.1) Gauss at the center of the crystal. Incidentally, the magnitude of the relativistic magnetic field is about 3 Gauss, assuming an intra-crystal electric field of 2.0×10^8 V/cm. The spin rotation due to only the relativistic magnetic field after the compensation of the external magnetic field is as follows,

$$\varphi_{(110)} = 0.44 \pm 0.03.$$

Here, the external magnetic field inside the crystal was estimated by linear interpolation at the center of the crystal and it is assumed to be constant. So the range of the external magnetic field of the two-point measurements should be accounted for as the systematic uncertainty.

7.4.5 Summary of the Statistical and Systematic Uncertainties

Statistical and systematic uncertainties of the spin rotation of (110)-plane are summarized in Table 7.2.

Table 7.2: Summary of the statistical and systematic uncertainties of the spin rotation of (110)-plane.
*This uncertainty is based on the initial polarization with crystal and without crystal at another experiment.

Items	Details	Uncertainties of spin rotation
Statistic Uncertainty		± 0.03
Systematic Uncertainties		
	Initial Polarization	± 0.003
	External Magnetic Field	± 0.001
	Crystal*	$+0.001, -0$
	Thickness of Crystal	± 0.0002(neglegible)
	Experimental system	± 0.078
	Total	$+0.083, -0.082$

The spin rotation of neutrons in dynamical diffraction on the (110)-plane of α-quartz with the thickness of 10 mm, was obtained as

$$\varphi_{(110)} = 0.44 \pm 0.03^{\text{stat}} \pm 0.08^{\text{syst}}. \tag{7.12}$$

The effective intra-crystal electric field obtained from this spin rotation by Eq. (7.1) is as follows,

$$E_{(110)} = (2.2 \pm 0.2^{\text{stat}} \pm 0.5^{\text{syst}}) \times 10^8 \text{ V/cm}. \tag{7.13}$$

This value is consistent with the values obtained by phase contrast measurements and similar spin rotation measurements [32, 33, 53], and is also in good agreement with the early calculations by V. V. Voronin and et al. [32, 54].

7.5 Results of Other Crystal Planes with $\Delta\phi_g = 0$ in the Asymmetric Laue Configuration

In our experiment, we used a white beam by the pulsed neutron source to examine the transmission diffraction peaks, which allows us to simultaneously detect diffraction peaks from several crystal planes in the asymmetric Laue configuration other than (110)-plane. Therefore, crystal planes in the asymmetric Laue configuration with $\Delta\phi_g = 0$, other than the (110)-plane, can be analyzed simultaneously. However, the actual planes and tilt angles that can be analyzed are limited because the diffraction peaks of these crystal planes shift, disappear, or appear when the tilt angle is changed, as can be seen in Fig. 7.5. Among the many diffraction peaks detected at each tilt angle, the $(0\bar{2}1)$-plane at the tilt angle of 0° (diffraction peak A in Fig. 7.5), the (011)-plane at the tilt angle of 0° (diffraction peak B in Fig. 7.5) and the $(11\bar{1})$-plane at the tilt angle of 30° (diffraction peak C in Fig. 7.5) could be analyzed. Since the spin rotation of them was obtained only at a specific tilt angle, the spin rotation of these crystal planes could not be obtained from the thickness dependence as (110)-plane.

Figure 7.10 shows the TOF spectra of the diffraction peaks from the $(0\bar{2}1)$-, (011)- and $(11\bar{1})$- planes. In (a), the diffraction peak of the $(0\bar{2}1)$-plane almost overlap with that of the (021)-plane. Since the crystal structure factors F_g of the $(0\bar{2}1)$- and (021)-planes are 20.818 and 7.3138, respectively, and so the diffraction intensity of $(0\bar{2}1)$-plane is about three times that of the (021)-plane, we decided to consider the spin rotation in diffraction peak collectively, considering that the $(0\bar{2}1)$-plane is the dominant influence. Of course, strictly speaking, the following result for the $(0\bar{2}1)$ plane is a combined effect of the $(0\bar{2}1)$ and (021) planes.

The diffraction peak of the (011)-plane in (b) is slightly shifted and overlapped by the peak of the (011)-plane. This is because the coordinate system of the incident crystal plane and the beam axis is slightly tilted, although they should overlap perfectly in a perfectly symmetric Laue configuration. This is because the (011)-plane is on the long wavelength (high TOF) side, and the shift is magnified. The influence of the $(01\bar{1})$ plane can be removed by shortening the integration range of the diffraction peak of the (011) plane on the tail side.

The diffraction peak of the $(11\bar{1})$-plane in (c) could be treated as a single peak because it is completely separated from the adjacent peak of the $(1\bar{3}1)$-plane. The respective diffraction peak integration ranges are shown in Fig. 7.10.

The analysis method is the same as for (110)-plane in Section 7.4. The results of the analysis are summarized in TableTable 7.3.

Table 7.3: Summary of results for other planes with asymmetric Laue configuration:

Item	$(0\bar{2}1)$	(011)	$(11\bar{1})$
P_{obs}/P_0	0.95 ± 0.02	0.99 ± 0.01	0.88 ± 0.04
φ	0.30 ± 0.07	0.14 ± 0.07	0.49 ± 0.08
φ after compensation	0.29 ± 0.07	0.11 ± 0.05	0.48 ± 0.08

The results of the spin rotation of these asymmetric planes containing the systematic uncertainty were as follows:

$$\varphi_{(0\bar{2}1)} = 0.29 \pm 0.07^{\mathrm{stat}} \pm 0.12^{\mathrm{syst}}, \tag{7.14}$$

$$\varphi_{(011)} = 0.11 \pm 0.05^{\mathrm{stat}} \pm 0.21^{\mathrm{syst}}, \tag{7.15}$$

$$\varphi_{(11\bar{1})} = 0.48 \pm 0.08^{\mathrm{stat}} \pm 0.11^{\mathrm{syst}}. \tag{7.16}$$

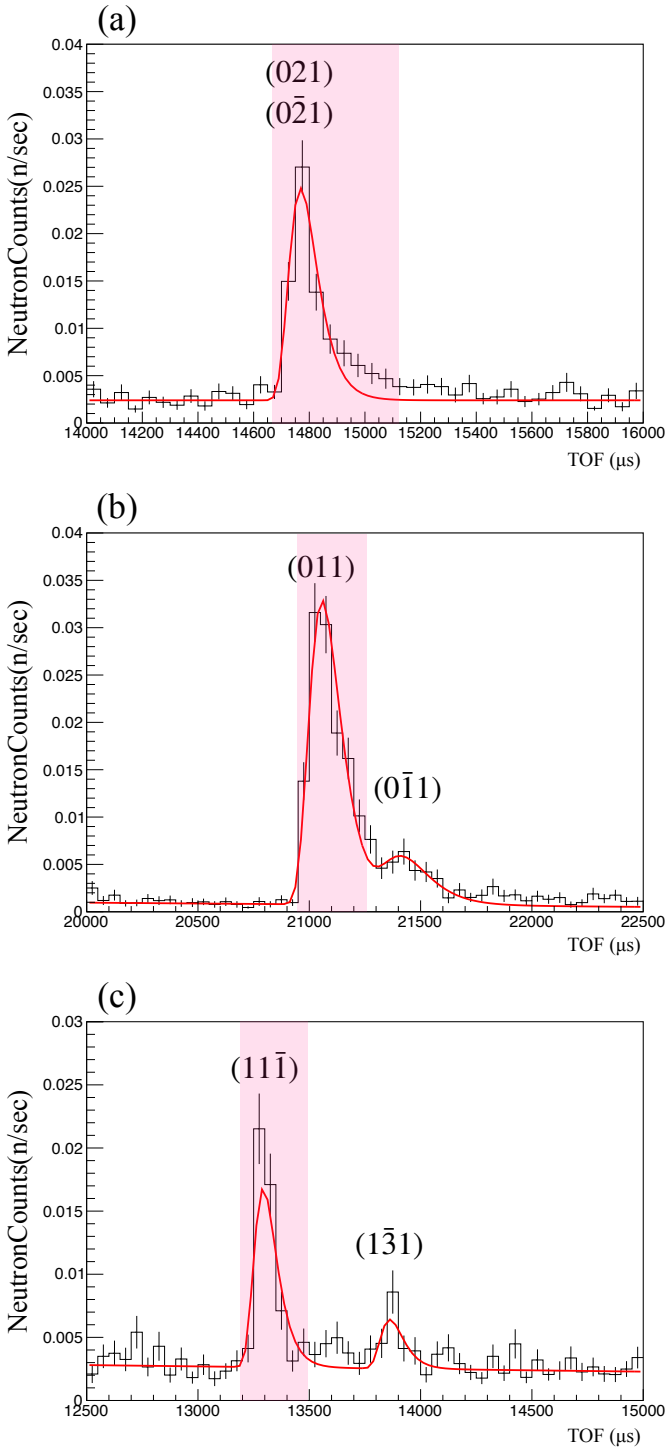

Figure 7.10: TOF spectra of diffraction peak of $(0\bar{2}1)$-, (011)- and $(11\bar{1})$-planes;
(a), (b) and (c) show the TOF spectra of the diffraction peaks from the $(0\bar{2}1)$-, (011)- and $(11\bar{1})$-planes, respectively. The $(0\bar{2}1)$ peak is almost completely overlapped by the (021) peak. A small peak of $(0\bar{1}1)$-plane overlaps the tail of the (011) peak. This can be excluded by narrowing the integration range of the peak. The peak of $(11\bar{1})$ is a single peak. The red areas in the figure indicate the respective integration ranges.

The effective intra-crystal electric field obtained from these spin rotations by Eq. (7.1) is as follows;

$$E^{\mathrm{eff}}_{(0\bar{2}1)} = (1.4 \pm 0.3^{\mathrm{stat}} \pm 0.6^{\mathrm{syst}}) \times 10^8 \mathrm{V/cm}, \tag{7.17}$$

$$E^{\mathrm{eff}}_{(011)} = (0.5 \pm 0.3^{\mathrm{stat}} \pm 1.0^{\mathrm{syst}}) \times 10^8 \mathrm{V/cm}, \tag{7.18}$$

$$E^{\mathrm{eff}}_{(11\bar{1})} = (2.4 \pm 0.4^{\mathrm{stat}} \pm 0.5^{\mathrm{syst}}) \times 10^8 \mathrm{V/cm}. \tag{7.19}$$

The spin rotations and the effective intra-crystal electric fields of these crystal planes, $(0\bar{2}1)$, (021), (011) and $(11\bar{1})$, are expected to be zero in the previous calculations because of $\Delta\phi_g = 0$ [54]. In this experiment, the spin rotation of (011)-plane is consistent to zero and consistent with the calculation assuming $\Delta\phi_g = 0$. However, there is a significant deviation from zero on $(0\bar{2}1)$- and $(11\bar{1})$-planes, nevertheless $\Delta\phi_g = 0$. The statistic and systematic uncertainties in the result (011) are larger than the others. This is because the experiment was carried out at an initial polarization close to 1. The propagation of the uncertainty is proportional to $\sin^{-1}(\varphi_{\mathrm{S}})$ when converting from the polarization to the spin rotation angle. For decreasing this uncertainty, it needs to carry out the experiment near an initial polarization of 0.

We know no experimental measurements to date that have measured the effective intra-crystal electric fields or the spin rotations for these crystal planes in the symmetric as well as asymmetric Laue configurations. In this experiment, the significant spin rotations were measured for these $(0\bar{2}1)$- and $(11\bar{1})$-planes with $\Delta\phi_g = 0$. Although this is still one experimental result and further follow-up tests are needed, this result indicates that an effective intra-crystal electric field may exist even on a crystal plane with $\Delta\phi_g = 0$. This could be the effect of the interference terms 13–16 in Table 6.1, which have been ignored so far.

7.6 Discussion of the Intra-crystal Electric Field

In this experiment, we obtained two experimental results on the effective intra-crystal electric field. One is that for the (110)-plane, for which an effective intra-crystal electric field has been considered to exist at $\Delta\phi_g \neq 0$ and has actually been measured, we obtained results that are consistent with previous measurement and calculation results. On the other hand, non-zero spin rotation was measured in the $(0\bar{2}1)$, (011) and $(11\bar{1})$-planes, which have not been measured so far but are theoretically considered to have no effective intra-crystal electric field because $\Delta\phi_g = 0$, and results were obtained as if an effective intra-crystal electric field existed. The following possibilities as possible causes.

(1) Influence of magnetic scattering due to magnetic impurities in a crystal.
Since no difference was observed in the direct beam polarization measurements with and without the crystal, the effect is considered to be small.

(2) Influence of depolarization due to thermal diffuse scattering.
The Debye-Waller factor $\exp(-W_d)$ is about 0.95–0.98, and the solid angle of the detector is small, less than 0.2 mradian, so the effect is negligible.

(3) The effect of the interference terms 13–16.
If the pendellösung interference is partially broken, oscillating components that should be cancel each other may remain uncanceled. In such a case, the interference terms 13–16 cannot be neglected and an effective intra-crystal electric field may be generated even at $\Delta\phi_g = 0$.

We believe that these spin rotations observed at the crystal planes with $\Delta\phi_g = 0$ are most likely the effect of the interference terms 13–16, which was considered negligible so far.

If this is the case, then there should also be an effect of this in the (110)-plane, which raises the question of whether there is a contradiction. Theoretical calculations of the effective intra-crystal electric field for the (110)-plane are specifically discussed in the Ref. [32] and [54]. [32] and [54], but the values are slightly different. Here, $v_g^{\mathrm{E}} = 1.92$ V and $\Delta\phi_g = -0.42$ are assumed from Ref. [54]. The space of lattice planes is $d_g = 2.4569$ Å. We have already mentioned that the 9 and 10 terms in Table 6.1 represent α-wave and the 11 and 12 terms represent β-wave. Similarly, the wave represented by the 13 and 16 terms is called λ-wave and that by the 14 and 15 terms is called η-wave. In the symmetric Laue configuration, the intensity ratio of the λ-and η-waves is $1/2 : 1/2$, as is the ratio of the α-and β-waves. As mentioned earlier, the λ-and η-waves have a Pendellösung oscilation component in their factor, so they cancel each other when integrated in the crystal thickness direction. However, in real crystals, it may assumed that they can not cancel each other completely due to some crystal defects at the order of the Pendellösung length and a certain component remains. If the ratio is R, the effective intra-crystal electric fields of α-wave, β-wave, λ-wave and η-wave are calculated as follows;

$$E_{(110)}^{\mathrm{eff}-\alpha} = -v_g^{\mathrm{E}} \boldsymbol{g} \sin\Delta\phi_g, \tag{7.20}$$

$$E_{(110)}^{\mathrm{eff}-\beta} = v_g^{\mathrm{E}} \boldsymbol{g} \sin\Delta\phi_g, \tag{7.21}$$

$$E_{(110)}^{\mathrm{eff}-\lambda} = v_g^{\mathrm{E}} \boldsymbol{g} R \left(\sin\Delta\phi_g + \cos\Delta\phi_g\right), \tag{7.22}$$

$$E_{(110)}^{\mathrm{eff}-\eta} = -v_g^{\mathrm{E}} \boldsymbol{g} R \left(\sin\Delta\phi_g - \cos\Delta\phi_g\right). \tag{7.23}$$

A schematic diagram of the spin rotation is shown in Fig. 7.11 (a), where P_0 indicates the initial polarization state, $P_0 = 1$. The spin rotation angles due to the effective intra-crystal electric field sensed by the α, β, λ and η-waves are noted as ϕ_α, ϕ_β, ϕ_λ and ϕ_η, respectively. First, half of the wave rotates ϕ_α, then the half of it rotates ϕ_λ and the other half rotates ϕ_η, then the polarization states are P1 and P2, respectively. On the other hand, the half that rotates ϕ_β in the opposite direction of ϕ_α also rotates ϕ_λ and ϕ_η to become P3 and P4, respectively. The rotation angles are given by Eq. (7.1). The intensities of P_1, P_2, P_3 and P_4 are equal to 1/4 each. The observed total polarization is given by $(P_1 + P_2 + P_3 + P_4)/4$ and can be obtained as follows using Eqs. (7.20)–(7.23),

$$P_{\mathrm{obs}} = \frac{1}{2}\cos(\phi_\alpha)\left[\cos(\phi_\lambda) + \cos(\phi_\eta)\right], \tag{7.24}$$

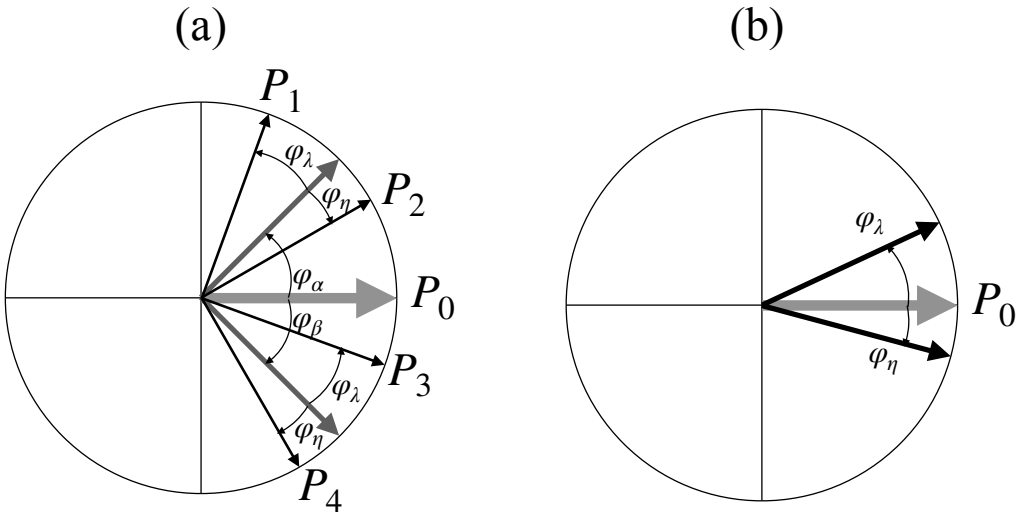

Figure 7.11: Spin rotation of four waves, α, β, λ and η;
Schematic representation of the spin rotation due to the effective intra-crystal electric field sensed by the four interference waves, α, β, λ and η.
(a) The case of $\Delta\phi_g \neq 0$, the (110) plane, and $R \neq 0$ is shown. From the initial polarization ratio $P_0 = 1$, first, one half of the wave rotates by ϕ_α and the other half of the wave rotates by ϕ_β in the opposite direction. They also rotate by half, by ϕ_λ and ϕ_η, and become to four polarization states, P_1, P_2, P_3 and P_4. These four states have the same intensity, and the total polarization is obtained by averaging them.
(b) The case of $\Delta\phi = 0$ and $R \neq 0$ is shown. In this case, the effective intra-crystal electric field sensed by the α- and β-waves is zero, and the spin rotation of the λ- and η-waves is observed as it is.

where ϕ_α can be replaced by ϕ_β.

Figure 7.12 shows the relationship between the uncanceled fraction R and the intra-crystal electric field obtained from the resulting spin rotation for the crystal thickness of 10 mm. The value at $R = 0$ is the intra-crystal electric field when only α- and β-waves are considered, which in this case is 2.0×10^8 V/cm. The blue line and band in the figure show the result of this experiment. When $R < 0.3$ or so, the influence of the λ-wave and η-wave is within the uncertainty of this experiment and does not cause any contradiction. This is because the rotation of the λ- and η-waves is in the direction that they cancel each other out around the spin rotation of the α- and β-waves, respectively. However, they do not completely cancel each other out. For reference, the red line shows the case where the spin rotation of the α- and β-waves is $\pi/2$. In this case, the effect of R cancels out completely and the observed effective intra-crystal electric field is 2.0×10^8 V/cm for the α- and β-waves, which is independent of R.

On the other hand, when $\Delta\phi_g = 0$, as shown in Fig. 7.12 (b), the $\sin\Delta\phi_g$ term in Eqs. (7.20)–(7.23) becomes zero, so there is no spin rotation of the α- and β-waves, but only of the λ- and η-waves, which appear as spin rotation as they are, and this can be observed. Thus, by observing the spin rotation in the crystal plane with $\Delta\phi_g = 0$, it may be possible to evaluate the value of R, i.e., the imperfection of the crystal.

In Fig. 7.12, the closer the value of R approaches 1, i.e., the larger the crystal imperfection, the stronger the effective intra-crystal electric field, which would appear to be advantageous for nEDM search experiments, but this is not the case. The spin rotation discussed here deals only with the amount of rotation on the $\boldsymbol{xy}$-plane, but in reality, there are likely to be fluctuations in the $\boldsymbol{z}$-direction. In the case of spin rotation on the $\boldsymbol{xy}$-plane, these are expected to cancel out or be negligible. In the nEDM search experiments, however, such fluctuations cannot be neglected because the problem is the spin polarization in the $\boldsymbol{z}$ direction. Therefore, it is necessary to keep the value of R as close to zero as possible and to quantitatively estimate the effect on the $\boldsymbol{z}$-directional polarization for the nEDM search experiment using the crystal diffraction.

This argument is currently hypothetical and experimental results are not yet satisfactory, so further experimental verification and theoretical considerations are needed. However, it has the possibility to provide a new indicator for the investigation of crystal imperfections, and a clue for the investigation of systematic

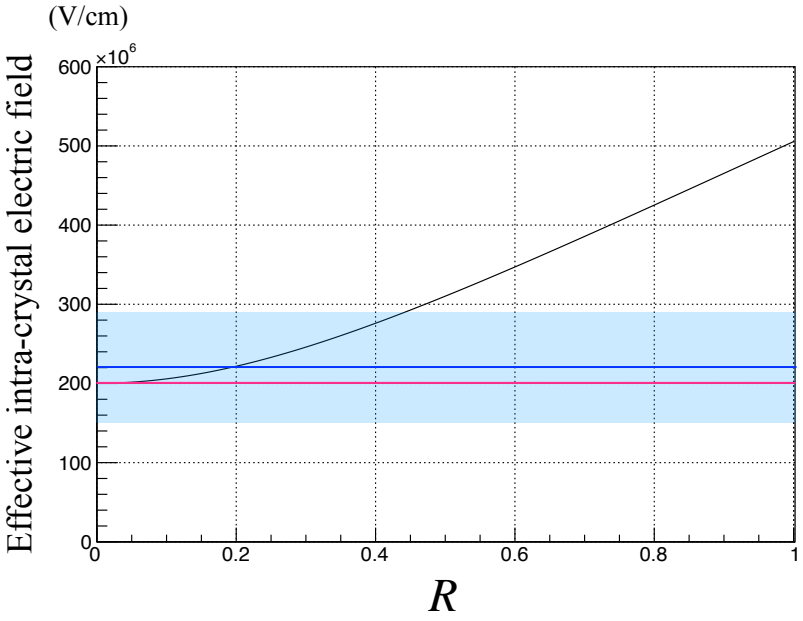

Figure 7.12: The effect of the effective intra-crystal electric field due to λ- and η-waves;
The relationship between the index R, which is considered to represent crystal imperfections, and the effective intra-crystal electric field observed at that time is shown in the black line for the (110)-plane of α-quartz, $u_g^{\mathrm{E}} = 1.92$ V, $\Delta\phi_g = -0.42$, and the crystal thickness is 10 mm. $R = 0$ indicates the effective intra-crystal electric field of conventional α- and β-waves only, 2.0×10^8 V/cm. At this time, the effects of the λ- and η-waves are completely canceled out. The blue line and band show the results of this experiment, which are consistent in the range $R < 0.3$. The red line is for a crystal thickness of 38.5 mm. In this case, the amount of rotation of the α- and β-waves is $\pi/2$, and the observed effective intra-crystal electric field ibecomes independent of R, with a constant value of 2.0×10^8 V/cm. The spin rotation of the λ- and η-waves is not completely canceled, but rather does not appear in the observation.

uncertainties in nEDM search experiments using crystal diffraction.

We plan to verify the reproducibility as the first step to validate this hypothesis. By reworking the crystal used in this study, we will increase the crystal thickness by a factor of about 2.5 and increase the amount of spin rotation to improve the accuracy of the verification. In addition, we will measure the spin rotation of other crystal planes with $\Delta\phi_g = 0$. Theoretical calculations for crystal planes other than (110) are currently in progress. In the future, we will test this hypothesis using crystals of various crystalline qualities (including Si, Ge, and other centrosymmetric crystals).

8 Improvement of the Crystal Diffraction Method

In this section we would discuss the experimental methods and possibilities for nEDM search experiments using crystal diffraction. In Table 2.1 of Section 2.5, the three factors that determine the sensitivity of nEDM search experiments were characterized numerically. There, the crystal diffraction method requires an intra-crystal electric field of $\sim 10^8$ V/cm, an interaction time of ~ 1 msec, and statistics of $\sim 10^4$ counts per sec to achieve a sensitivity of $1 \times 10^{-26}\ e \cdot$cm while 100 days. We will discuss whether these numbers are achievable and how to achieve them. As shown in Section 6, for the intra-crystal electric field, it was already known that the target of 1×10^8 V/cm is achievable, and there may be the possibility of 1×10^9 V/cm for a specific crystal. In the following discussion, we assume 2×10^8 V/cm in the (110)-plane for SiO_2 crystal and 1×10^9 V/cm in the (532)-plane for $Bi_{12}GeO_{20}$ crystal. The latter has not yet been confirmed experimentally. The basic unit of the experiment to search for nEDM using crystal diffraction is shown in Fig. 8.1.

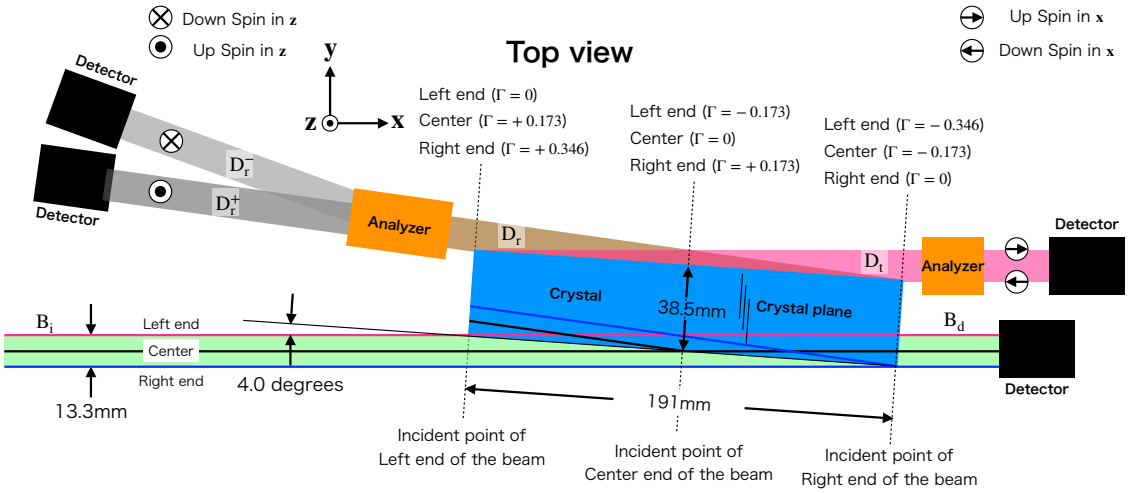

Figure 8.1: Basic unit for the experiment to search for nEDM by crystal diffraction:
A13.3 mm wide neutron beam B_i is injected onto a 191mm wide crystal, and the reflected and transmitted diffraction beams, D_r and D_t, respectively, are ejected from the ejection plane. The reflected beam is analyzed to the spin up and down state in z-direction and counted, respectively, to search for nEDM. The transmitted beam is analyzed to the spin up and down state in x-direction and are counted alternately to monitor the polarization of the spin in x-direction. B_d is the direct beam transmitted through the crystal and it is also monitored. The black line represents the center of the beam, the blue line represents the right end (looking downstream), and the red line represents the left end, respectively. In this case, the beam is propagated from each incident point into the Bormann fan with an apex angle of 172 degrees, and a portion of the beam is ejected from the ejection plane. The value of Γ of each ejected beam is noted in the figure.

In Fig. 8.1, the basic geometry is illustrated using the (110)-plane of α-quartz as an example. The crystal is positioned with a glancing angle η of 4 degrees with respect to the neutron beam. The relationship with the Bragg angle θ_B is $\theta_B = 90 - \eta$ (degrees). The reason for taking this small glancing angle is to increase the interaction time. In the case of the (110)-plane of α-quartz with the effective intra-crystal electric field of 2.0×10^8 V/cm, the thickness of the crystal, where the incident spin state becomes to $P = 0$ in the x-direction is fixed to 38.5 mm regardless of the neutron wavelength (see Eq. (4.22)). Since the thickness of the crystal is fixed, a small glancing angle is advantageous to increase the interaction time by decreasing the velocity of neutrons along the crystal plane. The optimum value of η is not determined only by it. It is also determined by taking into account the experimental apparatus conditions, etc., but this is not discussed here. In actual experiments, magnetic shields are placed around the crystal to shield it from external magnetic fields and other devices that will be described later, but these are also omitted. As one example, the size of the crystal that can accept all 13.3 mm beam width requires, in this case, a width of 191 mm as one example. The height is determined by the beam height, so if the beam height is 50 mm, the required α-quartz size is 191 mm wide, 50 mm high, and 38.5 mm thick. Neutrons incident on the crystal diffract and spread in

a wide Bormann fan with a vertex angle of 172 $^\circ$, as indicated by the line in the figure, and the reflected and transmitted diffraction beam are ejected from the ejection surface. Of the diffracted beam, the neutrons ejected from the ejection plane range from $\Gamma = -0.173$ to $+0.173$ at the beam center. This ratio is important for estimating the statistics of neutrons available for experiments In this case, the reflected diffraction beam is used to search for nEDM. It is analyzed to the spin up state and down state in z-direction and counted respectively. The transmitted diffraction beam is used to monitor the depolarizing condition in x-direction. It is analyzed to the spin up state and down state in x-direction and counted alternately. The direct beam through the crystal is also monitored to watch the beam condition.

8.1 The Possibility of Extending the Statistics by Multi-unit

One of the reasons for the low sensitivity of the crystal diffraction method is the statistics. Table 2.1 shows that the statistics of 10^4cps is required, but in fact this it is not achieved. The intensities obtained in dynamical diffraction of α-quartz in the Laue configuration are on the order of 0.1cps in the Pendellösung fringes experiment. Even under the geometric conditions of the basic unit shown in Fig.8.1, the neutron counts are estimated to be at most $\sim$ 100 cps, which is as low as 2 orders of magnitude.

The simple way to increase the statistics is to multiplex the basic unit. Figure 8.2 shows an example. Specifically, how the basic units are arranged and multiplexed should be decided by taking into account the beam and equipment environment. In the figure, four basic units are arranged in a mirror inversion. In the downstream unit, the intensity of the incident beam is reduced due to diffraction and absorption in the previous units. The reduction in beam intensity due to absorption is only about 70 % for α-quartz and 50 % for Bi12GeO$_2$0 in the last unit when the number of multiplexing units is set to 10, so it is sufficiently effective to use a multi-unit system. Furthermore, by using multi units, the wavelength of neutrons used by each stage can be changed. Since the conditions under which the incident spin state becomes the polarization of $P = 0$, do not change, only the nEDM effect increases in proportion to the neutron wavelength. This can be used to check the systematic uncertainties of the experiment.

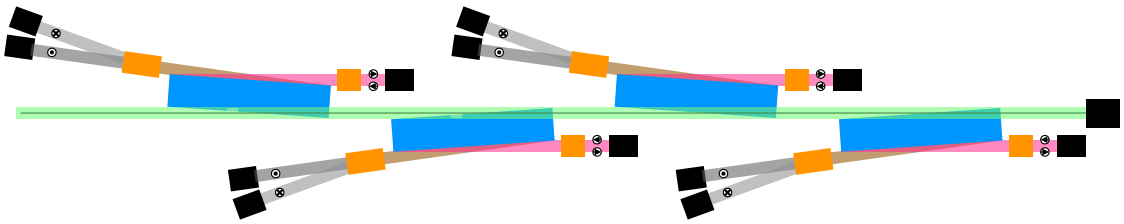

Figure 8.2: Schematic diagram of Multi-stage system:
Four basic units are arranged; the beam passing through the first stage passes directly through the second and third stages and enters the last stage; the second and fourth stages are mirrored with respect to the beam axis of the first and third stages.

8.2 The Possibility of Increasing of Interaction Time by Applying an External Magnetic Field inside a Crystal only

Second reason for the low sensitivity of the crystal diffraction method lies in the interaction time. As mentioned above, it was necessary that the spin polarization becomes to be $P = 0$ in the x-direction, when the nEDM measurement is performed. This condition give a limitation that determined the required crystal thickness and the interaction time.

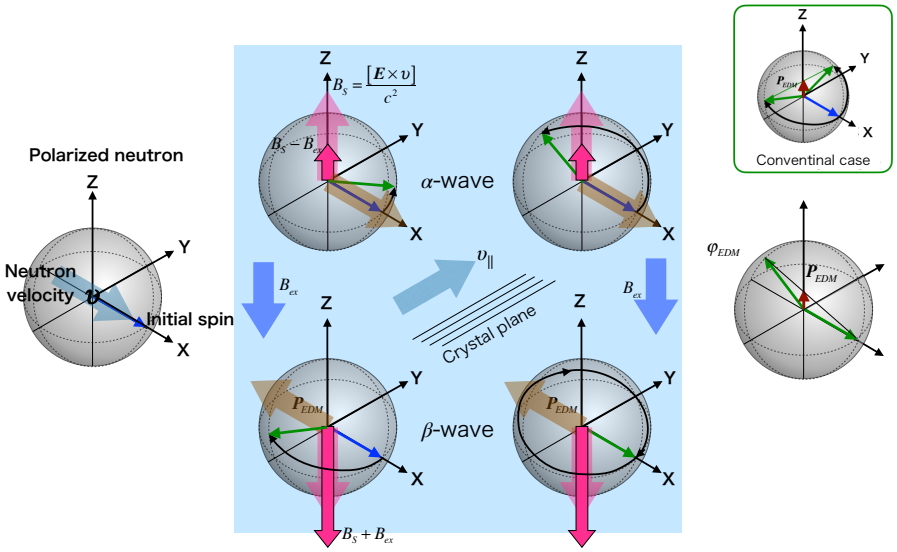

Figure 8.3: The external magnetic field application method:
An external magnetic field $\boldsymbol{B}_{\rm ex}$ is applied downwards (in this case in the same direction as the Schwinger field $\boldsymbol{B}_{\rm S}$ sensed by the β-wave) only inside the crystal (blue part). The solenoid generating $\boldsymbol{B}_{\rm ex}$ is omitted. The α-wave sense the combined magnetic field $(B_{\rm S}-B_{\rm ex})$ and precess, while the β-wave sense the combined magnetic field $(B_{\rm S}+B_{\rm ex})$ and precess in the opposite direction. The blue arrows represent the initial spin and the green arrows the state of the precessional rotation. The figure shows the case where $n=1$ $(\kappa=1/3)$ and the strength of the external magnetic field is 1/3 of the Schwinger magnetic field. α-wave precesses slowly due to the weakening of the magnetic field, while β-wave precesses twice as fast as α-wave. As it ejects from the crystal, the α-wave rotates π and the β-wave rotates 2π. The α-wave shows a maximum $(4d_nE_g)/(\mu_nB_{\rm S})$ nEDM effect, while the β-wave shows zero nEDM effect. Overall, the nEDM signal appearing in the y-direction is the average of the α- and β-waves in $(2d_nE_g)/(\mu_nB_{\rm S})$, as indicated by the brown arrow. This is twice the nEDM signal of the conventional method. The conventional case is shown in the upper right panel.

Here we would discuss that the interaction time can be extended under the condition of combined α- and β-wave polarization by adding an external magnetic field and treating the α- and β-wave precessions separately,

Figure 8.3 shows the principle of increasing the interaction time between the nEDM and the intra-crystal electric field by applying an external magnetic field only inside the crystal. This method is named as the external magnetic field application method. A thin solenoid coil (omitted in the figure) is installed in the z-axis direction so that it wraps around the neutron injection and ejection surfaces of the crystal. This allows an external magnetic field $\boldsymbol{B}_{\rm ex}$ to be applied only inside the crystal. Neutrons that enter the crystal and undergo dynamical diffraction are split into α- and β-waves, which are subjected to the opposite Schwinger magnetic fields $\boldsymbol{B}_{\rm S}$ and $-\boldsymbol{B}_{\rm S}$, respectively. Because of the externally applied magnetic field, the α-wave interacts with the magnetic field $(\boldsymbol{B}_{\rm S}+\boldsymbol{B}_{\rm ex})$ and the β-wave interacts with the magnetic field $(-\boldsymbol{B}_{\rm S}+\boldsymbol{B}_{\rm ex})$, resulting in precessional rotation at different Lamor frequencies. By choosing the external magnetic field appropriately, we can find a condition where the α- and β-waves are individually not $P=0$, but they are $P=0$ when they are combined.

For example, by choosing an external magnetic field such that the α-wave has a rotation of π and the β-wave has a rotation of $2n\pi$ $(n=1,2,\cdots)$, the α-wave is polarized to $P=-1$ and the β-wave is polarized to $P=+1$, so the overall polarization is zero. The nEDM signal reaches its maximum value for the α-wave and zero for the β-wave, but the overall value will remain half of the maximum value. If the α-wave rotates at a small Larmor frequency and the β-wave rotates at a large Larmor frequency, the interaction time can be expanded and the maximum value of the α-wave nEDM signal is increased.

Assuming that $\boldsymbol{B}_{\rm ex}$ is κ times larger than $\boldsymbol{B}_{\rm S}$ and is applied in the opposite direction of $\boldsymbol{B}_{\rm S}$, the ratio of

the amount of spin rotation of α-wave to that of the and β-wave is as follows.

$$\frac{\varphi_S^\beta}{\varphi_S^\alpha} = \frac{1+\kappa}{1-\kappa}. \tag{8.1}$$

The spin rotation of the α-wave becomes slower and that of the β-wave becomes faster. In order to become $P = 0$ as a whole, the rotation of the β-wave should be $2n\pi$ when the rotation of the α-wave is π. Therefore, κ can be determined from the following equation.

$$2n = \frac{1+\kappa}{1-\kappa}. \tag{8.2}$$

In this case, the EDM signals (polarization in the y-axis direction) of the α- and β-waves can be expressed by the following equations, respectively,

$$P_{\mathrm{EDM}}^\alpha = \frac{d_n E_g}{\mu_n(1-\kappa)B_{\mathrm{S}}}\left[1-\cos\frac{2\mu_n(1-\kappa)B_{\mathrm{S}}}{\hbar}\tau\right] \tag{8.3}$$

$$P_{\mathrm{EDM}}^\beta = \frac{d_n E_g}{\mu_n(1+\kappa)B_{\mathrm{S}}}\left[1-\cos\frac{2\mu_n(1+\kappa)B_{\mathrm{S}}}{\hbar}\tau\right] \tag{8.4}$$

The synthesized EDM signal is as follows.

$$P_{\mathrm{EDM}} = \frac{1}{2}\left(P_{\mathrm{EDM}}^\alpha + P_{\mathrm{EDM}}^\beta\right) \tag{8.5}$$

Figure 8.4 shows the time evolution of the nEDM signal and the precession of the α- and β-waves due to the Schwinger magnetic field in the conventional method and the external magnetic field application method with $n = 1$ ($\kappa = 1/3$). In the conventional measurement, the nEDM signal reaches a maximum value every $(2n-1)\pi$, but due to $P_x = 0$ condition, the measurement had to be performed at $\pi/2$ rotation. On the other hand, when using the external magnetic field application method with $n = 1$, the period of x-polarization is different for α- and β-waves, and the period and amplitude of the nEDM signal are different. The first $P_x = 0$ from the point of incidence is about 0.1 msec, but the maximum of the nEDM signal can be measured about 0.4 msec, when the second $P_x = 0$ occurs (when the precession of the α-wave is π). Here, the horizontal axis represents the time course, but at the same time it is proportional to the thickness of the crystal, so it needs to be 3 times thicker than in the conventional method.

Figure 8.5 shows the time evolution of the nEDM signal and the precession of the α- and β-waves with the Schwinger magnetic field for $n = 6$ ($\kappa = 11/13$). In this case, the α-wave rotates by only π, while the β-wave rotates by 12π, and the nEDM signal at the $P_x = 0$ position increases sevenfold compared to the conventional method. The thickness of the crystal is then 13 times that of the conventional method. If the intra-crystal electric field is strong and $\pi/2$ rotation can be achieved with thin crystal, it may be possible to prepare thick crystals compatible with the external magnetic field application method. But if not, the availability of thick crystals with good crystallinity is the limitation of this external magnetic field application method.

The external magnetic field application method has the following advantages. First, as can be seen from the $P_x = 0$ points in Fig. 8.4 and 8.5, the rate of change of P_x is the largest in the conventional method, whereas the rate of change is the slowest in the external magnetic field application method, making it easier to control the $P_x = 0$ state. Furthermore, in the external magnetic field application method, the position of $P_x = 0$ can be easily changed by varying the external magnetic field. Therefore, even if the spin analysis axis is slightly tilted, the false signal can be minimized ($\simeq 0$) by scanning the external magnetic field.

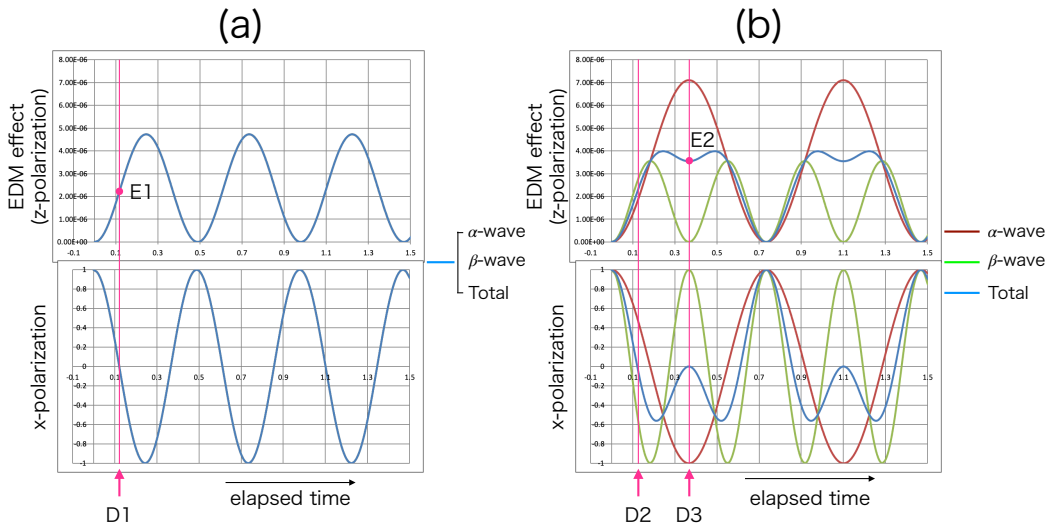

Figure 8.4: Time evolution of the nEDM signal and the precession of the α- and β-waves due to the Schwinger magnetic field:
(a) The conventional method: The time evolution of the polarization of α- and β-waves is the same, and the nEDM effect also has the same time evolution. The measurement is performed at the time (D1) when both α- and β-waves are $P_x = 0$. The maximum value of the nEDM effect is when α- and β-waves are at $P_x = -1$, but the false signal is so large that the measurement is practically impossible. (b) The external magnetic field application method in the case of $n = 1$ ($\kappa = 1/3$): In this case, the α- and β-waves behave differently. The β-wave is twice as fast as the α-wave in both P_x and the nEDM signal. The first $P_x = 0$ state is realized at time D2, at which point the nEDM effect is almost the same as in the conventional method. Next, the measurement is performed at D3, where $P_x = 0$, and the nEDM effect, red circle E2, is obtained. Compared to the conventional method, the interaction time is 3 times longer and the nEDM effect is 1.5 times larger. However, the thickness of the crystal has to be tripled.

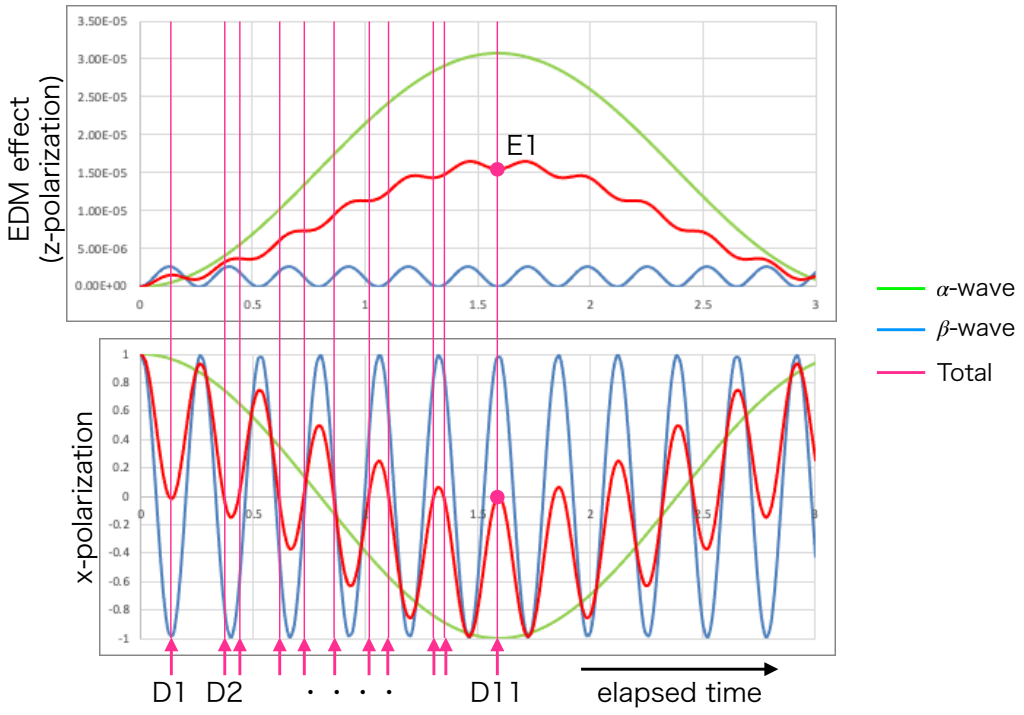

Figure 8.5: Time evolution of the nEDM signal and the precession of the α- and β-waves in the external magnetic field application method in the case of $n = 6$ ($\kappa = 11/13$):
The β-wave is 12 times faster than the α-wave in both P_x and the nEDM effect. The $P_x = 0$ state is realized many times from D1, but the measurement is performed at D11 and the red circle E1 is obtained as the nEDM effect. Compared with the conventional method, the interaction time is 13 times longer and the nEDM effect is 6.5 times larger. However, the crystal thickness must also be increased by a factor of 13.

9 Feasible Study of nEDM Search Experiment by the Crystal Diffraction Method

In this section, we estimate the feasibility of nEDM search experiment by crystal diffraction method. We have confirmed that a strong electric field of the order of 10^8 V/cm is available in the crystal, as expected. There are plans for the remaining two factors that determine the experimental sensitivity, i.e., the increase of statistics and the expansion of interaction time, respectively. Based on these, we would like to calculate the duration of the experiment to obtain a sensitivity of $1.0 \times 10^{-26}\ e \cdot \mathrm{cm}$ for α-quartz and $Bi_{12}GeO_{20}$. The beam intensity is assumed to be $1 \times 10^{12}\ \mathrm{cm^{-2}s^{-1}sr^{-1}meV^{-1}}$. This correspond to the intensity of the current J-PARC MLF 1 MW operation.

9.1 Feasible Study of nEDM Search Experiment Using α-quartz

Table 9.1 shows the results of the feasibility study for (110)-plane of α-quartz, in the case of the conventional nEDM search experiment, the case with the external magnetic field, the case with both the external magnetic field and the multi-unit system. The conventional method requires about 10,000 days to reach the sensitivity of $1 \times 10^{-26}\mathrm{e} \cdot \mathrm{cm}$, while the external magnetic field method reduces the time to 3,500 days, about 1/3 of that by the conventional method, and the addition of the multi-unit system, further reduces the time to 1,200 days, 1/8 of that by the conventional method. If an even stronger neutron source (TOF is not daringly necessary, so a nuclear reactor source can also be used) can be used in the future, it can be said to have sufficient potential.

Table 9.1: Feasibility study for α-quartz.
The number of days required to reach the sensitivity of $1 \times 10^{-26}\ e \cdot \mathrm{cm}$ is shown.The beam intensity is assumed to be $1 \times 10^{12}\ \mathrm{cm^{-2}s^{-1}sr^{-1}meV^{-1}}$ and the beam divergence is 0.42 degrees.

Method	Unit	Conventional	Improvement$_1$	Improvement$_2$
Conventional Method		Base	Base	Base
External Magnetic Field		None	Add	Add
Multi-Unit System		None	None	Add
Electric field	V/cm	2×10^8	2×10^8	2×10^8
Crystal thickness	mm	38.52	115.6	115.6
Crystal width	mm	191	191	191
Crystal hight	mm	50	50	50
Schwinger magnetic field	Gauss	0.1253	0.1253	0.1253
External magnetic field	Gauss	0	0.0418	0.0418
Spin rotation(α)	radian	$\pi/2$	π	π
Spin rotation(β)	radian	$\pi/2$	2π	2π
Interaction time	msec	0.6842	2.0533	2.0533
Number of multi units		1	1	4
Required time	days	9,668	3,416	1,068

9.2 Feasible Study of nEDM Search Experiment Using $Bi_{12}GeO_{20}$

Table 9.2 shows the results of the feasibility study on (532)-plane of $Bi_{12}GeO_{20}$ crystal. Although there are no examples of actual measurements of the intra-crystal electric field in $Bi_{12}GeO_{20}$, theoretical calculations show a value of 5.2×10^8 V/cm in the (433)-plane. In addition, (532)-plane is expected to have a stronger intra-crystal electric field than that in the (433)-plane. Table 9.2 shows the results of the feasibility study on the (532)-plane assuming an electric field of 1×10^9 V/cm. By using the external magnetic field application and the multi-unit system, the number of days required becomes 220 days, and the feasibility becomes even higher.

Table 9.2: Feasibility study for $Bi_{12}GeO_{20}$.
The number of days required to reach the sensitivity of 1×10^{-26} $e \cdot$cm is shown.The beam intensity is assumed to be 1×10^{12} cm^{-2}s^{-1}sr^{-1}meV^{-1} and the beam divergence is 0.42 degrees.

Method	Unit	Conventional	Improvement$_1$	Improvement$_2$
Conventional Method		Base	Base	Base
External Magnetic Field		None	Add	Add
Multi-Unit System		None	None	Add
Electric field	V/cm	1×10^9	1×10^9	1×10^9
Crystal thickness	mm	7.70	53.93	53.93
Crystal width	mm	191	191	191
Crystal hight	mm	50	50	50
Schwinger magnetic field	Gauss	0.9351	0.9351	0.9351
External magnetic field	Gauss	0	0.6679	0.6679
Spin rotation(α)	radian	$\pi/2$	π	π
Spin rotation(β)	radian	$\pi/2$	6π	6π
Interaction time	msec	0.0916	0.6417	0.6417
Number of multi units		1	1	4
Required time	days	1,705	704	220

Thus, it was shown that the statistical sensitivity of the crystal diffraction nEDM search experiment in the Laue configuration can reach 1×10^{-26} $e \cdot$cm by using an external magnetic field and the multi-unit system. Of course, a great deal of phenomenological analysis and technical development still needs to be done to actually implement the plan.

10 Conclusion

The nEDM search experiment is one of the most sensitive probes to search for physics beyond the Standard Model. We are conducting an experimental study of the nEDM search experiment using crystal diffraction. The basis of the crystal diffraction method is the dynamical diffraction theory and the use of the very strong intra-crystal electric field sensed by neutrons in the diffraction process.

Many dynamical diffraction phenomena have been verified using reactor neutron sources. The first step, we have phenomenologically verified dynamical diffraction using a pulsed neutron source. In this study, the experiment were carried out using the pulsed neutron source at MLF in J -PARC. Firstly, Pendellösung fringes were observed using a Si crystal. Then, for α-quartz, Pendellösung fringes with a contrast close to 60% were observed by screening the crystallinity by X-ray topography and infrared absorption spectra. Second, we measured the intensity distribution on the crystal ejection surface by the dynamical diffraction and were able to confirm the intensity distribution indicated by conventional diffraction theory. Third, the intensity of dynamical diffraction was quantitatively estimated. Although perfect agreement could not be obtained, the difference between the calculated and measured values was a factor of 2. Thus, we were able to confirm the same dynamic diffraction phenomena with a pulsed neutron source as with a reactor neutron source.

The second step, using α-quartz, the effective intra-crystal electric fields were measured for (110)-plane in the symmetric Laue configuration and $(0\bar{2}1)$-, (011)-, and $(11\bar{1})$-plane in the asymmetric Laue configuration. For the (110) plane, where the existence of an effective intra-crystalline electric field is expected, the results are consistent with the previous measurements. On the other hand, significant non-zero spin rotations were observed in the $(0\bar{2}1)$- and $(11\bar{1})$-planes, which were thought to have zero effective intra-crystal electric field, indicating that an effective intra-crystal electric field may also exist in these planes. This is thought to be due to interference terms that were thought to cancel out due to Pendellösung oscillation and be negligible. In real crystals, the Pendellösung oscillation may be inhibited by crystal defects of the order of Pendellösung length, and these interference terms do not completely cancel out and appear as an electric field. Such defects in the crystal should be minimized because they introduce systematic uncertainties in nEDM search experiments. The appearance of such an electric field (spin rotation) at the crystal plane, where the effective intra-crystal electric field should be zero, can be used not only as a new indicator to evaluate crystal defects, but also as a clue to investigate systematic uncertainties in nEDM search experiments. Using a pulsed neutron source, we can simultaneously observe spin rotation in multiple crystal planes, including such a crystal plane with $\Delta\phi_g = 0$. By monitoring this spin rotation, we can investigate the systematic uncertainty of the experiment. Since experimental results are still limited, further experimental and theoretical studies are needed to clarify the contribution of the interference terms. Quantitative evaluations are needed for crystals of different crystallinity and at different sites, and for multiple crystal planes with $\Delta\phi_g = 0$. We plan to verify the reproducibility as the first step to validate this hypothesis. Theoretical calculations for crystal planes other than (110) are currently in progress. In the future, we will test this hypothesis using crystals of various crystalline qualities (including Si, Ge, and other centrosymmetric crystals).

Regarding the intra-crystal electric field, which is one of the factors determining the sensitivity of nEDM search experiments using crystal diffraction, it was confirmed that a strong electric field is available as expected. It was shown that the remaining two factors, interaction time and statistics, are improved by an external magnetic field application method and a multi-unit system, respectively. By combining these two methods, we showed the possibility of reaching $1 \times 10^{-26}\ e \cdot \mathrm{cm}$ in 200 days at the highest output power of MLF in J-PARC.

Acknowledgement

First and foremost, I would like to express my greatest gratitude to my supervisor, Professor Hirohiko Shimizu. When I was about to enter the gates of physics again at the age of 60, I was very fortunate to have met Professor Shimizu, who opened and guided me to the fresh and fascinating path of neutron physics. After being introduced to his laboratory, I would like to express my sincere appreciation and respect for his broad mind, high knowledge and deep insight.

In addition, Associate Professor Masaaki Kitaguchi gave me a lot of precise advice in the actual research field. There were many times when he appeared on a whim, thought for a moment, and then gave me precise advice that I had never thought of, which helped me overcome difficulties in my experiments. I cannot thank him enough. I am grateful to Associate Professor Katsuya Hirota for teaching me how to prepare for experiments and detailed techniques in my first neutron experiment at KUANS.

I would like to thank my collaborators, Mr. Masaya Nakaji, Mr. Yuya Uchida, Mr. Seiso Fukumura, Ms. Mayu Hishida, Mr. Ryota Takemori, and Mr. Yakuhiro Fujiie. Mr. Nakaji laid the foundation for the MLF BL17 experiment. Mr. Uchida played a very important role in the experimental setup, especially the slit, which is the key to observing the Pendellösung fringes observation. Mr. Fukumura led us all in the theoretical aspect. Ms. Hishida laid the foundation for the intensity distribution of Pendellösung fringes i, including side reflections. Mr. Takemori introduced a new theoretical framework, the statistical dynamics theory, and measured the intensity distribution of Pendellösung fringes. Mr. Fujiie helped me a lot with my experiment. I was greatly encouraged not only by the experiments with them but also by the study sessions in the seminar. In addition to them, many other students helped me, and I am very grateful to them for treating me, who is older than their fathers, without dividing me.

I am very grateful to the MLF people at J-PARC for providing me with the neutron beam and experimental apparatus. In particular, Dr. Kazuhiko Soyama, Dr. Noboru Miyata, Dr. Takayasu Hanashima, Dr. Kazuhiro Akutsu, and Dr. Hiroyuki Aoki provided technical support on beam line 17 and technical advice on data analysis, which were very important for my research.

Ms. Kazumi Hasegawa, Ms. Eri Ozaki, and Ms. Yoko Yamamoto, my secretaries, always helped me with complicated paperwork and applications. I am especially grateful to Ms. Hasegawa for her help from the beginning to the end of my student life, and for her warm hospitality.

In addition, I was able to receive a grant from the Foundation of Global Life Learning Center to support my Ph.D. studies for the academic year 2019. I am grateful for the financial support, but more than that, I am honored and greatly encouraged to have been selected as a recipient of such a support project. It took me a long time me, but I would like to thank you from the bottom of my heart.

I would also like to thank all of my family members who have supported my selfishness at my age. In particular, I would like to thank my wife, Yuko, who has watched over me warmly for the past 10 years and has made my lunch boxes every day. I would like to dedicate this Ph.D. thesis to my wife, Yuko.

References

[1] G. Aad, T. Abajyan, B.Abbot, et al., "Observation of a new particle in the search for the standard model higgs boson with the atlas detector at the lhc." *Physics letters B*, vol. 716, no. 1, pp. 1-29, 2012.

[2] S. Chatrchyan, V. Khachatryan, A. Sirunyan, et al., "Observation of a new bosson at amass of 125 gev with the cms experiment at the lhc." *Physics Letters B*, vol. 716, no. 1, pp. 30-61, 2012.

[3] X. Fan, T. G. Myers, B. A. D. Sukra, and G. Gabrielse. "Measurement of the Electron Magnetic Moment." *arXiv*, 2209. 13084v2, 7 Dec. 2022.

[4] T. Aoyama, T. Kinoshita and M. Nio. "Theory of the Anomalous magnetic Moment of the electron." *Atoms*, vol. 7, 28, 2019.

[5] Sergey Volkov. "Calculation the five-loop QED contribution to the electron anomalous magnetic moment: Graphs without lepton loops." *Phys. Rev. D*, vol. 100, 096004, 2019.

[6] Richard H.Parker, Chenghui Yu, Weicheng Zhong, Brian Estey, Holger Müller. "Measurement of the fine-structure constant as a test of the Standard Model" *Science*, 360, 191-195 (2018).

[7] Leo Morel, Zhibin Yao, Pierre Clade and Saïda Guellati-Khelifa. "Determination of the Fine-Structure Constant with an accuracy of 81 parts per trillion" *Nature*, 588, 3 December (2020).

[8] C. S. Wu, E. Ambler, R. W. Hayward, D. D. Hoppes, and R. P. Hadson. "Experimental test of parity conservation in beta decay." *Phys. Rev.*, vol. 105, pp. 1413-1415, 1957.

[9] T. D. Lee and C. N. Yang. "Question of parity conservation in weak interaction." *Phys. Rev.*, vol. 104, pp. 254-258, 1956.

[10] R. L. Garwin, L. M. Lederman. *Nuovo Cim.*, Vol. 11, pp. 776, 1959.

[11] J. I. Friedman and V. L. Telegdi. "Nuclear emulsion evidence for parity non-conservation in the decay chain $\pi^+ - \mu^- - e^+$." *Phys, Rev.*, vol. 105, pp. 1681-1682, 1957.

[12] J. H. Christenson, J. W. Crownin, V. L. Fitch and R, Turlay. "Evidence for the 2π decay of the k_2^0 meson." *Physical Review Letters*, vol. 13, pp. 138-140, 1964.

[13] Belle Collaboration, K. Abe, et al. http://arxiv.org/abs/hep-ex/0202027, 2002

[14] B. Aubert and et al. http://arxiv.org/abs/hep-ex/0203007, 2002

[15] A.D.Sakharov,. "Violation of CP invariance C asymmetry and Baryon asymmetry of universe." *JETP Lett.*, vol. 5, pp. 24, 1967.

[16] G.R.Farrar and M.E.Shaoshnikov. "Baryon asymmetry of the universe in the standard model." *Phys. Rev. D*, vol. 50, pp. 774-818, 1994.

[17] G. Luders. "On the equivalence of invariance under time reversal and under particle-antiparticle conjugation for relativistic field theories." *MATEMATISK-FYSISKE MEDDELELSER KONGELIGE DNNSKE VIDENSKABERNES SELSKAB*, vol. 28(5), pp. 1-17, 1954.

[18] E.M.Purcell and N.F.Ramsey. "On the possibility of elevtric dipole moments for elementary particles and nuclei." *Phys. Rev.* , vol. 78, pp. 807, 1950.

[19] W.W.Havens, et al.. "Interaction of neutrons with electrons in lead." *Phys. Rev.* , vol. 72, pp. 634-636, 1947.

[20] C.Abel, et al.. "IMeasurement of the permanent electric dipole moment of the neutron." *Phys. Rev. Lett.*, vol. 124, 081803, 2020.

[21] C.Abel, et al.. "Opticlly pumped Cs magnetometers enabling a high-sensitivity search for the neutron electric dipole moment." *Phys. Rev. A*, vol. 101, 053419, 2020.

[22] M.Pospelov and A.Ritz. "Electricdipole moments as probes of new physics." *Annals of Physics*, vol. 318, pp.119-169, 2005.

[23] P.G.Harris, et al.. "New Experimental Limit on the Electric Dipole Moment of the Neutron" *Physical Review Lettters* , vol. 82, pp.904-907, 1999.

[24] J.M.Pendlebury, et al.. "Geometric-phase-induced false electric dipole moment signals for particles in traps" *Physical Review A.* , vol. 70, 032102, 2004.

[25] C.A.Baker, et al.. "Improved Experimental Limit on the Electric Dipole Moment of the Neutron" *Physical Review Letters* , vol. 97, 131801, 2006.

[26] J.M.Pendlebury, et al.. "Revised experimental upper limit on the electric dipole moment of the neutron" *Physical Review D*, vol. 92, 092003, 2015.

[27] N.F.Ramsey. "The method of successive oscillatory fields" *Physics Today*, vol.33, 7, pp.25-30, 1980.

[28] J. H. Smith, E. M. Purcell and N. F. Ramsey. "Experimental Limit to the Electric Dipole Moment of the Neutron" *Physical Review*. vol. 108, pp.120-122, 1957.

[29] F.M.Piegsa. "New concept for a neutron electric dipole moment search using a pulsed beam" *Physical Review C*. vol. 88, 045502, 2013.

[30] C.G.Shull and R.Nathans. "Search for a neutron electric dipole moment by a scattering experiment" *Physical Review Letters*. vol. 19, pp. 384-386, 1967.

[31] M.Forte. "Neutron-optical effects sensitive to P and T symmetry violation" *J. of Physics G: Nuckear Physics*. vol. 9, pp. 745-754, 1983.

[32] V.L.Alekseev, V.V.Voronin, et al.. "Measurement of the strong intracrystalline electric field in the Schwinger interaction with diffracted neutrons" *Sov. Phys.JETP*. vol.69, pp. 1083-1085, 1989.

[33] V. V. Fedorov, E. G. Lapin, S. Yu. Semenikhin, V. V. Voronin. "Set-up for searching a neutron EDM by the crystal-diffraction method: first measurements" *Physica B*. vol.297, pp.293-298, 2001.

[34] V.V.Fedorov, I.A.Kuznetsov, et al.. "Neutron spin optics in a noncentrosymmetric crystals as a new way for nEDM search" *Nuclear Instruments and Physics Research B*. vol.252, pp. 131-135, 2006.

[35] V.V.Fedorov, I.A.Kuznetsov, et al.. "Neutron spin optics in a noncentrosymmetric crystals as a way for nEDM search. New experimental results" *Physica B*. vol.385-386, pp. 1216-1218, 2006.

[36] V.V.Fedorov, M.Jentschel, et al.. "Perspective for nEDM search by crystal diffraction. Test experiment and results" *Nuclear Physics A*. vol.827, pp. 538c-540c, 2009.

[37] V.V.Fedorov, M.Jentschel, et al.. "Measurement of the neutron electric dipole moment by crystal diffraction" *Nuclear Instruments and Physics Research A*. vol.611, pp. 124-128, 2009.

[38] V.V.Fedorov, M.Jentschel, et al.. "Measurement of the neutron electric dipole moment via spin rotation in a noncentrosymmetric crystal" *Physics Letters B*. vol.694, pp. 22-25, 2010.

[39] V.V.Fedorov and V.V.Voronin. "Neutron diffraction and optics of a noncentrosymmetric crystal. New feasibility of a search for neutron EDM" *arXiv:hep-ex/0504042 v2*. 3 May 2005.

[40] V.V.Fedorov and V.V.Voronin. "Modern status of search for nEDM, using neutron optics and diffraction in noncentrosymmetric crystals" *JPS Conf. Proc. NOP2017*. vol.22, 011007, 2018.

[41] V.V.Fedorov and V.V.Voronin. "Study of neutron fundamental properties in the perfect crystal optics and diffraction" *EPJ Web of Conference PPNS2018*. vol.219, 06004, 2019

[42] F.Kuchler, et al.. "Searches for electric dipole moments − Overview of status and new experimental efforts" *Universe* 2019, 5, 56. universe5020056.

[43] C.G.Darwin. "The theory of X-ray reflection" *Philosophical Magazine* . vol.27, pp.315-333, 1914.

[44] C.G.Darwin. "The theory of X-ray reflection. Part Ⅱ " *Philosophical Magazine*. vol.27, pp.675-690, 1914.

[45] P.P.Ewald. "Reasoning of the crystal optics " *Annalen der Physik*. vol.49, pp.1-38, 1916.

[46] P.P.Ewald. "An explanatory statement concerning crystal optics " *Annalen der Physik*. vol.49, pp.117-143, 1916.

[47] M. von Laue. *Ergebnisse der Exakten Naturwissenshaften*. vol.10, pp.133, 1931.

[48] M.L.Goldberger and F.Seitz. "Theory of the Reflection and the Diffraction of Neutrons by Crystals" *Physical Review*. vol.71, pp.294-310, 1947.

[49] V.F.Sears. "Dynamical theory of neutron diffraction" *Canadian Journal of Physics*. vol.56, pp.1261-1288, 1978.

[50] H.Rauch and D.Petrascheck. "Dynamical Neutron Diffraction and its Application" *Neuron Diffraction*. pp.303-351, edited by H.Dachs (Springer, Berlin), 1978.

[51] C.G.Shull. "OBSERVATION OF PENDELLÖSUNG FRINGE STRUCTURE IN NEUTRON DIFFRACTION" *Physical Review Letters*. vol.21, pp.1585-1589,1968.

[52] S. Itoh, M. Nakaji, Y. Uchida, M. Kitaguchi, H. M. Shimizu. "Pendellösung interferometry by using pulsed neutrons" *Nuclear Instruments and Methods in Physics Research A*. vol.908, pp.78-81, 2018.

[53] V.V.Voronin, E.G.Lapin, S.Yu.Semenikhin, and V.V.Fedorov. "Depolarization of a Neutron Beam in Laue Diffraction by a Noncentrosymmetric Crystal" *JETP Letters*. vol.72, pp.308-311,2000.

[54] V. V. Voronin. *Doctoral thesis*. Petersburg Nuclear Physics Institute, 1994.